

PHASE FIELD AND GRADIENT DAMAGE MODELS IN DUCTILE FAILURE

Erfan Azinpour

Dissertation presented to the Faculty of Engineering, University of Porto, as a requirement
to obtain the Ph.D. degree in Mechanical Engineering

Supervisor:

Professor José Manuel de Almeida César de Sá

Programa Doutoral em Engenharia Mecânica (PRODEM)

Departamento de Engenharia Mecânica (DEMec)

Faculdade de Engenharia (FEUP)

Universidade do Porto (UP)

January 2020

J. Almeida Sá
09/04/2020

Dedicated to my family

“Every scientific fulfilment raises new questions; it asks to be surpassed and outdated.”

Max Weber

Acknowledgements

First and foremost, I express my most sincere gratitude to Prof. Jose M. A. Cesar de Sa, who has fully supported and guided me throughout my Ph.D. programme with his knowledgeable advices. Indeed, without his constant encouragement and kind supervision, the completion of the present thesis could not have been possible. Additionally, I would like to thank Dr. Abel Santos for his invaluable insights that I have been given regarding the finite element modelling in ABAQUS and his perseverance within this scope of the research. I also owe a sincere gratitude to Dr. Pedro Areias as his research activities and innovative advices truly inspired me to pursue my thesis.

I gratefully acknowledge the funding of Projects NORTE-01-0145-FEDER-000022 - SciTech - (NORTE2020) and POCI-01-0145-FEDER-030592 (ifDamagElse), co-financed by Programa Operacional Regional do Norte, through Fundo Europeu de Desenvolvimento Regional (FEDER) and national funds through Fundação para a Ciência e a Tecnologia (FCT), Portugal.

I would also like to thank all colleagues and staff from the department of mechanical engineering of University of Porto and INEGI institution, who have supported me during my Ph.D. program. Last but not least, I would dedicate this thesis to my parents and give very special gratitude to them who have supported me continuously and without a doubt they brought me an enormous level of inspiration throughout my career.

Abstract

This study addresses several computational aspects of failure analysis in ductile metallic materials with emphasis on application of gradient regularisation methodologies in fracture modelling.

The progressive degradation in metals is typically associated with nucleation, growth and coalescence of micro-voids and micro-cracks, followed by meso-crack initiation and propagation. The developed phase-field diffusive fracture models in the course of last two decades gave some key insights into the problem of crack development in brittle and ductile material contexts. These approaches have been proved to be reliable tools in a wide variety of fracture situations, including intricate crack topologies like branching or bifurcation. From another perspective, the issues arisen from the need to observe objectivity of the numerical solutions to avoid mesh dependence pathologies that are commonly reported associated with the use of existing damage models have been successfully dealt with resorting to gradient nonlocal approaches. Although coming from different concepts the phase-field diffusive method in fracture and nonlocal approaches to damage share some similarities as both employ spatial gradients of the microstructural fields to obtain regularized solutions.

The present contribution is an attempt to build a bridge between the existing material modelling that has roots in damage mechanics and fracture mechanics by developing theoretical and computational material framework which gives an advantage of predicting ductile material failure behaviour until final rupture. The crack propagation problem is treated using a phase-field model coupled with a micromechanical damage model, at which the void growth mechanism drives the crack field evolution in the material softening regime. This combined multi-field fracture model framework is implemented using the finite element method and throughout the work, the capabilities and performance of the numerical model is examined via representative fracture

benchmarks that cover a wide range of stress states. Further investigation is carried out by experimentation on additively-manufactured steel components, in which the simulated crack advance in tensile test samples are compared against laboratory experimental data, where the role of the porosity growth is emphasized.

Resumo

Este estudo aborda vários aspectos computacionais de modelos de análise da falha dúctil em materiais metálicos, com ênfase na aplicação de metodologias de regularização de gradiente na modelização de fendas.

A degradação progressiva em metais é tipicamente associada à nucleação, crescimento e coalescência de micro vazios e micro fissuras, seguida de iniciação e propagação de macro fendas. Os modelos desenvolvidos de fractura difusiva que utilizam o modelo de campo de fase, forneceram, no decorrer das últimas duas décadas, algumas percepções fundamentais sobre o problema do desenvolvimento de fendas em materiais frágeis e dúcteis. Estas abordagens provaram ser ferramentas de confiança numa grande variedade de situações de fractura, incluindo topologias complexas envolvendo bifurcação e ramificação de fendas. Numa outra perspectiva, as questões surgidas a partir da necessidade de observar a objectividade das soluções numéricas para evitar patologias de dependência de malha que são comumente associadas ao uso dos modelos de danos e falha existentes têm sido tratadas com sucesso com o recurso a abordagens que utilizam modelos gradiente não locais. Embora provenientes de diferentes conceitos, o método difusivo de campo de fase de fractura e modelos não locais de dano compartilham algumas semelhanças, já que ambos empregam gradientes espaciais dos campos de variáveis internas micro estruturais para obter soluções regularizadas.

Esta contribuição é uma tentativa de construir uma ponte entre os modelos existentes que têm raízes na Mecânica do Dano Contínuo e na Mecânica da Fractura, a partir do desenvolvimento de um enquadramento teórico e computacional que permita prever o comportamento de falha dúctil de um material do início do dano até a ruptura final. O problema de propagação de fendas é tratado usando um modelo de campo de fase juntamente com um modelo de dano micromecânico, no qual o mecanismo de

crescimento de vazios impulsiona a evolução e crescimento da fenda no modelo de campo de fase. Esta estrutura combinada de um modelo multi-campo de fractura é implementada computacionalmente usando o método dos elementos finitos. Ao longo do trabalho, as capacidades e o desempenho do modelo numérico são examinados por meio de testes representativos que abrangem uma ampla gama de estados de tensão. Uma investigação adicional é realizada em componentes de aço obtidos por fabrico aditivo em que, salientando-se o papel da porosidade, a observação experimental da evolução da fractura em provetes é comparada com os resultados obtidos com o modelo numérico desenvolvido.

Contents

1	Introduction	1
1.1	Motivation and background	2
1.2	Objectives and tasks.....	5
1.3	Thesis organisation	5
2	Elements of Continuum Mechanics and Fundamental Concepts	7
2.1	Kinematics of deformation	7
2.1.1	Deformation gradient.....	8
2.1.2	Strain and stress measures	9
2.2	Fundamental laws	11
2.2.1	Conservation of mass and momentum balance	11
2.2.2	Laws of thermodynamics.....	12
2.2.3	Constitutive theory	13
2.2.4	Heat transfer analysis.....	14
2.2.5	Initial boundary value problem and finite element method.....	15
3	Local approaches to ductile fracture.....	19
3.1	Physical background	19
3.2	Mathematical models in ductile failure.....	22
3.2.1	Constitutive framework of the Lemaitre's damage criterion:	23
3.2.2	Gurson-based damage models	31
3.2.3	Rousselier damage model:.....	32
4	Gradient regularisation of ductile failure models	36
4.1	Nonlocal regularisation approaches	37
4.1.1	Mathematical background	37
4.1.2	Nonlocal gradient regularisation of ductile damage.....	39
4.1.3	A simple and unified solution strategy for the coupled problem	40

4.2	Phase-field modelling of fracture in brittle solids	41
4.2.1	Regularisation of the sharp crack topology	42
4.2.2	Constitutive relations in a fractured solid.....	44
4.2.3	Weak form of the boundary value problem.....	46
4.2.4	Finite element implementation using a staggered solution strategy.....	47
4.3	Phase-field diffusion model in ductile fracture.....	49
4.3.1	General description.....	49
4.3.2	Extended formulation to the micromechanical damage framework.....	50
4.3.3	Numerical implementation of the coupled multi-field problem.....	52
4.3.4	Integration algorithm of the phase-field diffused pressure-dependent plasticity model	54
4.3.5	Derivation of the consistent tangent moduli.....	58
5	Numerical results.....	64
5.1	Phase-field solution method validation in brittle setting	65
5.1.1	Verification of the solution on a single element.....	65
5.1.2	Phase-field crack in 2D analysis:	67
5.2	Numerical modelling of fracture using the phase-field coupled ductile fracture model:	72
5.2.1	Verification of the coupled model on a single element	72
5.2.2	Tensile test on round bars:.....	73
5.2.1	Tensile test on asymmetrical notched specimen:	78
5.2.1	Shear sample.....	85
5.3	Nonlocal gradient regularisation analysis.....	88
5.3.1	Flat grooved tensile specimen	91
6.	Experimental and numerical modelling of fracture in additively manufactured steel components.....	97
6.1.	Experimental procedure	99
6.1.1.	Microstructural observations	103

6.2.	Numerical analysis of fracture in DED processed samples	106
6.2.1.	Determination of the material parameters	107
6.2.2.	An approach to identify initial porosity values using Generalised Mixture Rule (GMR).....	109
6.2.3.	Crack analysis using phase-field ductile fracture model	119
7	Summary and conclusions	122
7.1.	Concluding remarks	123
7.2.	Future work.....	124

LIST OF FIGURES

Figure 2.1 Finite deformation of a solid from initial configuration to the current configuration.....	9
Figure 3.1 Micromechanical evolution of ductile fracture	21
Figure 3.2 Illustration of a damaged element	25
Figure 4.1 a) One-dimensional bar with a crack at $x = 0$, b) variation of the phase-field with the length scale	43
Figure 4.2 a) Sharp crack versus b) diffused crack topology using phase-field regularisation method; width of the diffused region is characterized by ld	45
Figure 4.3 a) Schematic representation of the staggered solution procedure using Abaqus/Standard routines.....	53
Figure 5.1 Single plane strain element under a) tensile and b) shear loading	66
Figure 5.2 Analytical versus numerical load history for the single tensile element.....	68
Figure 5.3 Analytical versus numerical phase field history for the single tensile element	68
Figure 5.4 Analytical versus numerical load history for the single shear element.....	69
Figure 5.5 Length scale sensitivity of the phase-field problem for the single tensile element	69
Figure 5.6 Single edge notched tensile test a) geometry and boundary conditions and crack development at b) $u_1 = 0.005 \text{ mm}$, c) $u_1 = 0.00622 \text{ mm}$ and d) $u_1 = 0.00705 \text{ mm}$	70
Figure 5.7 Double asymmetrical notched sample a) geometry and boundary conditions and crack development at b) $u_1 = 0.0296 \text{ mm}$, c) $u_1 = 0.0386 \text{ mm}$ and d) $u_1 = 0.05 \text{ mm}$	71
Figure 5.8 Influence of the fracture coefficient on the material response of the single element using the diffusive ductile fracture model	73
Figure 5.9 Tensile test on a) smooth round bar and b) notched round bar with notch radius of 20; dimensions are in mm	75
Figure 5.10 Force vs. displacement using local damage models for the SRB sample ...	76
Figure 5.11 Force vs. displacement using local damage models for the NRB sample ..	77
Figure 5.12 Influence of the fracture coefficient on the global response of the SRB and NRB samples using the coupled phase-field ductile fracture model.....	77

Figure 5.13 Contour plots of the equivalent plastic strain, void volume fraction and phase-field at different load increments.....	79
Figure 5.14 Stress triaxiality distribution along the bottom edge of the quarter of tensile test specimens	80
Figure 5.15 Stress triaxiality versus the equivalent plastic strain for the tensile test specimens	80
Figure 5.16 Asymmetrical notched specimen under tensile loading; geometry, boundary conditions and the mesh discretization of the critical region; dimensions are in <i>mm</i> ...	81
Figure 5.17 Force vs. vertical displacement using local Rousselier damage model for the asymmetrical notched specimen.....	83
Figure 5.18 Force vs. vertical displacement using diffusive Rousselier damage model for the asymmetrical notched specimen	83
Figure 5.19 Damage profile in the asymmetrical notched specimen at different deformation levels	84
Figure 5.20 Evolution of equivalent plastic strain and phase-field crack in asymmetrical notched specimen in the post-critical deformation regime.....	84
Figure 5.21 Experimental observation of fracture in asymmetrical notched specimen conducted in [80].....	85
Figure 5.22 Contour plots of the axial and equivalent stresses at different deformation levels.....	86
Figure 5.23 a) Geometry and boundary condition of the shear sample; b) fractured specimen [81]	87
Figure 5.24 Force vs. vertical displacement using diffusive Rousselier damage model for the shear specimen.....	89
Figure 5.25 Length scale sensitivity of the diffusive Rousselier damage model for the shear specimen.....	89
Figure 5.26 Influence of the fracture coefficient on the global response of the diffusive Rousselier damage model for the shear specimen.....	90
Figure 5.27 Contours of the equivalent plastic strain and phase-field profiles in the material post-critical regime for the shear specimen at different deformation levels	90
Figure 5.28 Contours of the equivalent stress and the axial stress in the material post-critical regime for the shear specimen at different deformation levels	91

Figure 5.29 a) Flat-grooved sample geometry and discretisation of the quarter of sample with element edge size of b) $bh = 0.25 \text{ mm}$, c) $bh = 0.125 \text{ mm}$ and d) $bh = 0.094 \text{ mm}$	93
Figure 5.30 Evolution of the internal damage represented via the ($a1 - a3$) local field and ($b1 - b3$) nonlocal field	94
Figure 5.31 a) Force versus deflection obtained from the local damage model and b) evolution of the local damage field	95
Figure 5.32 a) Force versus deflection obtained from the nonlocal gradient damage model and b) evolution of the nonlocal damage field.....	96
Figure 6.1 SEM image of stainless steel 316L powder feed material used in DED process	100
Figure 6.2 Metal filling patterns during the fabrication process	101
Figure 6.3 DED-processed 316L cubic component with test specimens in three orientations	102
Figure 6.4 Schematic of the building directions during the fabrication process for a) sample group $T1i$ and b) sample groups $T2i$ and $T3i$	102
Figure 6.5 Geometry of the tensile test samples (dimensions in mm).....	103
Figure 6.6 Deformed and fractured tensile test specimens.....	103
Figure 6.7 The engineering stress versus strain graphs taken from tensile samples	105
Figure 6.8 Relationship between the porosity and global energy density function in DED processes.....	105
Figure 6.9 Porosity observation in the fabricated samples before the test	106
Figure 6.10 (a, b) Fracture surfaces, (c) Identified defects dominated by crack initiation	107
Figure 6.11 (a) Force versus displacement and (b) void volume fraction evolution for sample T11 using the local Rousselier model	111
Figure 6.12 (a) Force versus displacement and (b) void volume fraction evolution for sample T31 using the local Rousselier model	112
Figure 6.13 Ellipsoid pores with dimensions a, b and c in the fabricated component microstructure.....	113
Figure 6.14 Melt pool dimensions in the fabricated component microstructure.....	114
Figure 6.15 Force vs. displacement graph obtained from Rousselier damage model against experimental data for sample $T32$	116

Figure 6.16 Force vs. displacement graph obtained from Rousselier damage model against experimental data for sample <i>T33</i>	117
Figure 6.17 Force vs. displacement graph obtained from Rousselier damage model against experimental data for sample <i>T34</i>	117
Figure 6.18 Force vs. displacement graph obtained from Rousselier damage model against experimental data for sample <i>T35</i>	118
Figure 6.19 Linear regression of the scattered data of identified initial porosity values at yield strength of each sample of group <i>T3i</i>	118
Figure 6.20 Force versus displacement for samples T11 and T31 using the phase-field ductile fracture model.....	120
Figure 6.21 Distribution of equivalent plastic strain, phase-field crack, axial stress and von-Mises equivalent stress in the post-critical regime for sample T11 and at different deformation levels: a) $\varepsilon_{22} = 63\%$, b) $\varepsilon_{22} = 63.8\%$, c) $\varepsilon_{22} = 64.3\%$ and d) $\varepsilon_{22} = 66.8\%$	121

LIST OF TABLES

Table 5.1 Material parameters of Al-6061(T6) used for the numerical modelling of tensile samples	75
Table 5.2 Material parameters used for the numerical modelling of asymmetrical notched tensile test	82
Table 5.3 Material parameters used for the numerical modelling of shear sample.....	88
Table 5.4 Material parameters used for the numerical modelling of flat grooved sample	92
Table 6.1 Fabrication parameters employed in the DED process	100
Table 6.2 Chemical Composition of stainless steel 316L.....	100
Table 6.3 Thermo-physical properties of stainless steel 316L initial powder.....	101
Table 6.4 Mechanical properties of the samples	104
Table 6.5 Material parameters for the DED-processed AISI 316L steel alloy used for the numerical modelling of tensile test on T11 and T31 specimens	109
Table 6.6 Comparison of identified values of initial porosity using FEM and GMR methods.....	119

NOMENCLATURES

In alphabetical order:

A	Void nucleation term coefficient
$A_{\vec{e}_x}, A_{\vec{e}_y}, A_{\vec{e}_z}$	Melt pool cross sections
a, b, c	Dimensions of the pores
B_0, B	Reference and current configuration of a body
B	Left Cauchy-Green strain tensor
b, \bar{b}	Body force vector at current and reference configuration
B, B^d	Displacement and phase-field gradient operator
β	Weighted averaging operator in nonlocal integral model
β_∞	Integral nonlocal bell-shaped function
C	Right Cauchy-Green strain tensor
c_p	Specific heat
C_1, C_2, C_3, C_4	Coefficients of the J factor parameter
D	Rate of the deformation
$\mathfrak{D}, \bar{\mathfrak{D}}$	Current and reference mass density
D	Rousselier damage parameter
$\mathcal{D}, \bar{\mathcal{D}}$	Lemaitre local and nonlocal damage variable
D^e	Fourth order elastic tangent matrix
D^p	Pressure-dependent plastic consistent tangent operator
E	Green-Lagrange strain tensor
e	Euler-Almansi strain tensor
ε	Infinitesimal strain tensor
$\varepsilon^e, \varepsilon^p$	Elastic and plastic strain tensor

ε_v^e	Volumetric elastic strain component
$\boldsymbol{\varepsilon}_d^e$	Deviatoric elastic strain tensor
$\bar{\varepsilon}^p$	Equivalent plastic strain
$\bar{\varepsilon}_c^p$	Critical equivalent plastic strain
ε_N	Mean equivalent plastic strain
ε_c	Strain associated with the critical stress
ε^*	Thermal strain
\dot{e}	Rate of the specific internal energy
\mathbf{F}	Deformation gradient
$\mathbf{F}_{iso}, \mathbf{F}_{vol}$	Isochoric and volumetric components of deformation gradient
$\mathbf{f}^{int}, \mathbf{f}^{ext}$	Internal and external force vectors
F, \bar{F}	Arbitrary local and nonlocal fields
f	Void volume fraction
f_0	Initial void volume fraction
f_c	Critical void volume fraction
f_f	Void volume fraction at fracture
f_N	Void volume fraction of nucleating voids
f^*	Effective porosity
F	Force conjugated to the void volume fraction
g	Rousselier damage function
$g(d)$	Phase-field degradation function
G	Shear modulus
h_s	Heat source term
h	Hatch spacing

H	Phase-field crack driving force
\hbar	Heat input parameter
I	Second order identity tensor
I_s	Symmetric identity tensor
I_d	Fourth order deviatoric projection tensor
I_1, I_2, I_3	Invariants of stress tensor
J	Material Jacobian
J	J fractal parameter from GMR approach
K	Bulk modulus
\bar{K}	Strength coefficient
κ	Dimensionless numerical parameter
\mathcal{K}	Thermal conductivity
L	Velocity gradient
l	Radius of the hatches in the melt pool
l_N	Nonlocal gradient intrinsic length
l_d	Phase-field fracture length parameter
m	Mass of the nonporous material
$M_c; M_s$	Mechanical property of phases of composite; bulk
n	number of dimensions of body B_0
N	Normal vector to the surface that force applied
N_i^e	Shape function associated with node i and element e
N_i^g	Global shape function
N_1, N_2, N_3	Number of the pores in \vec{e}_x, \vec{e}_y and \vec{e}_z directions
n_{node}	number of the nodes in each element

n_{elem}	Number of the elements in the global mesh
n_{point}	Number of the nodes in the global mesh
η	Fracture coefficient
η^*	Stress triaxiality
\mathcal{P}	Material particle in body B_0
\mathbf{P}	First Piola-Kirchhoff stress tensor
p	Hydrostatic stress or pressure
Q	Heat flux
\mathcal{Q}	Volumetric powder flow
q	von Mises equivalent stress
\bar{q}	Trial von Mises equivalent stress
q^*	Mass powder flow
q_1, q_2, q_3	GTN material parameters
\mathbf{R}	Orthogonal rotation tensor
R	Hardening function
R^d	Phase-field residual force
\bar{R}	Viscous crack resistance
\mathcal{r}	Density of the heat production
r, r_0	Mean and initial radius of a cavity
r_1, r_2	Lemaitre damage parameters
ρ	Relative density of the voids
$\rho_c; \rho_s$	Density of phases of composite; bulk
ρ_{powder}	Density of powder
\mathbf{S}	Second Piola-Kirchhoff stress tensor

\mathbf{s}	Deviatoric stress tensor
s	Entropy
S	Phase-field crack state function
s_N	Mean equivalent plastic strain standard deviation
$\boldsymbol{\sigma}$	Cauchy stress tensor
$\sigma_1, \sigma_2, \sigma_3$	Principal stress components
$\mathbf{s}_1, \mathbf{s}_2, \mathbf{s}_3$	Principal deviatoric stress components
σ_c	Critical stress
σ_0	Stress flow of the undamaged material
σ_T, ε_T	True stress; True strain
σ_N, ε_N	Engineering stress; Engineering strain
σ_1	Rousselier damage parameter
σ_m	Mean stress
T	Temperature
t	Surface traction force
t_0	Nominal surface traction force
∇T	Temperature gradient
δT	Liquidus and solidus temperature difference
\mathbf{u}	Displacement field
U	Right stretch tensor
\mathbf{v}	Velocity of particle \mathcal{P} at the reference configuration of body
\mathbf{v}	Velocity of particle \mathcal{P} at the current configuration of body
V	Left stretch tensor
v	Scan speed of the laser beam in DED process

$V_w; V_s$	Volume of phases of porous; bulk
V	Volume of the melt pool
\mathbf{W}	Spin tensor
W	Laser power of DED process
\mathbf{x}, \mathbf{X}	Position of particle \mathcal{P} at current and reference configurations
χ	Volumetric thermal expansion coefficient
Y	Damage energy release rate
Υ	Absorption coefficient
Ω_0	Reference internal region of body B_0
$\partial\Omega_0$	Reference external boundary of body B_0
$\boldsymbol{\varphi}$	Deformation mapping
ξ	Normalized third invariant of the deviatoric stress tensor
$\theta, \bar{\theta}$	Lode angle and its normalised value
ϑ	thermal diffusivity
ψ	Helmholtz free energy
ψ_e, ψ_p	Elastic and plastic components of free energy
ψ_d	Free energy part associated with damage dissipation
ψ_{ed}	Elastic-damageable component of free energy
φ	Yield function
ϕ	Yield potential
α	Internal variable
$\dot{\gamma}$	Plastic multiplier
ζ	Position of an infinitesimal volume
ω	Material integrity parameter in Lemaitre damage model

1 Introduction

Over the past century, the technological and machinery advances have introduced many crucial subjects to the engineering community. Prevention of failure and structural integrity in components is one of the most intriguing and yet challenging fields to date, where a great deal of attention is focused on its methodological and practical sides. Fracture in structures is a physical phenomenon that can be caused due to various reasons, ranging from external circumstances such as environment or loading types, to structural characteristics, such as, for instance, impurities, voids or pre-existing cracks in the material bulk. Prediction and prevention of the fracture phenomena, that is directly associated with an improved structural integrity of the material, is of utmost importance in scientific community and defines the main goal in the present research.

It is a very common practice to conduct fracture analyses with a series of experimental and numerical tests in order to precisely predict material failure. The simulation of materials behaviour by means of efficient numerical methods, is a high influential factor in industrial sectors in order to save financial resources and consumption of energy and time which all aim to retain a sustainable world. Depending on the characteristics of the materials that lie either on the categories of brittle or ductile, there exist a great deal of research studies regarding failure analysis, pointed to either of these fracture types, which indeed gave rise to the development of mathematical models categorized within the fracture mechanics and damage mechanic fields. The core idea of the present study is to develop a material model that has roots in both areas, with the application for ductile metallic materials.

This chapter firstly brings to the attention a review over the influential studies in the context of fracture and damage mechanics that suggests the importance of this research work. Next, the primary objectives of this study are specified and the last section outlines the organisation of the thesis.

1.1 Motivation and background

Fracture analysis in structures is mainly described as a tool to reveal the level of resistance in materials under loading, which is linked to the losing of material load-carrying capacity. Within the context of ductile materials, such as aluminium or steel alloys, the material undergoes an extensive level of plastic deformation after some certain amount of load, which is typically followed by the accumulation of damage. The latter phenomenon is linked to the material internal degradation that is verified from micromechanical observations. This deformation phase typically is preceded by the formation and development of macro-structural defects, which are often referred to as the initiation and propagation of macro-cracks.

Different from the cleavage fracture, ductile material failure induces more sophisticated fracture surfaces such as cup-cone or curvilinear cracks. To date, a large number of numerical tools have been developed to simulate the behaviour of material under various levels of degradation, varying from the discrete crack approaches in the context of linear elastic fracture mechanics (LEFM), to the phenomenological damage frameworks in the context of continuous damage mechanics (CDM).

It has been shown in many studies that the discrete representation of cracks in structures is not an adequate, in many cases not efficient, way to deal with the development of fracture. Most of the issues correspond to the classical discrete crack approaches come from the conformity of the geometry discretization alignment with crack discontinuities. In line with this, there are several numerical techniques such as the extended finite element methods (XFEM) [1], remeshing strategies [2] or meshless methods such as the element-free Galerkin methods [3] that were introduced as a remedy to alleviate the mesh-induced issues attributed to the classical discrete crack approaches.

In light with the diffusive approaches to fracture, the well-received phase-field approach in fracture avoids the sharp description of the crack topology, introducing several advantages such as the analysis of crack on a fixed mesh and the flexibility to handle the intricate crack patterns such as crack branching, merging or bifurcation. This method bypasses the need to numerically track fracture interfaces to impose displacement jumps at discontinuities.

Subsequent to the development of this methodology in [4], motivated by the mathematical basis of Ambrosio and Tortorelli [5], that was originally applied for image

segmentation, this method has been studied and implemented within the finite element framework through the course of last two decades and is addressed as a reliable tool for assessment of crack initiation and propagation in brittle fracture [6–11], ductile fracture [12–15], fatigue fracture [16], cohesive fracture [17,18], among others. Distinguishing the fractured regions using an order parameter, or the so-called *phase-field crack* parameter that is introduced as a scalar value between zero and one, resembles the description of internal damage variable in damage mechanics, though each came from different concepts.

The ductile material progressive degradation has been frequently studied in the context of continuous damage mechanics, where the mathematical models are established based on thermodynamical considerations and typically the internal material degradation is defined based on the evolution of an internal damage variable in the micromechanical level. In this regard, phenomenological or micromechanically-motivated damage models were developed in the *local* material continuum. A strong coupling between the plastic deformations and damage variable commonly characterises the constitutive model description, which in turn makes a direct influence on the material loss of load-carrying capacity through the proper definition of the stress-degrading mechanism.

Within the framework of micromechanically-based damage models that are primarily attributed to the early work of Gurson in the porous media [19], the micro-void or porosity growth is considered as the main source of material internal degradation. Due to the inability of pioneering versions of Gurson-based models in predicting softening induced by shear-dominant loading conditions, several enhancements were proposed, as can be found for instance in references [20,21].

In a close relation with this model and its extended version by Tvergaard and Needleman that is well known as the GTN model [22], Rousselier [23,24] introduced a simpler damage concept based on thermodynamical considerations that incorporates a yield function with less model parameters. Following its mathematical concept, the vertex of the Rousselier yield function gives benefit of prediction of damage growth under shear-dominated failure situation, which makes it a suitable choice for analysis of ductile fracture in a wide range of stress triaxialities. This damage model has been investigated for prediction of cup-cone fracture [25–27] and clinched joint failure [28]. Potentially improved versions can be found in the context of nonlocal gradient regularization [29,30], *localizing* gradient enhancement [31] and XFEM [32]. An efficient method regarding the

integration algorithm and use of edge rotations to assess crack propagation was discussed in [33]. Due to the fact that the original damage law does not consider the void coalescence mechanism, a modification was proposed by Zanganeh et al. [34] based on a coalescence onset criterion [35] to accelerate the failure in the post-critical material behaviour. The Rousselier model is largely utilised in the present work.

The conventional description of damage in the CDM and micromechanical damage approaches gave rise to mesh-dependent issues that are linked to the ill-posedness of the equations governing the boundary value problem. It has been established that the utilisation of *nonlocal* damage models could alleviate these mesh-induced issues. An implicit gradient nonlocal damage model that uses a second order gradient term in the construction of mathematical model efficiently proves the ability to model the internal degradation independent of the mesh discretisation, whereby a length scale parameter is involved in the description of the constitutive model. The representation of the nonlocal variable using an additional gradient equation resembles the phase-field diffusive crack model structure, although with utterly different backgrounds. Interested readers are referred to [36,37], where both approaches are compared through the mathematical framework and numerical representations.

In recent years, combining the phase-field concept in fracture with the ductile deformation material models became popular as the former developed models in brittle context revealed an inadequacy in analysis of fracture. This can significantly enhance the performance and predictive ability of the phase-field numerical tools in fracture of solids, that defines one of the main objectives of the present study, as is described in the next section.

In [13], authors followed a purely geometric approach to generalise the phase-field energetic concept towards the stress-based criteria, at which the influence of the inelastic deformation could be considered through the use of an alternative crack driving force. This approach provides a basis for the phase-field problem to be coupled with various constitutive models, which has been addressed recently in the context of von Mises plasticity [38] and GTN damage model [15].

Resorting to this methodology, the Rousselier damage criterion is here introduced as the underlying damage model and is considered herein as a precursor to the crack development through the initiation and propagation of cracks. The coupled material

model performance is assessed via numerical simulation on several fracture benchmarks with ductile material characteristics which also includes the analysis of tensile samples produced with additive manufacturing technology in an attempt to broaden its field of application. This could be of particular interest within the present material framework as it has been revealed that metallic components fabricated by this process have some levels of porosity which could be mostly linked to the process conditions.

1.2 Objectives and tasks

The primary objective of the present research is the development and numerical implementation of the mathematical formulation linked to the gradient approaches in ductile failure. This corresponds to the utilisation of phase-field and gradient nonlocal damage approaches, their implementation within the finite element framework and the evaluation of the numerical model to assess fracture behaviour through a combination of numerical and experimental examples.

In the scope of present research, the following tasks are defined:

1. The derivation of the mathematical formulation for the gradient approaches. This task includes the definition of suitable couplings between the mechanical problem and the nonlocal or phase-field parameter from the gradient problem.
2. Numerical implementation. The boundary value problem described in the previous task is implemented within the finite element framework using ABAQUS software by utilising proper user interface codes.
3. Performance assessment. The predictive ability and performance of the implemented numerical method is analysed through several fracture benchmarks, including tensile samples of steel alloy that are produced by an additive manufacturing process.

1.3 Thesis organisation

The thesis is organised in seven chapters as follows. The next chapter reviews some of the fundamental concepts including the elements of continuum mechanics and laws of thermodynamics. The physical process of fracture in ductile metallic materials and some of the damage models that are mainly used in this work are revisited in chapter 3.

Main body of research corresponds to the coupled gradient approaches in ductile fracture is presented in chapter 4, where the gradient nonlocal and phase-field fracture approaches are defined in the context of ductile fracture and their numerical implementation are explained in detail, whereby an alternative scheme is used for the solution of gradient nonlocal damage model.

Chapter 5 presents the numerical results of the developed models in the previous chapter obtained by quantitative and qualitative assessment of several known fracture benchmarks. The phase-field model performance is further investigated in chapter 6 by analysing tensile samples fabricated from stainless steel 316 L powder base using additive manufacturing with the emphasis on the porosity growth. The additive manufacturing process of the components are briefly explained in the first section of chapter and the simulations of the fracture are discussed subsequently. The thesis is concluded in chapter 7 by presenting the primary findings and future perspectives in line with this study.

2 Elements of Continuum Mechanics and Fundamental Concepts

This chapter reviews several basics including the principles of continuum mechanics and thermodynamics in the continuous materials. The information provided here is indeed required for understanding the mathematical basis of the material models in the subsequent chapters. The following notations are used henceforth: The vectors and second order tensors are denoted by the italic and bold letters, the fourth order tensors are represented by bold letters, the scalars are written as italic letters and the symbols \cdot and $:$ indicate the contraction and double contraction products, respectively.

2.1 Kinematics of deformation

Displacement and the change in the material shape or size known as the deformation, construct the main skeleton of the continuum mechanics. Let \mathcal{B}_0 be the reference or initial configuration of a n dimensional body encompassing the region $\Omega_0 \in \mathbb{R}^n$ with $\partial\Omega_0 \in \mathbb{R}^{n-1}$ as an external boundary (Figure 2.1). Assuming \mathcal{P} as a material particle, the change in the state of the body from the initial configuration (particle position at \mathbf{X}) to the current configuration \mathcal{B} (particle position at \mathbf{x}) may be characterized by a transformation, i.e. a deformation mapping denoted by $\boldsymbol{\varphi}$ at time t as follows:

$$\mathbf{x} = \boldsymbol{\varphi}(\mathcal{P}, t) \quad (2.1)$$

where \mathbf{x} is the position of the particle in the current or deformed configuration. For an invertible deformation mapping, the position of \mathcal{P} at time t may be expressed by:

$$\mathcal{P} = \boldsymbol{\varphi}^{-1}(\mathbf{x}, t) \quad (2.2)$$

The displacement of the particle at time t may be given by

$$\mathbf{u}(\mathcal{P}, t) = \mathbf{x} - \mathcal{P} = \boldsymbol{\varphi}(\mathcal{P}, t) - \mathcal{P} \quad (2.3)$$

Accordingly, the velocity of \mathcal{P} at the reference configuration is defined by the time derivative of the deformation mapping as:

$$\mathbf{V}(\mathbf{x}, t) = \frac{\partial \boldsymbol{\varphi}(\mathcal{P}, t)}{\partial t} \quad (2.4)$$

Using Eq.(2.2), the spatial velocity, i.e. the velocity at the current position is expressed by:

$$\mathbf{v}(\mathbf{x}, t) = \mathbf{V}(\boldsymbol{\varphi}^{-1}(\mathbf{x}, t), t) \quad (2.5)$$

2.1.1 Deformation gradient

The deformation gradient is a second order tensor which relates the reference and current configurations by the following expression:

$$\mathbf{F}(\mathcal{P}, t) = \frac{\partial \boldsymbol{\varphi}(\mathcal{P}, t)}{\partial \mathcal{P}} = \frac{\partial \mathbf{x}}{\partial \mathcal{P}} = \nabla_{\mathcal{P}} \boldsymbol{\varphi}(\mathcal{P}, t) \quad (2.6)$$

where $\nabla_{\mathcal{P}} \boldsymbol{\varphi}(\mathcal{P}, t)$ is called the material or initial gradient of the deformation $\boldsymbol{\varphi}$. Recalling Eq. (2.3), the deformation gradient may be defined in terms of the displacement field:

$$\mathbf{F}(\mathcal{P}, t) = \mathbf{I} + \nabla_{\mathcal{P}} \mathbf{u} \quad (2.7)$$

being \mathbf{I} the second order identity tensor and $\nabla_{\mathcal{P}} \mathbf{u}$ the material displacement gradient in the reference configuration. It is possible to define the deformation gradient in terms of the spatial coordinates as

$$\mathbf{F}(\mathbf{x}, t) = (\mathbf{I} - \nabla_{\mathbf{x}} \mathbf{u})^{-1} \quad (2.8)$$

Any change in the material volume is determined by the following relation:

$$dv = J dV \quad (2.9)$$

where dV and dv are the reference volume and the volume of the deformed body respectively, and J , the Jacobian, is the determinant of the deformation gradient:

$$J \equiv \det \mathbf{F} \quad (2.10)$$

The above Jacobian must be strictly positive, i.e. $J > 0$, in order to prevent the acceptance of self-penetration of the body upon deformation. It is established that any deformation can be split into the pure volumetric and isochoric components such that:

$$\mathbf{F} = \mathbf{F}_{iso} \mathbf{F}_{vol} \quad (2.11)$$

in which isochoric deformation \mathbf{F}_{iso} does not generate any change in the volume of the body, i.e. $J = 1$, expressed by:

$$\mathbf{F}_{iso} = (\det \mathbf{F})^{\frac{-1}{3}} \mathbf{F} = J^{\frac{-1}{3}} \mathbf{F} \quad (2.12)$$

and volumetric part is given by:

$$\mathbf{F}_{vol} = (\det \mathbf{F})^{\frac{1}{3}} \mathbf{I} = J^{\frac{1}{3}} \mathbf{I} \quad (2.13)$$

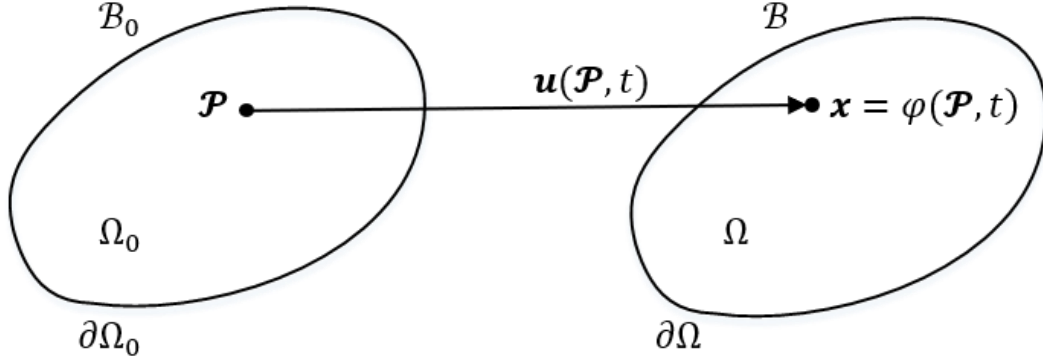


Figure 2.1 Finite deformation of a solid from initial configuration to the current configuration

From another perspective, the deformation gradient may be decomposed into a pure body positive definite stretch tensor and a rotation tensor, using the following relation:

$$\mathbf{F} = \mathbf{R}\mathbf{U} = \mathbf{V}\mathbf{R} \quad (2.14)$$

where \mathbf{R} is an orthogonal rotation tensor, and the symmetric tensors \mathbf{U} and \mathbf{V} are respectively, right and left stretch tensors that are expressed by:

$$\mathbf{U} = \sqrt{\mathbf{C}} \quad , \quad \mathbf{V} = \sqrt{\mathbf{B}} \quad (2.15)$$

being \mathbf{C} and \mathbf{B} right and left Cauchy-Green strain tensors that in turn, may be written as

$$\mathbf{C} = \mathbf{U}^2 = \mathbf{F}^T \mathbf{F} \quad , \quad \mathbf{B} = \mathbf{V}^2 = \mathbf{F} \mathbf{F}^T \quad (2.16)$$

For a rigid body motion, the above Cauchy-Green tensors coincide and become equal to a second order identity tensor.

2.1.2 Strain and stress measures

Within the scope of deformation analysis of structures, the strain measure quantifies the displacement between the material particles of the deformed body relative to the reference configuration. In many cases strains may be assumed to be small (infinitesimal) between

the initial and final configurations or between two consecutive configurations in an incremental process. This will be the case here where the main body of research is based on small deformation theory.

The Green-Lagrange strain measure is defined based on a rigid body motion, given by the following tensor:

$$\mathbf{E} = \frac{1}{2}(\mathbf{C} - \mathbf{I}) \quad (2.17)$$

In a similar manner, the Euler-Almansi strain tensor is written as:

$$\mathbf{e} = \frac{1}{2}(\mathbf{I} - \mathbf{B}^{-1}) \quad (2.18)$$

at which they can be related through the deformation gradient, such that:

$$\mathbf{E} = \mathbf{F}^T \mathbf{e} \mathbf{F} \quad (2.19)$$

Following the infinitesimal deformation theory, $dv \approx dV$ and therefore $J \equiv \det \mathbf{F} \approx 1$. Hence, the Eulerian and Lagrangian strain tensors coincide and the infinitesimal strain tensor is given by:

$$\boldsymbol{\varepsilon} = \frac{1}{2}(\nabla_x \mathbf{u} + \nabla_x \mathbf{u}^T) \quad (2.20)$$

where $\nabla_x \mathbf{u}$ is the spatial gradient of the displacement field. It should be noted that the concepts that are discussed herein such as strains and stresses are defined mainly in a sufficiently large element of body which is primarily related to the smallest element of body that gives meaning to the existence of these elements, knowingly the representative volume element (RVE) of the body.

Another kinematical descriptor is the velocity gradient which may be defined in the current configuration as:

$$\mathbf{L} = \nabla_x \mathbf{v} = \dot{\mathbf{F}} \mathbf{F}^{-1} \quad (2.21)$$

By the additive decomposition of the velocity gradient into the symmetric and skew-symmetric parts, two kinematical descriptors may be defined in the following relation:

$$\mathbf{L} = \mathbf{D} + \mathbf{W} \quad (2.22)$$

where \mathbf{D} is called the rate of deformation or stretching tensor, given by:

$$\mathbf{D} = \frac{1}{2}(\mathbf{L} + \mathbf{L}^T) \quad (2.23)$$

and \mathbf{W} is known as the spin tensor, defined as

$$\mathbf{W} = \frac{1}{2}(\mathbf{L} - \mathbf{L}^T) \quad (2.24)$$

Following the assumption that material is a continuous media, the stress measures need to be defined in order to quantify the applied forces effect and the level of material degradation. Various measures of stress associated with the body or surface forces can be found in literature. Applying a force $d\mathbf{f}$ on a unit surface element (ds) in the current configuration, Cauchy or true stress tensor, $\boldsymbol{\sigma}$, is defined as a true quantity, which maps a unit outward normal vector \mathbf{N} in the current configuration to the relative surface traction vector, \mathbf{t} , such that:

$$\mathbf{t} = \frac{d\mathbf{f}}{ds} = \boldsymbol{\sigma}\mathbf{N} \quad (2.25)$$

Similarly, the nominal traction vector \mathbf{t}_0 can be expressed with respect to the reference surface element ds_0 as:

$$\mathbf{t}_0 = \frac{d\mathbf{f}}{ds_0} = \mathbf{P}\mathbf{N} \quad (2.26)$$

where \mathbf{P} is the first Piola-Kirchhoff stress tensor, which alternatively can be written as:

$$\mathbf{P} = J\mathbf{F}^{-T}\boldsymbol{\sigma} \quad (2.27)$$

The second Piola-Kirchhoff stress tensor is defined as:

$$\mathbf{S} = \mathbf{F}^{-1}\mathbf{P} = J\mathbf{F}^{-1}\boldsymbol{\sigma}\mathbf{F}^{-T} \quad (2.28)$$

which is a symmetric tensor.

2.2 Fundamental laws

The concepts of mass conservation and fundamental laws of thermodynamics in the context of continuum media are very briefly reviewed in this section. The information provided here indeed will be used in the process of material modelling and numerical implementation in the subsequent chapters.

2.2.1 Conservation of mass and momentum balance

The conservation of mass is postulated as

$$\dot{\mathfrak{D}} + \mathfrak{D} \operatorname{div}_x \dot{\mathbf{u}} = 0 \quad (2.29)$$

where \mathfrak{D} is the material density at the current configuration and div_x is the spatial divergence of the operator field. The momentum balance law for body \mathcal{B} may be mathematically represented in the spatial coordinates in the following form:

$$\operatorname{div}_x \boldsymbol{\sigma} + \mathbf{b} = \mathfrak{D} \ddot{\mathbf{u}} \quad (2.30)$$

Analogously, it may be expressed in the reference configuration in terms of the first Piola-Kirchhoff stress tensor, \mathbf{P} , as

$$\operatorname{div}_x \mathbf{P} + \bar{\mathbf{b}} = \bar{\mathfrak{D}} \ddot{\mathbf{u}} \quad (2.31)$$

where \mathbf{b} and $\bar{\mathbf{b}}$ are respectively the body force vector at the deformed and reference configurations, whereby $\bar{\mathbf{b}} = J\mathbf{b}$. In case of quasi-static problems, the inertial effects are neglected and by omitting the subscript x , Eq. (2.30) is rewritten as:

$$\operatorname{div} \boldsymbol{\sigma} + \mathbf{b} = \mathbf{0} \quad (2.32)$$

2.2.2 Laws of thermodynamics

The majority of ductile fracture concepts and the models of continuous damage mechanics are derived resorting to the thermodynamic concepts of the irreversible processes. The first law of thermodynamics that corresponds to the energy conservation reads:

$$\mathfrak{D} \dot{e} = \boldsymbol{\sigma} : \mathbf{D} + \mathfrak{D} \mathcal{r} - \operatorname{div} Q \quad (2.33)$$

where \dot{e} represents the rate of the specific internal energy, \mathcal{r} is the density of the heat production and Q stands for the heat flux. Regarding the isothermal mechanical processes, the above equation is reduced to

$$\mathfrak{D} \dot{e} = \boldsymbol{\sigma} : \mathbf{D} \quad (2.34)$$

which confirms that the rate of the internal energy per unit volume in the deformed state of the material must be equal to the stress power, $\boldsymbol{\sigma} : \mathbf{D}$, per unit deformed volume. Equivalently, this definition can be expressed in terms of the Kirchhoff stress tensor, $\boldsymbol{\tau}$, in the reference configuration as follows

$$\bar{\mathfrak{D}} \dot{e} = \boldsymbol{\tau} : \mathbf{D} \quad (2.35)$$

The second law of thermodynamics expresses the irreversible characteristic of the natural processes, which implies the irreversibility of the entropy production, as it is expressed by the following equation:

$$\mathfrak{D}T\dot{s} + \text{div}\mathbf{Q} - \mathfrak{D}r \geq 0 \quad (2.36)$$

being s the entropy of the system whereby T stands for the temperature. For an isothermal process, this equation is simplified as:

$$\mathfrak{D}T\dot{s} \geq 0 \quad (2.37)$$

With $\bar{\mathfrak{D}} = J\mathfrak{D}$, the inequality is written as:

$$\bar{\mathfrak{D}}T\dot{s} \geq 0 \quad (2.38)$$

Another thermodynamic definition is the Helmholtz free energy potential, representing the maximum work that a system can achieve under constant volume and temperature, given by:

$$\psi = e - Ts \quad (2.39)$$

By time differentiating the above equation we obtain

$$T\dot{s} = \dot{e} - \dot{\psi} \quad (2.40)$$

and combining Eqs. (2.26), (2.29) and (2.31) yields the Clausius-Duhem inequality:

$$\boldsymbol{\tau} : \mathbf{D} - \bar{\mathfrak{D}}\dot{\psi} \geq 0 \quad (2.41)$$

2.2.3 Constitutive theory

Most of the material models are derived based on a constitutive theory, in which the thermodynamic state of the material can be characterized by the set of state variables such as the deformation gradient, temperature or stresses. These variables are categorized as the observable and internal variables. Total strain and the displacement field are commonly observable variables and descriptors such as the plastic strains, equivalent plastic strain and damage are known as the internal variables which are associated with the dissipated energy. Following this concept, the material thermodynamic potential is commonly described via the free energy, whereby the forces conjugated to the state variables are determined. These expressions are complemented with the description of dissipative mechanism and the evolution laws for the internal variables described by their

rate forms. Based on the type of loading and the state of the problem, the choice of a suitable constitutive model is imperative.

For the problems in which material undergoes extensive plastic deformation after losing the initial load-carrying capacity, the *coupled* local approaches to fracture are a common choice to assess the level of the deformation and accumulation of damage. The term *coupled* in this context refers to the consideration of different deformation states for the plastic hardening and damage softening, in which these two phases are simultaneously considered in the constitutive model description.

These ductile fracture approaches mostly fall under the categories of the micromechanical or phenomenological approaches, in which the former class of methods is associated with the material models that describe the deformations in the microscopic scale, while the phenomenological models rely on the macrostructural material considerations. Several material models based on the concept of continuous damage mechanics (CDM) and micromechanical approaches are discussed in the next chapter, including the constitutive material model based on the Rousselier damage law which will be utilized as the basis for the phase-field extension of the ductile fracture model herein.

2.2.4 Heat transfer analysis

The thermal equilibrium differential equation for a n dimensional conducting body is expressed as:

$$\mathfrak{D}c_p \frac{\partial T}{\partial t} - \mathcal{K} \nabla^2(T) = Q \quad (2.42)$$

where $T(\mathbf{x}, t)$ is the temperature as the function of the position $\mathbf{x} \in \mathbb{R}^n$ and time t , c_p is the specific heat and \mathcal{K} is the thermal conductivity. This representation corresponds to the transient heat transfer (referring to the time dependence of the problem), and is a simplified version as neglects the effects of temperature on the specific heat and the thermal conductivity that is considered isotropic. The above problem is supplemented with the corresponding initial and boundary conditions and can be reduced to the following relation for steady state analysis, assuming null heat flux at the boundary:

$$\begin{cases} -\mathcal{K} \nabla^2(T) = Q \\ \partial_t T = 0 \end{cases} \quad (2.43)$$

The main body of research in this work neglects the temperature effects in the material softening phase. However, this section was presented due to an analogy that is made between the diffusion equation of the nonlocal gradient and the heat conduction problem which provides a more efficient basis for finite element implementation of such coupled gradient problems, in which the temperature serves as the diffusive field in the gradient approaches. This coupled temperature-displacement strategy was also recently addressed in [39] based on the damage initiation criterion that was presented in [40].

2.2.5 Initial boundary value problem and finite element method

The implementation of the material constitutive models essentially involved with using a suitable numerical method, as the analytical solutions in most of these models are not available or not easy to achieve due to their nonlinear nature. It is established to perform two numerical approximations on the initial boundary value problem: the time discretisation, i.e. the numerical integration of the constitutive relations and the spatial discretisation. Regarding the latter, the finite element method (FEM) is used throughout this work, in which the problem domain is discretised to a finite number of elements (readers are referred to [41,42] for an overview of the method). It is a common practice in this context to obtain the weak form of the initial boundary value problem (IBVP) and then perform the finite element approximation, which is for instance followed in the implementation of the phase-field approach in the subsequent chapters.

Using the infinitesimal strain approach and given the history of total strain tensor $\varepsilon(t)$ where $t \in [t_0, T]$, the IBVP is to find the stress and set of internal variables α as:

$$\begin{cases} \boldsymbol{\sigma}(t) = \bar{\rho} \frac{\partial \psi}{\partial \varepsilon} \\ \dot{\alpha}(t) = f^*(\varepsilon(t), \alpha(t)) \end{cases} \quad (2.44)$$

The second equation involves with the evolution of the internal variables, in which the rate of the internal variable $\dot{\alpha}$ is described by a function f^* . Finding the weak form of the above problem using for instance the principle of virtual work is the initial point for performing the finite element method. Herein the displacement-based finite element framework is briefly reviewed.

The stress as a function of the displacement field enters the following initial boundary value problem in weak form as:

$$\int_{\Omega} [\boldsymbol{\sigma}(\boldsymbol{\varepsilon}(\mathbf{u})) : \nabla \delta \mathbf{u} - \mathbf{b} \delta \mathbf{u}] d\Omega - \int_{\partial\Omega} \bar{\mathbf{t}} ds = 0 \quad (2.45)$$

being $\delta \mathbf{u}$ the virtual displacement. The spatial discretisation of the above problem is performed by determining the discretised displacement field \mathbf{u}^h by interpolating the displacement field \mathbf{u} , using interpolation functions, i.e., at the element level the shape function $N_i^e(x_i)$, such that:

$$\mathbf{u}^h = \sum_{i=1}^{n_{node}} N_i^e \mathbf{u}_i \quad (2.46)$$

where $N_i^e(\mathbf{x}^i)$ is associated with the node i of element e whose coordinate is \mathbf{x}^i , and the total number of the nodes for the element is denoted by n_{node} . The shape function $N_i^e(\mathbf{x}^i)$ is defined in a way that its value at node i is unity, i.e. $N_i^e(\mathbf{x}^i) = 1$, and zero at other nodes of the element, means $N_i^e(\mathbf{x}^j) = 0$ for $j \neq i$. Over the entire problem domain Ω , the finite element discretisation is conducted with a mesh consisting of total number of elements denoted by n_{elem} , such that:

$$\Omega^h = \bigcup_{e=1}^{n_{elem}} \Omega^e \quad (2.47)$$

The discretised displacement field thus defined globally as:

$$\mathbf{u}^h = \sum_{i=1}^{n_{point}} N_i^g \mathbf{u}_i \quad (2.48)$$

where N_i^g is the global shape function and n_{point} is the total number of the nodal points in the mesh topology. The global shape function matrix is given by:

$$[N_i^g] = \begin{bmatrix} N_i^g & 0 & \dots & 0 \\ 0 & N_i^g & \dots & 0 \\ & & \ddots & \\ 0 & 0 & \dots & N_i^g \end{bmatrix} \quad (2.49)$$

Having defined the global displacement field vector as

$$\{\mathbf{u}\} = \{u_1^1, \dots, u_{n_{dim}}^1, \dots, u_1^{n_{point}}, u_{n_{dim}}^{n_{point}}\}^T \quad (2.50)$$

where n_{dim} is the number of the element dimensions and u_i^j being the i th component of the displacement vector at the global node j , the discretised displacement field and its virtual counterpart can be represented by:

$$\{\mathbf{u}\}^h = [N^g]\{\mathbf{u}\} \quad , \quad \{\delta\mathbf{u}\} = [N^g]\{\delta\mathbf{u}\} \quad (2.51)$$

where

$$\{\delta\mathbf{u}\} = \left\{ \delta u_1^1, \dots, \delta u_{n_{dim}}^1, \dots, \delta u_1^{n_{point}}, \delta u_{n_{dim}}^{n_{point}} \right\}^T \quad (2.52)$$

To determine the gradient operator, the global displacement symmetric gradient operator or B matrix is written as:

$$[B^g] = \begin{bmatrix} N_{1,1}^g & 0 & N_{2,1}^g & 0 & \dots & N_{n_{point},1}^g & 0 \\ 0 & N_{1,2}^g & 0 & N_{2,2}^g & \dots & 0 & N_{n_{point},2}^g \\ N_{1,2}^g & N_{1,1}^g & N_{2,2}^g & N_{2,1}^g & \dots & N_{n_{point},2}^g & N_{n_{point},1}^g \end{bmatrix} \quad (2.53)$$

where $(.)_{i,j} = \frac{\partial(.)}{\partial x_j}$. it should be noted that the above gradient operator is applicable for 2D problems of plane stress or plane strain and axisymmetric configurations. With the above definitions, the initial boundary value problem of Eq. (2.45) is written in discrete form as:

$$\int_{\Omega^h} [\boldsymbol{\sigma}^T [B^g]\{\delta\mathbf{u}\} - \mathbf{b} \cdot [N^g]\{\delta\mathbf{u}\}] d\Omega - \int_{\partial\Omega^h} t \cdot [N^g]\{\delta\mathbf{u}\} ds = 0 \quad (2.54)$$

By rearranging the above expression one can obtain the following equation:

$$\left\{ \int_{\Omega^h} [[B^g]^T \boldsymbol{\sigma} - [N^g]^T \mathbf{b}] d\Omega - \int_{\partial\Omega^h} [N^g]^T t ds \right\}^T \{\delta\mathbf{u}\} = 0 \quad (2.55)$$

Where one should bear in mind that the stress tensor is a function of strain tensor and thus the displacement field. By determining the global internal force (f^{int}) and external force (f^{ext}) as:

$$f^{int} = \int_{\Omega^h} [B^g]^T \boldsymbol{\sigma} d\Omega \quad , \quad (2.56)$$

$$f^{ext} = \int_{\Omega^h} [N^g]^T \mathbf{b} d\Omega + \int_{\partial\Omega^h} [N^g]^T t ds$$

the finite element problem is established based on the following boundary value problem:

$$f^{int} - f^{ext} = 0 \quad (2.57)$$

where the internal force is the function of the displacement field. In subsequent chapters, the above finite element procedure is utilised for the solution of the phase-field evolution equation.

3 Local approaches to ductile fracture

3.1 Physical background

At the microstructural scale, the ductile fracture phenomenon is characterised by a sequential material degradation, consisting of nucleation, growth and coalescence of the micro-voids or micro-cavities in the material bulk, as illustrated in Figure 3.1. Nucleation of the voids occurs at the inclusions or second-phase particles, due to the particle cracking or decohesion of the matrix/inclusion interface. Increasing the level of plastic deformations in the surrounding matrix propels the micro-voids growth, through the dilatation or elongation of the voids, respectively predominant in high and low levels of triaxiality.

In shear-dominated loading situations connected to low stress triaxiality, void nucleation is more commonly observed at the secondary voids, i.e. a smaller population of the voids created between the primary voids, which coins the term “void-sheeting” for this type of failure. This mechanism is described as one of the primary causes of void coalescence in low triaxialities, which is associated with the accelerated internal material deterioration through the formation of *shear bands*. In high triaxialities, the void internal necking is typically observed, whereby two adjacent voids are merged following the reduction of inter-void ligament, driving the micromechanical failure process to the final material rupture. For further details in this subject, readers are referred to [43] that gives an extensive review over the continuum approaches to fracture including the discussions on the micromechanical description of material failure.

Despite the fact that several physical aspects of fracture such as void shape, size or orientation could be of importance in the crack analyses, the mathematical models are often established based on simplified assumptions and approximations that can reduce the computational costs and complexity of the models.

Early material models described failure process via linking the cavity growth to the hydrostatic pressure, hence referred to as *void growth models* (VGM) in literature. The models by McClintock [44] and Rice & Tracy [45], respectively developed for isolated cylindrical and spherical cavities in an infinite rigid perfectly plastic material matrix.

These models were defined based on definition of a critical value for cavity growth rate which is considered as a characteristic of the material model. Rice & Tracy [45] found that the spherical cavity growth in a non-hardening material and under high levels of triaxiality can be approximated by the following relation:

$$\ln\left(\frac{r}{r_0}\right) = 0.283 \int \exp\left(\frac{3\sigma_m}{2q}\right) d\bar{\varepsilon}^p \quad (3.1)$$

where r is the mean radius of cavity, r_0 is the initial radius of the cavity, the ratio σ_m/q defines the stress triaxiality and $\bar{\varepsilon}^p$ is the equivalent plastic strain. The above relation essentially constructs a linear relation between the cavity growth and the equivalent plastic strain rate. However, the constant value of 0.283 was found to be not an optimised value, as it was reported in subsequent efforts that it underestimates the crack growth. Also the lack of nucleation and coalescence mechanisms led to several other modified versions of this model thereafter.

The VGM models are essentially characterised under the category of *uncoupled* fracture criteria, hinting that there is no coupling between plasticity and damage at any level, and, therefore, the influence of damage on the yield surface of the material model is neglected. However, these material models are widely accepted in the engineering community due to its simplicity in mathematical description and calibration procedure.

Later on, more physically-sound ductile fracture criteria were proposed at which the internal material degradation could be quantified via a scalar internal variable interpreted as the damage variable. These *coupled* models are often categorised either as the phenomenological approaches in ductile damage within the continuous damage mechanics framework or the micromechanically-motivated approaches.

The former class of models, such as the one developed by Lemaitre [46] or Lemaitre and Chaboche [47,48], are typically classified under the theory of continuous damage mechanics (CDM). These models are based on a continuous description of the damage and internal variables that are defined at the microscopic scale.

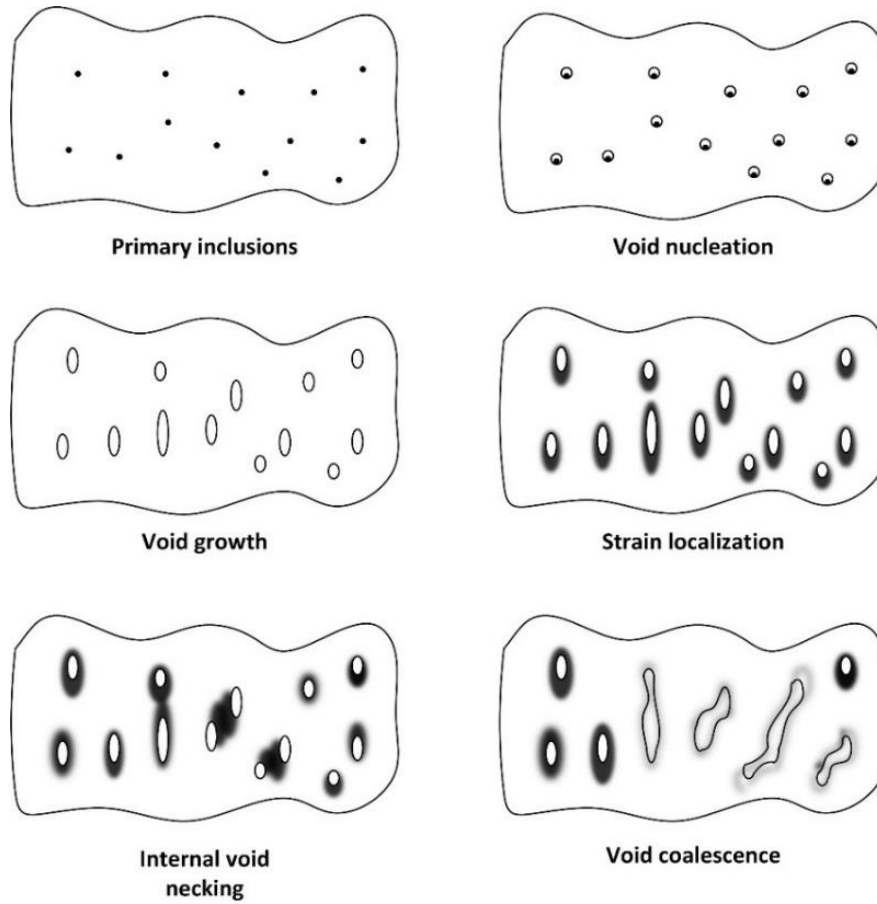


Figure 3.1 Micromechanical evolution of ductile fracture

Micromechanical approaches on the other hand were developed in the context of porous materials in the early work of Gurson [19] and its subsequent extended version [49], through analysis of a finite sphere containing a spherical void in a medium of a perfectly rigid plastic material matrix. In this family of material models, value of void volume fraction, i.e. porosity, quantifies the internal material degradation and thus the level of material loss of load-carrying capacity.

Coming from thermodynamical backgrounds, the pressure-dependent plasticity model by Rousselier [23,24] modified the yield potential of the classical von Mises plasticity in a similar manner to the Gurson-based models, at which a damage dissipation term based on the cavity growth is added to the flow potential. Unlike the Gurson model, the damage is still generated in Rousselier model even under pure shear condition the vertex of the its flow potential confirms a non-zero shear component for the plastic deformation under high levels of triaxiality.

This chapter discusses the main ingredients of the local damage models used in the present work, by discussing their thermodynamical description and mathematical framework of their constitutive modelling. The model of Lemaitre and its integration procedure in finite element framework is explained briefly in the following section. Next, the Rousselier damage criterion as the mostly used ductile fracture framework herein is revisited.

3.2 Mathematical models in ductile failure

The models that are based on the physical description of fracture are often referred to as the *local approaches* to fracture, are defined, at each material point, on the basis of a fracture criterion resulting from micro-crack/meso-crack analyses. Within this context, the coupled approaches, where a coupling between the plastic deformations and the damage softening is established, are of main concern in this study. The constitutive model of these approaches is typically derived from thermodynamical considerations and the definition of the free Helmholtz energy and it is accompanied by evolution of the internal variables and macroscopic criteria.

Within the framework of continuous media, the material progressive degradation may be characterised by introducing an evolving scalar damage variable at the macroscopic level representation and material failure is then described in a phenomenological way, in the field of continuous damage mechanics, one of the most popular frameworks for the assessment of material internal degradation through the course of last three decades.

Since the early work of Kachanov [50] in creep rupture, several authors made a connection between a scalar damage variable and the reduction, at the mesoscale, of the material load resisting area, defining the effective resisting area, \bar{S} , as:

$$\bar{S} = S - S_D \quad (3.2)$$

where S_D is the area of cavities with S as the area of the intact material. Figure 3.2 schematically represents the effective area in a damaged element. An effective stress $\bar{\sigma}$, a concept originated from the early work of Kachanov, is thus defined as:

$$\bar{\sigma} = \frac{\sigma}{1 - \mathcal{D}} \quad (3.3)$$

and the isotropic damage variable is given by:

$$\mathcal{D} = \frac{S - \bar{S}}{S} \quad (3.4)$$

The material internal degradation in this context is described as the density of micro-cavities and micro-voids, based on the above isotropic scalar damage parameter, $0 \leq \mathcal{D} \leq 1$, evolving continuously from zero (intact material) to one (fully damaged material). This class of models are referred to as phenomenological as the internal damage variable affects the macroscopic material properties, such as the elastic moduli.

3.2.1 Constitutive framework of the Lemaitre's damage criterion

The constitutive relations for the Lemaitre and subsequent damage models are mostly derived based on the thermodynamic principles and rules of the continuous media as described in the previous chapter, at which the state of the material can be determined by a set of *observable* and *internal* variables.

The Lemaitre's ductile damage framework is established based on coupling between the material elastoplastic deformation with the degradation mechanism induced by the damage softening term. This model uses the concept of effective stress and the hypothesis of strain equivalence, in which the effective stress tensor substitutes the usual stress tensor at the constitutive equations. In the following, the mathematical descriptions and standard notations are used, in a close agreement with the ones in [51].

The derivation of the constitutive model in elastoplastic solids is commonly described by the additive decomposition of the strain tensor as follows:

$$\boldsymbol{\varepsilon} = \boldsymbol{\varepsilon}^e + \boldsymbol{\varepsilon}^p \quad (3.5)$$

where $\boldsymbol{\varepsilon}^e$ and $\boldsymbol{\varepsilon}^p$ are the elastic and plastic strain tensors, respectively. Following the thermodynamic principles of irreversible processes, the Helmholtz free energy of the damaged material can be expressed by the elastic-damageable (ψ_{ed}) and plastic (ψ_p) components as:

$$\psi = \psi_{ed}(\boldsymbol{\varepsilon}^e, \mathcal{D}) + \psi_p(\alpha) \quad (3.6)$$

The elastic-damageable contribution reads:

$$\psi_{ed}(\boldsymbol{\varepsilon}^e, \mathcal{D}) = \frac{1}{2} \boldsymbol{\varepsilon}^e : (1 - \mathcal{D}) \mathbf{D}^e : \boldsymbol{\varepsilon}^e \quad (3.7)$$

where \mathbf{D}^e is the fourth order elastic tangent matrix given by:

$$\mathbf{D}^e = 2G\mathbf{I}_d + K\mathbf{I}:\mathbf{I} \quad (3.8)$$

where G and K are the shear and bulk moduli, respectively and $\mathbf{I}_d = \mathbf{I}_s - \frac{1}{3}\mathbf{I}:\mathbf{I}$ is the fourth order deviatoric projection tensor based on the symmetric identity tensor, at which for 2D plane problems it is expressed by:

$$\mathbf{I}_s = \begin{bmatrix} 1 & 0 & 0 \\ & 1 & 0 \\ sym & & \frac{1}{2} \end{bmatrix} \quad (3.9)$$

The Cauchy stress tensor may be obtained as:

$$\boldsymbol{\sigma} = \partial_{\boldsymbol{\varepsilon}^e}(\psi) = (1 - \mathcal{D})\mathbf{D}^e : \boldsymbol{\varepsilon}^e \quad (3.10)$$

being $\partial_{\boldsymbol{\varepsilon}^e}$ the derivative with respect to the elastic strain tensor, $\boldsymbol{\varepsilon}^e$. The material plastic admissibility condition is verified by the following yield limit:

$$\varphi = \frac{q}{1 - \mathcal{D}} - R(\alpha) = 0 \quad (3.11)$$

where q is the von Mises equivalent stress and $R(\alpha)$ is the hardening function based on the internal hardening variable denoted by α .

The material isotropic hardening curve is characterised by $R(\alpha)$ and the hardening variable is commonly chosen as the equivalent plastic strain denoted by $\bar{\varepsilon}^p$ herein. This variable can be determined based on the rate of the plastic multiplier, $\dot{\gamma}$, at which the plasticity flow rule gives $\dot{\alpha} = \dot{\gamma}$. The force conjugated to the damage variable is calculated as:

$$Y = \partial_{\mathcal{D}}(\varphi) = -\frac{1}{2} \boldsymbol{\varepsilon}^e : \mathbf{D}^e : \boldsymbol{\varepsilon}^e \quad (3.12)$$

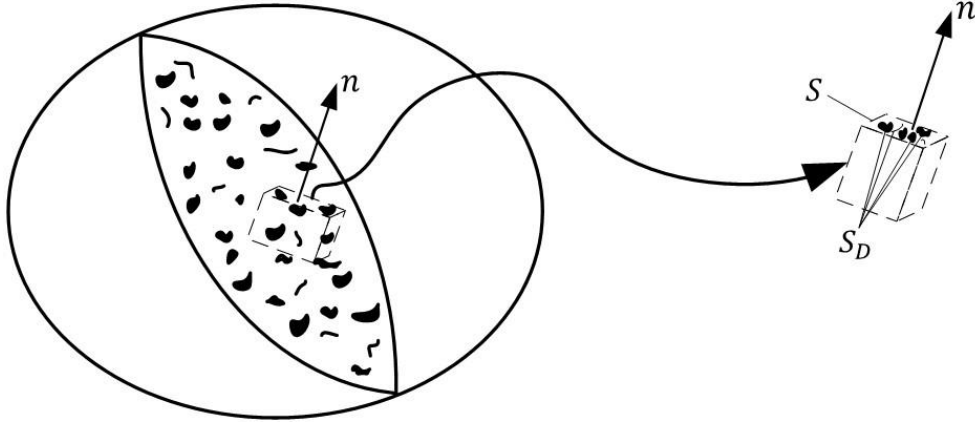


Figure 3.2 Illustration of a damaged element

The variable $-Y$ is more commonly known as the damage energy release rate and one can alternatively obtain the following expression:

$$Y = \frac{1}{(1 - \mathcal{D})^2} \left(\frac{-q^2}{6G} - \frac{p^2}{2K} \right) \quad (3.13)$$

where the product $Y\dot{\mathcal{D}}$ is described as the dissipated power due to the damage evolution, which can be given by the following rate form:

$$\dot{\mathcal{D}} = \frac{r_1}{(1 - \mathcal{D})(1 + r_2)} \left(-\frac{Y}{r_1} \right)^{r_2+1} \quad (3.14)$$

In the above relation, r_1 and r_2 are model parameters that affect the level of material degradation and require calibration based on the experimental observations. This model is complemented by the following loading/unloading conditions:

$$\varphi < 0; \quad \dot{\gamma} \geq 0; \quad \dot{\gamma}\varphi = 0 \quad (3.15)$$

The above constitutive model relations are summarized in Box 3.1.

Characterisation of the stress states

The concepts that are revisited in this section are applicable to the following material models of this study. It is a common practice in most of the constitutive models that the state of stress is determined based on the invariants of the Cauchy stress, given by:

$$\begin{aligned} I_1 &= -3p = \sigma_1 + \sigma_2 + \sigma_3 \\ I_2 &= \frac{1}{3}q^2 = \frac{1}{2}\mathbf{s}:\mathbf{s} = \frac{1}{6}[(\sigma_1 - \sigma_2)^2 + (\sigma_2 - \sigma_3)^2 + (\sigma_3 - \sigma_1)^2] \\ I_3 &= \det(\mathbf{s}) = s_1 s_2 s_3 \end{aligned} \quad (3.16)$$

where for $i=1,2,3$, I_i values are the invariants of the stress tensor, σ_i and s_i are respectively the principal values of the total and deviatoric stress tensors, $p = -\frac{1}{3}\boldsymbol{\sigma}:\mathbf{I}$ is the hydrostatic pressure, $q = \sqrt{\frac{3}{2}\mathbf{s}:\mathbf{s}}$ is the equivalent von Mises stress and the vector normal to the von Mises yield surface is defined as $\mathbf{N} = \frac{3}{2q}\mathbf{s}$. The hydrostatic and deviatoric invariants of the stress tensor are respectively correspond to the material deformation due to dilatation and distortion, such that:

$$\boldsymbol{\sigma} = \mathbf{s} + p\mathbf{I} \quad (3.17)$$

In the context of ductile metallic materials, new studies suggest that apart from the hydrostatic pressure, the influence of the third invariant of the deviatoric stress, through the designated Lode parameter, specially at low stress triaxiality states, should be considered in the models of ductile fracture [52]. In regards with this, a relation between the stress triaxiality, η^* , or often referred to as *triaxiality*, the Lode parameter ξ and the equivalent strain to fracture can be established. The interaction of the void volume fraction and the stress triaxiality in a peak-aged 6061 aluminium alloy was initially defined through establishing an empirical damage evolution law in [53]. Among other studies, the influence of triaxiality on the damage evolution and strain to rupture was shown in [45,54].

The triaxiality parameter is defined as:

$$\eta^* = \frac{-p}{q} = \frac{\sigma_m}{q} \quad (3.18)$$

where σ_m is the mean stress that is positive in tension as opposed to p that is positive in compression. The Lode angle θ is linked to the normalized third invariant of the deviatoric stress by:

$$\xi = \frac{27}{2} \frac{I_3}{q^3} = \cos(3\theta) \quad (3.19)$$

Having defined a possible variation for the Lode angle such that $0 \leq \theta \leq \pi/3$, the normalized third invariant varies between $-1 \leq \xi \leq 1$. In a large body of research studies such as [52], a normalized Lode angle parameter $-1 \leq \bar{\theta} \leq 1$ is used instead of Lode angle, that reads:

$$\bar{\theta} = 1 - \frac{6\theta}{\pi} \quad (3.20)$$

Though the influence of triaxiality is not directly introduced into the damage model description of the present research, the variation of this parameter is addressed very briefly in numerical analysis of round bars in chapter 5 due to comparison with the literature data.

Box 3.1. Constitutive relations of the Lemaitre ductile damage model

Elastoplastic decomposition of the strain rate:

$$\boldsymbol{\varepsilon} = d\boldsymbol{\varepsilon}^e + d\boldsymbol{\varepsilon}^p$$

Elastic damage law:

$$\boldsymbol{\sigma} = (1 - D)\mathbf{D}^e : \boldsymbol{\varepsilon}^e$$

Yield potential to verify plastic admissibility condition:

$$\varphi(\boldsymbol{\sigma}, D) = \frac{q}{1 - D} - R(\alpha)$$

Plastic flow rule:

$$d\boldsymbol{\varepsilon}^p = d\gamma \frac{\partial \varphi}{\partial \boldsymbol{\sigma}} = d\gamma N \text{ where } N = \sqrt{\frac{3}{2(1 - D)}} \frac{\mathbf{s}}{\|\mathbf{s}\|}$$

Evolution of the internal variables:

$$dR = d\gamma$$

$$dD = \frac{d\gamma}{1 - D} \left(\frac{-Y}{r_1} \right)^{r_2}$$

Loading/unloading conditions

$$d\gamma \geq 0 ; \quad \varphi \leq 0 ; \quad d\gamma \cdot \varphi = 0$$

Integration procedure of the Lemaitre's damage criterion:

The numerical integration of the above constitutive equations may be expressed via a fully-implicit return mapping algorithm. In this work, the simplified and efficient one-equation return mapping procedure proposed in [51] is used which requires rather lower computational cost, compared to the algorithm in [55] where 15 equations were required to be solved. By performing the temporal discretization of the problem, the algorithm starts with an elastic predictor stage and by reaching the prescribed yield limit, the return mapping solution strategy is applied.

Considering a pseudo time interval $\Delta t = t_{n+1} - t_n$, the values of internal and state variables $(\boldsymbol{\sigma}_n, \boldsymbol{\varepsilon}_n^p, \alpha_n, \mathcal{D}_n)$ should be updated to the values at the end of the time increment $(\boldsymbol{\sigma}_{n+1}, \boldsymbol{\varepsilon}_{n+1}^p, \alpha_{n+1}, \mathcal{D}_{n+1})$ using the constitutive relations discussed in the section 3.2.1. Given the value of the strain increment $(\Delta \boldsymbol{\varepsilon})$ corresponding to the time interval, the trial elastic strain tensor (the superscript *tr* refers to the trial material state henceforth) is defined by:

$$\boldsymbol{\varepsilon}_{n+1}^{e\ tr} = \boldsymbol{\varepsilon}_n^e + \Delta \boldsymbol{\varepsilon} \quad (3.21)$$

The trial stress tensor is calculated as:

$$\boldsymbol{\sigma}_{n+1}^{tr} = (1 - \mathcal{D}_n) \mathbf{D}^e \boldsymbol{\varepsilon}_{n+1}^{e\ tr} \quad (3.22)$$

which can be split into the following form:

$$\mathbf{s}_{n+1}^{tr} = (1 - \mathcal{D}_n) 2G \boldsymbol{\varepsilon}_{d\ n+1}^{e\ tr} ; \quad \bar{p}_{n+1}^{tr} = (1 - \mathcal{D}_n) K \boldsymbol{\varepsilon}_{v\ n+1}^{e\ tr} \quad (3.23)$$

where $\boldsymbol{\varepsilon}_{d\ n+1}^{e\ tr}$ and $\boldsymbol{\varepsilon}_{v\ n+1}^{e\ tr}$ are respectively the trial deviatoric and volumetric parts of the elastic strain tensor at the current time increment, where $p_{n+1} = K \boldsymbol{\varepsilon}_{v\ n+1}^{e\ tr}$. By defining the trial von Mises equivalent stress as:

$$\bar{q}_{n+1}^{tr} = \frac{q_{n+1}^{tr}}{1 - \mathcal{D}_n} = \frac{\sqrt{\frac{3}{2} \mathbf{s}_{n+1}^{tr} : \mathbf{s}_{n+1}^{tr}}}{1 - \mathcal{D}_n} \quad (3.24)$$

the corresponding yield function is given by:

$$\varphi^{tr} = \bar{q}_{n+1}^{tr} - R(\alpha) \quad (3.25)$$

at which the material experiences purely elastic regime for $\varphi^{tr} \leq 0$ and hence, the updated values of the state variables are chosen to be those at the beginning of the time increment. Upon the state where $\varphi^{tr} > 0$, the return mapping algorithm is activated based on the following set of evolution equations:

$$\boldsymbol{\varepsilon}_{n+1}^e = \boldsymbol{\varepsilon}_{n+1}^{e\ tr} - \Delta \gamma \sqrt{\frac{3}{2} \frac{\mathbf{s}_{n+1}}{(1 - \mathcal{D}_{n+1}) \|\mathbf{s}_{n+1}\|}} \quad (3.26)$$

$$\bar{\varepsilon}_{n+1}^p = \bar{\varepsilon}_n^p + \Delta \gamma \quad (3.27)$$

$$\mathcal{D}_{n+1} = \mathcal{D}_n + \frac{\Delta \gamma}{1 - \mathcal{D}_{n+1}} \left(\frac{-Y_{n+1}}{r_1} \right)^{r_2} \quad (3.28)$$

$$\frac{q_{n+1}}{1 - \mathcal{D}_{n+1}} - R(\bar{\varepsilon}_{n+1}^p) = 0 \quad (3.29)$$

Following the procedure adopted in [51], a material *integrity* is defined as:

$$\omega \equiv 1 - \mathcal{D} \quad (3.30)$$

The initial guess for the variation of the plastic multiplier is given by:

$$\Delta\gamma^{(0)} = \frac{[q^{tr} - \sigma_y(\bar{\varepsilon}_n^p)\omega_n]}{3G} \quad (3.31)$$

The single equation implicit return mapping functional for solving $\Delta\gamma$ is expressed as:

$$\omega(\Delta\gamma) - \omega_n + \frac{\Delta\gamma}{\omega(\Delta\gamma)} \left(\frac{-Y(\Delta\gamma)}{r_1} \right)^{r_2} = 0 \quad (3.32)$$

with

$$\omega_{n+1} = \omega(\Delta\gamma) \equiv \frac{3G\Delta\gamma}{\bar{q}_{n+1}^{tr} - \sigma_y(\bar{\varepsilon}_n^p + \Delta\gamma)} \quad (3.33)$$

and

$$-Y(\Delta\gamma) \equiv \frac{[\sigma_y(\bar{\varepsilon}_n^p + \Delta\gamma)]^2}{6G} + \frac{p_{n+1}^2}{2K} \quad (3.34)$$

The above integration algorithm is summarized in Box 3.2.

The nonlinear function expressed in Eq. (3.32) is solved using the Newton Raphson iterative scheme and upon the time that the algorithm is converged, the updated value of plastic multiplier is used to in the evolution equations for the state variables.

In the present material model, the inclusion of the damage threshold is considered. This can be evaluated based on a critical value of the equivalent plastic strain denoted by $\bar{\varepsilon}_c^p$, which is introduced to the model as a material parameter. Accordingly, the above return mapping procedure is applied only for $\bar{\varepsilon}^p \geq \bar{\varepsilon}_c^p$. Therefore, the von Mises plasticity algorithm is considered for the material state before the critical plastic strain. The mathematical description of the von Mises plasticity as well as the derivation of the plastic tangent modulus consistent with the isotropic plasticity or the above return mapping algorithm are not discussed herein and interested readers are referred to [51] for a detailed representation of these subjects. Implementation of the above return mapping algorithm is coded implicitly in user material module (UMAT) in ABAQUS that includes the stress update procedure and determination of the consistent tangent modulus. The calculations are carried out at in an incremental manner, where the updated values for state variables including the stresses and internal variables (hardening and damage variables) are

obtained at the material point level. In the subsequent chapters, this model is used for evaluation of the internal damage and fracture in a limited number of examples

Box 3.2. Integration procedure for solution of the Lemaitre ductile damage model

1. Determine the elastic trial strain

$$\boldsymbol{\varepsilon}_{n+1}^{e\ tr} = \boldsymbol{\varepsilon}_n^e + \Delta \boldsymbol{\varepsilon}$$

2. Coupled elastic-damageable equilibrium equation

$$\boldsymbol{\sigma}_{n+1}^{tr} = (1 - D_n) \mathbf{D}^e \boldsymbol{\varepsilon}_{n+1}^{e\ tr}$$

3. Deviatoric/hydrostatic stress components

$$\mathbf{s}_{n+1}^{tr} = (1 - D_n) 2G \boldsymbol{\varepsilon}_{n+1}^{e\ tr} ; \quad p_{n+1}^{tr} = (1 - D_n) K \boldsymbol{\varepsilon}_{n+1}^{e\ tr}$$

4. Determine the von Mises equivalent stress

$$\bar{q}_{n+1}^{tr} = \frac{\sqrt{\frac{3}{2} \mathbf{s}_{n+1}^{tr} : \mathbf{s}_{n+1}^{tr}}}{1 - D_n}$$

5. Verify the plastic admissibility condition through the following yield limit:

If $(\bar{q}_{n+1}^{tr} - R(\bar{\varepsilon}_{n+1}^{p\ tr}) \leq 0)$ then

$$(\cdot)_{n+1} = (\cdot)_{n+1}^{tr}$$

Elseif $(\bar{\varepsilon}_{n+1}^{p\ tr} \geq \bar{\varepsilon}_c^p)$ then von Mises isotropic plasticity problem to solve for the unknown $\Delta\gamma$ using Newton Raphson iterative scheme

$$\bar{F}(\Delta\gamma) = \bar{q}_{n+1}^{tr} - 3G\Delta\gamma - R(\bar{\varepsilon}_{n+1}^{p\ tr}) = 0$$

Else go to 6

6. Solve the following return mapping for the unknown $\Delta\gamma$ using Newton Raphson:

$$\bar{F}(\Delta\gamma) \equiv \omega(\Delta\gamma) - \omega_n + \frac{\Delta\gamma}{\omega(\Delta\gamma)} \left(\frac{-Y(\Delta\gamma)}{r_1} \right)^{r_2} = 0$$

$$\text{where } \omega_{n+1} = \omega(\Delta\gamma) \equiv \frac{3G\Delta\gamma}{\bar{q}_{n+1}^{tr} - \sigma_y(\bar{\varepsilon}_n^p + \Delta\gamma)}$$

$$-Y(\Delta\gamma) \equiv \frac{[\sigma_y(\bar{\varepsilon}_n^p + \Delta\gamma)]^2}{6G} + \frac{p_{n+1}^2}{2K}$$

7. Update the state variables:

$$\left\{ \begin{array}{l} \bar{\varepsilon}_{n+1}^p = \bar{\varepsilon}_n^p + \Delta\gamma \\ \bar{p}_{n+1} = \omega(\Delta\gamma) p_{n+1} ; \quad q_{n+1} = \omega(\Delta\gamma) \sigma_y(\bar{\varepsilon}_n^p + \Delta\gamma) \\ s_{n+1} = \frac{q_{n+1}}{\bar{q}_{n+1}} \mathbf{s}_{n+1}^{tr} ; \quad \boldsymbol{\sigma}_{n+1} = \mathbf{s}_{n+1} + p_{n+1} \mathbf{I} \\ \boldsymbol{\varepsilon}_{n+1}^e = \frac{1}{2G} \mathbf{s}_{n+1} + \frac{1}{3} \boldsymbol{\varepsilon}_{n+1}^e \mathbf{I} \end{array} \right.$$

3.2.2 Gurson-based damage models

The early development of the ductile fracture in the framework of porous solids is traced back to the work of Gurson [19], based on the growth of an isolated finite spherical cavity (or void) inside a plastically incompressible matrix of material. According to this criterion, a coupling between the macroscopic stresses and the volume fraction of the voids is established based on the following plastic potential:

$$\phi = \frac{q^2}{\sigma_0^2} + 2f \cosh\left(\frac{3p}{2\sigma_0}\right) - 1 - f^2 \quad (3.35)$$

where σ_0 is the current equivalent stress representing the flow of the undamaged matrix of the material and f is the void volume fraction representing the damage parameter in this context. The material softening is driven by the growth of the void volume fraction until $f = 1$, which can be determined from the above yield surface by having zero stress carrying capacity, i.e. $\sigma = 0$.

This model is only applicable for the problems with pre-existing cracks, where the rate of void volume fraction can be described under the premise of material matrix incompressibility as:

$$\dot{f} = (1 - f)tr(\dot{\varepsilon}^p) + A\dot{\bar{\varepsilon}}^p \quad (3.36)$$

where $\dot{\varepsilon}^p$ is the rate of the plastic strain that will be discussed more in the subsequent section. In the above relation, the first term corresponds to the growth of the voids, whereby the nucleation is primarily driven by the rate of the equivalent plastic strain in the second term multiplied by the coefficient A given by:

$$A = \frac{f_N}{s_N\sqrt{2\pi}} \exp\left[\frac{-1}{2}\left(\frac{\bar{\varepsilon}^p - \varepsilon_N}{s_N}\right)^2\right] \quad (3.37)$$

where f_N is the volume fraction of the nucleating voids, ε_N is the mean equivalent plastic strain and s_N is the standard deviation of the distribution. The Gurson model was enhanced by Tvergaard and Needleman [49], where nucleation and coalescence void mechanisms were added to the model according to phenomenological considerations. This criterion commonly known as GTN damage criterion can be expressed by modifying the yield potential expressed in Eq. (3.35) as:

$$\phi = \frac{q^2}{\sigma_0^2} + 2q_1 f^* \cosh\left(\frac{3q_2 p}{2\sigma_0}\right) - 1 - q_3 f^{*2} \quad (3.38)$$

with q_1 , q_2 and q_3 as the GTN model parameters in which they were introduced to take into consideration the void interaction effects. Although these parameters have to be identified following the experimental observations, it is a common practice to use $q_1 = 1.5$, $q_2 = 1.0$ and $q_3 = q_1^2 = 2.25$ based on the study in [56] where authors obtain the values by fitting the results with the unit cell model. The definition of flow stress in the yield surface expression may provide the link to the isotropic plasticity hardening and hence the evolution of the equivalent plastic strain.

The coalescence mechanism has a major influence in the material loss of load-bearing capacity and is modelled via definition of the *effective porosity* value, f^* , through the following failure criterion:

$$f^* = \begin{cases} f & \text{if } f \leq f_c \\ f_c + \frac{\bar{f}_f - f_c}{f_f - f_c} (f - f_c) & \text{if } f_c < f < f_f \\ \bar{f}_f & \text{if } f \geq f_f \end{cases} \quad (3.39)$$

being $\bar{f}_f = \frac{q_1 + \sqrt{q_1^2 - q_3}}{q_3}$, f_c the critical void volume fraction and f_f the value of void volume fraction at which the material is fully broken. Notice that for $f^* = 0$, the standard isotropic plasticity model is recovered.

The above mathematical model can be implemented via finite element method where with the above definitions, the total number of 9 model parameters may require to be identified, including the void interaction parameters. Several enhanced versions of the GTN model have been proposed by different authors as there are some limitations of the original model posed in numerical modelling of fracture. Among these, the model is extended to capture damage localisation in low triaxialities by adding a shear term in the void volume fraction rate description in [20]. Nevertheless, the GTN model has been highly regarded in the scientific community to date and the in its original format can be traced and utilised in finite element packages, for instance in Abaqus material library.

3.2.3 Rousselier damage model

The phenomenological ductile damage model of Rousselier [23,24] is developed based on the generalised continuum mechanics and thermodynamical considerations. This

model bears a resemblance to the micromechanically motivated Gurson-based models [49,57], whereby the volume fraction of the voids is taken as the main source of internal degradation. It is worth highlighting the advantage of this damage law over the Gurson-based models, as less material parameters are required to capture the material softening behaviour. This model also benefits of preserving a nonzero value of shear component for the plastic deformation tensor even under high triaxiality levels, a feature mainly attributed to the vertex of its yield surface. Using this framework, the material constitutive law is established by defining a potential that associates the macroscopic stresses and hydrostatic stress, hence, this model is classified under the family of pressure-dependent plasticity models. Following the thermodynamics of irreversible processes (TIP), the specific dissipated power is written based on a set of thermodynamical forces $\left\{\frac{\sigma}{\rho}, R, F\right\}$ conjugated to the internal variables $\{\varepsilon_p, \alpha, f\}$, such that:

$$\frac{\sigma}{\rho} : \dot{\varepsilon}_p - R\dot{\alpha} + F\dot{f} \geq 0 \quad (3.40)$$

where ρ is the relative density of the deformed material, R is the force conjugated to the internal variable α , i.e. the material hardening function, and F is the force associated with the damage variable f . By defining the specific free energy as:

$$\psi = \psi_e(\varepsilon_e) + \psi_p(\alpha) + \psi_d(f) \quad (3.41)$$

the conjugated forces are given by:

$$\frac{\sigma}{\rho} = -\frac{\partial \psi}{\partial \varepsilon_p} = \frac{\partial \psi}{\partial \varepsilon_e} \quad , \quad R = \frac{\partial \psi}{\partial \alpha} \quad , \quad F = \frac{\partial \psi}{\partial f} \quad (3.42)$$

where ψ_e , ψ_p and ψ_d are respectively the energies associated with the elastic, plastic and damage mechanisms. The plastic potential is determined based on the invariants of the stress tensor, σ_m and q and reads:

$$\phi = \phi_1\left(\frac{q}{\rho}, R\right) + \phi_2\left(\frac{\sigma_m}{\rho}, F\right) \quad (3.43)$$

with

$$\phi_1 = \frac{q}{\rho} - R \quad , \quad \phi_2 = Fg\left(\frac{\sigma_m}{\rho}\right) \quad (3.44)$$

Assuming the mass preservation law and incompressibility of the material matrix, the relative density is written as $\rho = \frac{1-f}{1-f_0}$, with f_0 being the initial void volume fraction attributed to the volume fraction of the inclusions. This function is indicative of the

density of the damaged material to its undamaged state that contains the inclusions. Rousselier showed that the function g takes the form, $g = D \exp\left(\frac{\sigma_m}{\rho\sigma_1}\right)$, and therefore, the common form of the plastic potential corresponds to this damage model is written by the following expression:

$$\phi = \frac{q}{\rho} - R(\alpha) + \sigma_1 f D \exp\left(\frac{\sigma_m}{\rho\sigma_1}\right) \quad (3.45)$$

Based on the normality rule, one can obtain the rate of the macroscopic plastic strain as:

$$\dot{\boldsymbol{\varepsilon}}^p = \dot{\lambda} \frac{\partial \phi}{\partial \left(\frac{\boldsymbol{\sigma}}{\rho}\right)} = \dot{\lambda} \left(\frac{3}{2} \frac{\mathbf{s}}{q} + \frac{1}{3} f D \exp\left(\frac{\sigma_m}{\rho\sigma_1}\right) \mathbf{I} \right) \quad (3.46)$$

in which it can be decomposed into the volumetric ($\dot{\varepsilon}_v^p$) and deviatoric ($\dot{\varepsilon}_d^p$) parts:

$$\dot{\varepsilon}_v^p = \dot{\lambda} \quad , \quad \dot{\varepsilon}_d^p = \frac{1}{3} \dot{\lambda} f D \exp\left(\frac{\sigma_m}{\rho\sigma_1}\right) \quad (3.47)$$

with $\dot{\lambda}$ as the plastic multiplier. The rate forms of the internal variables are given by:

$$\dot{\alpha} = -\dot{\lambda} \frac{\partial \phi}{\partial R} = \dot{\lambda} \quad , \quad \dot{f} = \dot{\lambda} D \exp\left(\frac{\sigma_m}{\rho\sigma_1}\right) \quad (3.48)$$

where σ_1 and D are the Rousselier model parameters that require to be calibrated relying on experimental observations. The former model parameter defines the material resistance to growth of the cavities and can be proportionately associated to the material flow stress.

In a similar manner to the Gurson-based models, the evolution of the void volume fraction due to growth of cavities in the original Rousselier model serves as the primary source of damage accumulation that is described through rate of the void volume fraction. Therefore, we have:

$$\dot{f} = (1 - f) \text{tr}(\dot{\boldsymbol{\varepsilon}}^p) = (1 - f) \dot{\varepsilon}_v^p \quad (3.49)$$

Due to the utilisation of an enhanced version of the model in the subsequent chapters, the numerical integration of the above constitutive framework is left to be discussed in chapter 4. As for the numerical aspects of Rousselier model and for comparison purposes, several aspects are highlighted as follows:

1. The role of the relative density should not be neglected in the present model, as $\frac{\sigma}{\rho}$ has been considered in derivation of the constitutive relations. This is linked to the

hypothesis of incompressibility and the fact that in the present ductile damage model the variation of density due the void growth is not negligible [23].

2. Differently than other modelling procedures put forward by some authors in which, as $f_0 \ll 1$, is assumed that $\rho = 1 - f$, in this study the initial porosity f_0 takes a nonzero value, as in the original Rousselier model. This scalar value is treated as a material parameter and in case of ($f_0 = 0$), no damage is generated and material model will be the same as the von Mises plasticity model.
3. The hardening function $R(\alpha)$ is determined via true stress-true plastic strain prior to the material softening regime. Henceforth, the internal variable α will be considered as the equivalent plastic strain, given by $\bar{\epsilon}_p = \sqrt{\frac{3}{2} \dot{\epsilon}_d^p : \dot{\epsilon}_d^p}$.
4. In the present work and following Eq. (3.49), the volume changes due to the growth of the voids is considered as the sole mechanism of the material deformation due to damage. However, several enhanced versions of the model based on addition of the nucleation and shear mechanisms through the modification of porosity rate were developed in literature, for instance in [20].
5. Apart from the material hardening determination which is typically carried out based on the laboratory test data, the phenomenological parameters of the Rousselier model are also required to be identified. Interestingly this process is easier as fewer model parameters than the GTN model need to be calibrated.
6. The vertex of the yield surface is considered as another important feature of the Rousselier damage model which makes it possible to utilise the model under wide range of triaxialities, i.e., even for tensile-dominant loading situations the plastic deformation tensor retains a non-zero shear component.
7. Despite the extension of the damage accumulation modelling by adding shear term to the evolution of porosity [20], under pure shear loading ($\sigma_m = 0$), the Rousselier model still generates damage growth as opposed to the Gurson-based models.

4 Gradient regularisation of ductile failure models

Numerical modelling of fracture has been one of the grand challenges in the engineering community throughout the decades. Some of the early computational predictive tools pursued the energetic Griffith theory in brittle fracture, at which a critical value of energy was introduced for creating a unit area of a crack interface. This discrete definition of discontinuities often requires an explicit tracking of the cracks which makes the numerical treatment cumbersome for more complex crack geometries. Several strategies were put forward by scientists to circumvent the difficulties of the discrete crack approaches, such as remeshing strategies [58,59] or extended finite element method [1], where the latter is based on the local enrichment of the finite element shape functions to deal with the displacement field jumps and stress singularity at the crack interfaces.

The computational load of these approaches, more specifically in dealing with complex crack geometries and 3D solids, gave rise to the smeared crack approaches, including the gradient and phase-field methods. The *nonlocal* and gradient regularisation of fracture was primarily originated from the continuous description of material degradation which has roots in continuous damage mechanics. The problem of ill-posed boundary value problem (the loss of ellipticity or hyperbolicity of differential equations in static and dynamic analyses) and spurious mesh sensitivity of the solution could lead to unrealistic and non-physical prediction of the fracture behaviour. These issues have been commonly reported in the *local* approaches to damage, such as the GTN or Lemaitre damage models which have been considered as two of the advanced material models in failure analysis of ductile metallic materials.

Stemming from the variational approaches to fracture, the phase-field diffusive method has been a topic of interest for the last two decades. This approach benefits from the ability to predict the initiation of cracks and analysing the crack development on a constant mesh without the need for any ad-hoc criteria, making this method a suitable choice for assessment of intricate crack patterns such as branching, merging or bifurcating topologies. The mathematical basis of the phase-field approach herein is in line with the

thermodynamically-consistent framework in [6] that is widely accepted in the fracture community and originally introduced in brittle solids.

In what follows, the gradient nonlocal methodology with the application in continuous damage mechanics is described and an efficient numerical strategy is discussed for finite element implementation of the coupled boundary value problem. Next, the primary ingredients of the phase-field mathematical framework in the brittle solids are revisited and the extension of the approach in the context of ductile fracture with the emphasis on micromechanical damage criterion is elucidated.

4.1 Nonlocal regularisation approaches

4.1.1 Mathematical background

The alleviation of the spurious mesh sensitivity through use of nonlocal regularisation was pioneeringly addressed by Pijaudier-Cabot et al. [60] in a practical sense, where a local field quantity, \mathcal{F} , may be spatially averaged over the problem domain Ω , with its nonlocal counterpart at point \mathbf{x} , using the following relation:

$$\bar{\mathcal{F}}(\mathbf{x}) = \int_{\Omega} \beta(\mathbf{x}, \zeta) \mathcal{F}(\zeta) d\Omega \quad (4.1)$$

with ζ as the position of an infinitesimal volume $d\Omega$ and $\beta(\mathbf{x}, \zeta)$ as the weighted averaging operator which should not modify the uniform field by satisfying the following normalizing condition

$$\int_{\Omega} \beta(\mathbf{x}, \zeta) d\Omega = 1 \quad (4.2)$$

The above operator often assumed to be homogenous and isotropic. The nonlocal field is considered as a weighted sum over the local values at all element integration points ζ within a nonlocal radius which characterises a domain of applicability or the so-called influence domain. Normalisation can be achieved by using the following typical weighting function:

$$\beta(\mathbf{x}, \zeta) = \frac{\beta_{\infty}(\mathcal{R})}{\int_{\Omega} \beta_{\infty}(\mathcal{R}) d\Omega(\zeta)} \quad (4.3)$$

where $\mathcal{R} = \|\mathbf{x} - \boldsymbol{\zeta}\|$ is the distance between \mathbf{x} and $\boldsymbol{\zeta}$, and where in $\beta_\infty(\mathcal{R})$ is often employed a non-negative, bell-shaped function. Interested readers are referred to [61] for an in-depth study of this methodology which is out of the scope of the present work.

The above conventional integral-type nonlocal kernels has always been followed by several issues such as the difficulty to achieve the quadratic convergence rates arises from inconsistent tangent operators as addressed in [63].

The gradient-type localisation limiters proposed pioneeringly in [62] via expanding the local field presented in Eq. (4.1) into a Taylor series, such that:

$$\begin{aligned} \mathcal{F}(\boldsymbol{\zeta}) = & \mathcal{F}(\mathbf{x}) + \frac{\partial \mathcal{F}}{\partial \mathbf{x}_i} (\zeta_i - \mathbf{x}_i) + \frac{1}{2!} \frac{\partial^2 \mathcal{F}}{\partial \mathbf{x}_i \partial \mathbf{x}_j} (\zeta_i - \mathbf{x}_i) (\zeta_j - \mathbf{x}_j) \\ & + \frac{1}{3!} \frac{\partial^3 \mathcal{F}}{\partial \mathbf{x}_i \partial \mathbf{x}_j \partial \mathbf{x}_k} (\zeta_i - \mathbf{x}_i) (\zeta_j - \mathbf{x}_j) (\zeta_k - \mathbf{x}_k) + \dots \end{aligned} \quad (4.4)$$

Substituting the above relation into (4.1) and truncating the fourth and higher order terms yields the following explicit relation:

$$\bar{\mathcal{F}} = \mathcal{F} + l_N \nabla^2 \mathcal{F} \quad (4.5)$$

With this definition, a length scale parameter l_N is introduced, which can be linked to the spatial interactions and the microstructure of the material. Thus, this parameter is often referred to as the material intrinsic length scale and numerically it is treated as a material parameter. The above relation can be further enhanced by differentiating it twice, yielding the following Helmholtz type PDE:

$$\bar{\mathcal{F}} - l_N \nabla^2 \bar{\mathcal{F}} = \mathcal{F} \quad (4.6)$$

with the corresponding boundary condition:

$$\nabla \bar{\mathcal{F}} \cdot \mathbf{N} = \mathbf{0} \quad (4.7)$$

Clearly, Eq. (4.6) gives a more practical representation as different from Eq. (4.5), the nonlocal field is related to the local field in an implicit manner. This can be explained by considering the strain field as the local quantity, at which its second gradient implies a third order derivative of the displacement field. The nonlocal formulation described by Eq. (4.6) is often considered to has a *truly* nonlocal nature and it has the flexibility to be introduced based on different local fields, including internal material degradation quantities such as plastic strain or damage variable. Following the context of the present

study, this gradient treatment has been successfully applied to the ductile damage frameworks, for instance in [64–66].

In the next section, the above nonlocal treatment is applied to the continuous damage description based on the Lemaitre ductile damage criterion and a novel strategy following the similarity of the equation with the heat conduction equation is introduced for implementation of the coupled problem within the finite element framework.

4.1.2 Nonlocal gradient regularisation of ductile damage

By recalling the material framework of Lemaitre’s ductile damage model and its numerical integration addressed in chapter 3, the nonlocal implicit gradient methodology can be utilised as a localisation limiter by choosing the damage field as the local quantity in this context.

As a point of departure, the following set of governing equations establishes the coupled multi-field boundary value problem over the problem domain Ω , consisting of the stress equilibrium and gradient equations that are given by:

$$\begin{cases} \operatorname{div} \boldsymbol{\sigma} + \rho \mathbf{b} = \mathbf{0} \\ \bar{\mathcal{D}} - l_N^2 \nabla^2 \bar{\mathcal{D}} = \mathcal{D} \end{cases} \text{ in } \Omega \quad (4.8)$$

with the boundary conditions:

$$\begin{cases} \boldsymbol{\sigma} \cdot \mathbf{N} = \mathbf{t} & \text{on } \partial\Omega_t \\ \mathbf{u} = \bar{\mathbf{u}} & \text{on } \partial\Omega_u \\ \nabla \bar{\mathcal{D}} \cdot \mathbf{N} = \mathbf{0} & \text{on } \partial\Omega \end{cases} \quad (4.9)$$

The first two conditions are applied to the stress equilibrium equation imposing the Neumann and Dirichlet boundary limits respectively on $\partial\Omega_t$ and $\partial\Omega_u$, where $\bar{\mathbf{t}}$ is the external boundary traction forces. The third condition is a Neumann type boundary condition linked to the gradient implicit equation. The influence of the nonlocal field thus can be considered in the model by modifying the constitutive material model framework accordingly, gives the following set of relations:

$$\varphi = \frac{q}{1 - \bar{\mathcal{D}}} - R(\alpha) = 0 \quad (4.10)$$

$$\boldsymbol{\sigma} = (1 - \bar{\mathcal{D}}) \mathbf{D}^e : \boldsymbol{\varepsilon}^e \quad (4.11)$$

$$Y = \frac{1}{(1 - \bar{\mathcal{D}})^2} \left(\frac{-q^2}{6G} - \frac{p^2}{2K} \right) \quad (4.12)$$

$$\dot{\mathcal{D}} = \frac{r_1}{(1 - \overline{\mathcal{D}})(1 + r_2)} \left(-\frac{Y}{r_1} \right)^{r_2+1} \quad (4.13)$$

$$\dot{\boldsymbol{\varepsilon}}^p = \dot{\gamma} \mathbf{N} \quad \text{with } \mathbf{N} = \sqrt{\frac{3}{2}} \frac{\mathbf{s}}{(1 - \overline{\mathcal{D}})^2 \|\mathbf{s}\|} \quad (4.14)$$

The numerical integration of the above system of equations is followed by the one-equation return mapping procedure that described in section 3.2.1 with minor differences coming from the replacement of the local damage field by its nonlocal counterpart in the relations, which will be skipped in this text.

4.1.3 A simple and unified solution strategy for the coupled problem

This section addresses a simplified methodology for solving the diffusive equation of gradient-enhanced nonlocal damage model in regards with its numerical implementation. This strategy which has also been recently used in [39], takes the advantage of built-in heat equation solver in commercial software ABAQUS, which offers an ability to bypass the need to mathematically establish the weak form of the governing equations containing the momentum balance and the diffusive equation and in the context of commercial software in use, it gives the possibility to utilise the user material code (UMAT) for coding the underlying constitutive material model. This is particularly efficient in computational terms compared to software procedures defined in the element level (UEL), where forces and tangent matrices are required to be determined precisely.

The attention is drawn to the transient heat equation problem that describes the local heat flux, Q , by the following relation:

$$\mathcal{D}c_p \partial_t T - K \nabla T = \dot{Q} \quad (4.15)$$

where $\partial_t T$ is the time derivative the temperature field T and ∇T is the gradient of the temperature field. This can be rewritten, for the steady-state case, giving the following boundary value problem:

$$\begin{cases} K \nabla T + h_s = 0 & \text{in } \Omega \\ Q \cdot \mathbf{N} = \mathcal{D} & \text{on } \partial\Omega \end{cases} \quad (4.16)$$

where h_s is a heat source term, and Neumann type boundary condition for the heat flux are applied and based on a heat source term, h_s , on the boundary $\partial\Omega$.

By observing the similarity of the above gradient equation with the nonlocal equation in PDE of Eq. (4.6), the above heat conduction problem and its built-in software capability can be suitably used for the implementation of the nonlocal gradient approach. Thus, the conductivity value and temperature are respectively served as the root squared of the intrinsic length parameter l_N , and the nonlocal damage field $\bar{\mathcal{D}}$. The heat source is simply taken as $h_s = \bar{\mathcal{D}} - \mathcal{D}$, which can be introduced into the coupled temperature-displacement subroutine HETVAL in ABAQUS software. This user routine can be processed along the UMAT routine, in which the local damage field is transferred through the common block. At each load increment, the calculated value of the nonlocal field (temperature in HETVAL) which is commonly smaller value than its local counterpart, is retrieved in the UMAT module and the calculations of the stresses and consistent tangent operator are carried out based on that value.

4.2 Phase-field modelling of fracture in brittle solids

The problem of the crack analysis has been exposed to a great number of theoretical and computational investigations since the advent of the phase-field approach in fracture. Coming from variational backgrounds in the late 90s, the phase-field diffusive methodology has been well received by the engineering community in a variety of applications. Compared to the classical theories within the framework of discrete crack approaches, phase-field crack concept carries the advantage of analysing discontinuities without the need to explicitly or implicitly track the propagating cracks, whereby it has the ability of predicting the evolution of a crack on a fixed finite element mesh. This feature competitively reduces the excessive computational costs linked to the utilisation of remeshing strategies or methods based on enriched shape functions such as XFEM, which is more significant in 3D problems, involving complex crack geometries, both in brittle and ductile fracture of solids.

Since its development on the basis of the variational approach to fracture proposed by Frankfort and Marigo [67], phase-field fracture concept has been utilised in the quasi-static and dynamic problems, with the application in brittle or ductile fracture. Though departing from the different mathematical basis, this formulation bears a resemblance to the gradient nonlocal concept discussed in section 4.1, due to the gradient format of the evolution equation, as addressed in comparative studies in [36,37].

The thermodynamically-consistent framework put forward by Miehe et al. in [68] is known as one of the early firm studies in this line of research, in theoretical and computational terms. In that work, in a pioneering move, the authors proposed a history field parameter based on a maximum positive reference energy to naturally impose the irreversible evolution of the crack discontinuity. This feature also provides an important basis to the implementation of the multi-field boundary value problem by an algorithm based on a staggered solution scheme, which evaluates displacement and phase-field in an alternate and uncoupled fashion.

The mathematical background of the present work falls under this line of research, where we start by revisiting the phase-field diffusion approach in brittle solids conforming to the formulation in [69] and, subsequently, the extended model framework with application to the ductile fracture concept is discussed with focusing on micromechanical damage criteria. Throughout the study, we confine ourselves to quasi-static problems and the mathematical notations are close to the adopted in the cited reference.

4.2.1 Regularisation of the sharp crack topology

Starting from a 1D setting, an infinite bar with problem domain $\Omega = \Gamma \times L$ is considered, where Γ and $L \in [-\infty, +\infty]$ are respectively the cross section and length of the bar as depicted in Figure 1.1(a). A sharp crack at $x = 0$ is treated in a diffusive manner by an auxiliary, scalar field variable or the so-called *crack phase-field* as:

$$d: \begin{cases} \Omega \times \tau \rightarrow [0,1] \\ (\mathbf{x}, t) \rightarrow d(\mathbf{x}, t) \end{cases} \quad (4.17)$$

that distinguishes between the intact ($d = 0$) and cracked ($d = 1$) material states. In one dimensional problem, this parameter can be expressed by the following exponential function:

$$d(x) = e^{-|x|/l_d} \quad (4.18)$$

The order parameter defined by Eq. (4.18) is governed by a length parameter, l_d , that defines the width of the crack diffusion area, and follows the properties $d(0) = 1$ and $d(\pm\infty) = 0$. The above expression is the solution of the following homogenous differential equation:

$$d(x) - l_d^2 d''(x) = 0 \quad (4.19)$$

Notice that the sharp crack description of Griffith theory may be recovered in the limit of $l_d \rightarrow 0$.

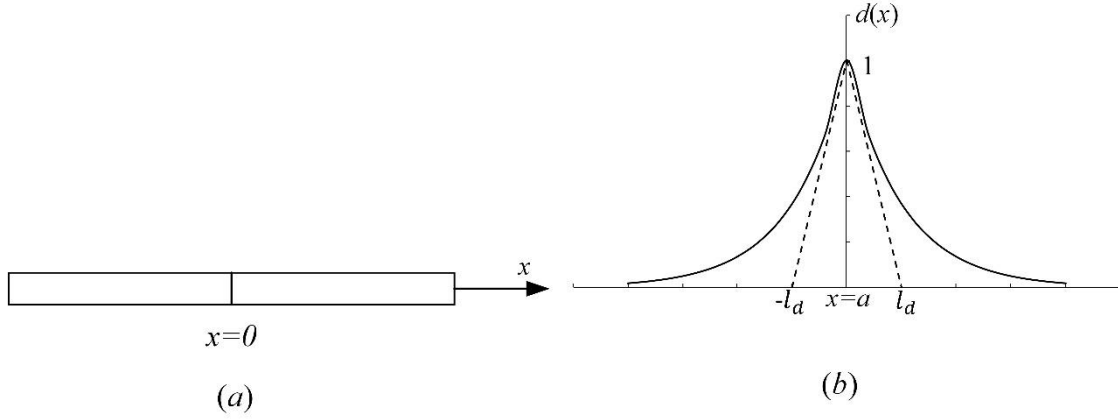


Figure 4.1 a) One-dimensional bar with a crack at $x = 0$, b) variation of the phase-field with the length scale

The solution of the strong form of Eq. (4.19) can also be obtained by the variational principle associated to:

$$d = \text{Arg} \left\{ \inf_{d \in w} I(d) \right\} \quad (4.20)$$

with $w = \{d | d(0) = 1, d(\pm\infty) = 0\}$ and the functional I defined as:

$$I(d) = \frac{1}{2} \int_{\Omega} (d^2 + l_d^2 d'^2) dV \quad (4.21)$$

By integrating over the volume $dV = \Gamma dx$ and for $d = e^{-|x|/l_d}$, one can obtain $I = l_d \Gamma$. The above relation expressed in the structure of the functional as introduced in [69] as follows:

$$\Gamma_{l_d} = \frac{1}{l_d} I(d) = \frac{1}{l_d} \left(\frac{1}{2} \int_{\Omega} (d^2 + l_d^2 d'^2) dV \right) = \int_{\Omega} \gamma(d, d') dV \quad (4.22)$$

where the function $\gamma(d, d')$ serves as the primary relation in constitution of the crack diffusion framework in this context. In a rather straightforward manner, the above expression can be generalised to higher-dimensional problems, where $\Omega \subset \mathcal{R}^D$ is the

domain of the multi-dimensional body with $\mathcal{D} \in [1,2,3]$, $\partial\Omega \subset R^{\mathcal{D}-1}$ defines the boundary of the body, consisting of the union $\partial\Omega_t$ and $\partial\Omega_u$, where tractions and displacement are prescribed, respectively, and the existing sharp crack discontinuity in the reference configuration, $\Gamma(t) \subset R^{\mathcal{D}-1}$, as depicted in Figure 1.2(a).

Regularisation of the crack geometry is performed using the following *crack density functional* per unit volume:

$$\gamma(d, \nabla d) = \frac{1}{2l_d} d^2 + \frac{l_d}{2} |\nabla d|^2 \quad (4.23)$$

being ∇d the spatial gradient of the phase-field order parameter. Accordingly, the regularised phase-field crack can be represented by:

$$d(x, t) = \text{Arg} \left\{ \inf_{d \in W_{\Gamma(t)}} \Gamma_{l_d} \right\} \quad (4.24)$$

that follows the Dirichlet boundary condition of $W_{\Gamma(t)} = \{d | d(x, t) = 1 \text{ at } x \in \Gamma(t)\}$. Likewise the one-dimensional case, the Euler equation of the variational form in Eq. (4.24) is expressed as:

$$d - l_d^2 \Delta d = 0 \text{ in } \Omega \quad \text{s.t.} \quad \nabla d \cdot \mathbf{N} = 0 \text{ on } \partial\Omega \quad (4.25)$$

where \mathbf{N} is the unit outward vector normal to the surface boundary $\partial\Omega$ and Δd represents the Laplacian of the phase field variable that should satisfy the above Neumann boundary condition. Figure 1.2 illustratively shows the diffusion of crack $\Gamma(t) \subset R^{\mathcal{D}-1}$ evolving irreversibly through time t .

4.2.2 Constitutive relations in a fractured solid

The above diffusion concept is used as a basis to develop the coupled phase-field deformation problem. The total energy dissipated in a cracked brittle solid can be described as a competition between the stored elastic energy Ψ^e and the surface (fracture) energy Ψ^f , and reads:

$$E(\mathbf{u}, d) = \Psi^e + \Psi^f = \int_{\Omega} \psi_e(\varepsilon(\mathbf{u}), d) dV + \int_{\Gamma} \mathcal{G}_c \gamma(d, \nabla d) dV \quad (4.26)$$

where ψ_e is the elastic strain energy written as:

$$\psi_e = g(d)\psi_0 = \frac{g(d)}{2} [\boldsymbol{\varepsilon}^e : \boldsymbol{\sigma}_{y0}] \quad (4.27)$$

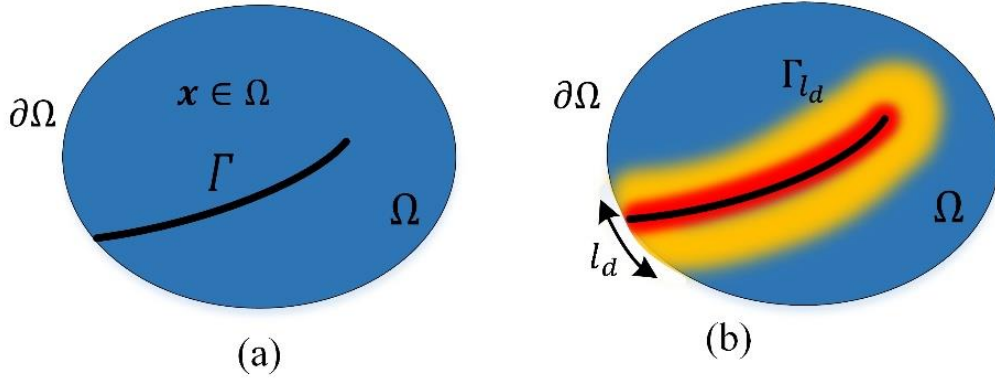


Figure 4.2 a) Sharp crack versus b) diffused crack topology using phase-field regularisation method; width of the diffused region is characterized by l_d

being ψ_0 is the reference elastic energy, $\boldsymbol{\sigma}_{y0} = \mathbf{D}^e : \boldsymbol{\varepsilon}^e$ the reference elastic stress tensor, \mathcal{G}_c the Griffith-based critical value of the energy released from the formation of crack interfaces and $g(d)$ the phase-field degradation function that is commonly expressed by the following quadratic form:

$$g(d) = (1 - d)^2 + \kappa \quad (4.28)$$

being $\kappa \ll 1$ a small dimensionless parameter to avoid difficulties in numerical implementation. The above expression assures monotonic decreasing of the stress-carrying capacity of the material and has the properties $g(0) = 1$, $g(1) = 0$ and $g'(1) = 0$, in which the first two conditions describe the limits for the undamaged and damaged material states respectively and the third property guarantees that a finite value of bulk energy for a fully damage state at $d = 1$ may be achieved. To impose the irreversibility

of the crack evolution ($\dot{d} \geq 0$), Miehe et al. [69] proposed a history field that is specified based on the maximum reference energy value¹ as:

$$\mathcal{H} = \max_{\tau \in [0, t]} \psi_0(\mathbf{x}, \tau) \quad (4.29)$$

In a similar manner to the gradient approach discussed in the previous section, the global problem of fracture is described based on the crack field of Eq. (4.17) and the displacement field:

$$\mathbf{u}: \begin{cases} \Omega \times \tau \rightarrow \mathcal{R}^D \\ (\mathbf{x}, t) \rightarrow \mathbf{u}(\mathbf{x}, t) \end{cases} \quad (4.30)$$

Therefore, the problem solution is essentially addressed with the following boundary value problem that is obtained by taking the variation of the bulk and fracture energies expressed in Eq. (4.26), such that $\delta\Psi^e = 0$ and $\delta\Psi^f = 0$, consisting of the bounded stress equilibrium equation:

$$\begin{cases} \nabla \cdot \boldsymbol{\sigma} = \mathbf{0} & \text{on } \Omega \\ \boldsymbol{\sigma} \cdot \mathbf{n} = \mathbf{t} & \text{on } \partial\Omega_t \\ \mathbf{u} = \bar{\mathbf{u}} & \text{on } \partial\Omega_u \end{cases} \quad (4.31)$$

and the phase-field evolution equation:

$$\begin{cases} \frac{\mathcal{G}_c}{l_d} (d - l_d^2 \Delta d) = 2(1 - d)\mathcal{H} & \text{on } \Omega \\ \nabla d \cdot \mathbf{N} = 0 & \text{on } \partial\Omega \end{cases} \quad (4.32)$$

where $\boldsymbol{\sigma}$ is the Cauchy stress and defined as:

$$\boldsymbol{\sigma} = [(1 - d)^2 + \kappa] \boldsymbol{\sigma}_0 \quad (4.33)$$

4.2.3 Weak form of the boundary value problem

The above initial boundary value problem described in Eqs. (4.31) and (4.32) are adopted as the basis for the following numerical analysis of fracture. Starting from the calculation

¹ In the work of Miehe et al. [68] and based on degradation under tension only (positive reference energy) $\psi_e = g(d)\psi_0^+ + \psi_0^-$, the history field is assigned to the maximum positive reference energy written as $\mathcal{H} = \max_{\tau \in [0, t]} \psi_0^+(\mathbf{x}, \tau)$.

of the weak forms of the mechanical and the phase-field equations, the test functions, $\delta \mathbf{u}$ and δd , respectively for displacement and phase-field are defined. By multiplying the test functions with Eqs. (4.31)₁ and (4.32)₁ and integration over the problem domain, one can obtain:

$$\begin{cases} \int_{\Omega} \boldsymbol{\sigma} : \nabla \delta \mathbf{u} dV = 0 \\ \int_{\Omega} \left(\left(\frac{\mathcal{G}_c}{l_d} + 2\mathcal{H} \right) d - \mathcal{G}_c l_d \Delta d - 2\mathcal{H} \right) \delta d dV = 0 \end{cases} \quad (4.34)$$

Performing the integration by parts on the phase-field equation, after some algebraic calculus, gives:

$$\int_{\Omega} 2\mathcal{H}(d-1)\delta d dV + \int_{\Omega} \mathcal{G}_c \left(\frac{d}{l_d} + l_d \nabla d \cdot \nabla \delta d - l_d \nabla(\delta d \nabla d) \right) dV = 0 \quad (4.35)$$

Neglecting the second order gradient terms on the second equation, the final weak form of the problem is given by:

$$\begin{cases} \int_{\Omega} \boldsymbol{\sigma} : \nabla \delta \mathbf{u} dV = 0 \\ \int_{\Omega} 2\mathcal{H}(d-1)\delta d dV + \int_{\Omega} \mathcal{G}_c \left(\frac{d}{l_d} + l_d \nabla d \cdot \nabla \delta d \right) dV = 0 \end{cases} \quad (4.36)$$

The above system of equations can be comfortably implemented within the finite element framework as is described in what follows.

4.2.4 Finite element implementation using a staggered solution strategy

Following the staggered integration procedure that was grounded by Miehe et al. in [69], the solution of the multi-field boundary value problem described in Eqs. (4.31) and (4.32) can be obtained based on alternate calculation of the crack and displacement fields, i.e. solving the displacement field for the frozen value of the crack field and vice versa. The commercial software ABAQUS package offers several modules that can be utilised for user coding in this context, as used by different authors in [9–11,70], among others. For this purpose, the weak form of the phase-field evolution equation expressed in Eq. (4.36)₂ is discretised by using the standard finite element shape functions N_i associated with node number i , written as:

$$d = \sum_{i=1}^{nnode} N_i d_i \quad (4.37)$$

with $nnode$ as the total number of the nodes per element. Accordingly, the derivatives and the gradients in 2D problem correspond to the phase-field are given by:

$$B_i^d = \begin{bmatrix} N_{i,x} \\ N_{i,y} \end{bmatrix} \quad (4.38)$$

$$\nabla d = \sum_{i=1}^{nnode} B_i^d d_i ; \quad \nabla \delta d = \sum_{i=1}^{nnode} B_i^d \delta d_i$$

By substituting the Eqs. (4.37) and (4.38) into Eq. (4.36)₂, one can obtain $R^d = 0$ with R^d as phase-field residual force given by:

$$R_i^d = \int_{\Omega} -2(d-1)N_i \mathcal{H} dV - \int_{\Omega} \mathcal{G}_c \left(\frac{1}{l_d} N_i d + l_d [B_i^d]^T [B_i^d] \right) dV = 0 \quad (4.39)$$

Given the time interval $\Delta t = [t_n, t_{n+1}]$, the solution is obtained by having the known value of the state variables at the beginning of the time increment t_n and updating their values at the end of the time increment t_{n+1} . The phase-field nodal values may be determined by solution of the following linear relation:

$$d_{i\,n+1} = d_{i\,n} - [K^d]_i^{-1} [f^d]_i \quad (4.40)$$

with the corresponding phase-field tangent expressed by:

$$[K^d]_i = \frac{\partial R_i^d}{\partial d} = \int_{\Omega} \mathcal{G}_c l_d [B_i^d]^T [B_i^d] dV + \int_{\Omega} \left(2\mathcal{H} + \frac{\mathcal{G}_c}{l_d} \right) N_i^T N_i dV \quad (4.41)$$

where

$$[f^d]_i = \int_{\Omega} 2\mathcal{H} N_i d\Omega \quad (4.42)$$

The numerical implementation of the above phase-field problem in ABAQUS through the use of a multi-layer user element module (UEL) is addressed in brittle solids [9] and elastoplastic solids [70]. In this work, the above definitions are introduced into the UEL routine and a direct sparse equation solver from the Intel Math Kernel Library (MKL) is embedded to solve the Eq. (4.40) for the phase-field nodal values. Once calculated, the

phase-field is interpolated to the integration points using Eq. (4.37) and is stored in a common block.

The stress equilibrium equation in Eq. (4.31) is treated in a parallel way via a user material routine (UMAT), whereby the phase-field values are retrieved to influence the stress update procedure following the Eq. (4.33). The history field of Eq. (4.29) is determined at the material point level using the elastic stress and strains and is stored through the common block to be utilised in the phase-field equation solver. This method, unlike the monotonic implementations for instance in [10], simplifies the user coding and bypasses the need to calculate the displacement tangents and cross term tangents in the UEL module. Moreover, it provides a basis for parallel utilisation of the sophisticated material models through the coding in the user material (UMAT) routine, which can be efficiently employed in the following sections.

4.3 Phase-field diffusion model in ductile fracture

4.3.1 General description

The diffusive phase-field models in ductile fracture emerged in the last few years, following the fact that mere representation of the crack with phase-field order parameter is not a sufficient modelling framework in most metallic materials, in which an extensive level of plastic deformation occurs prior to the meso-crack formation. Based on the type of coupling between the plasticity material model and the fracture energy, several different formulations were developed, to name a few, in [13,71–73]. The model of Borden et al. [72] is one of the most common adopted models, in which the influence of the plastic dissipation is embedded in the energy description in Eq. (4.26). This requires to consider the plastic strain effects in the definition of the bulk energy, i.e. replacing the elastic energy in Eq. (4.27) with the following relation that is expressed based on the plastic strains:

$$\psi_e = \frac{g(d)}{2} [(\boldsymbol{\varepsilon} - \boldsymbol{\varepsilon}^p) : \boldsymbol{\sigma}_{y0}] \quad (4.43)$$

The phase-field parameter in [72] is characterised by the micro-force balance law and the measure of the stress triaxiality is employed in the plastic work expression which is served as a driving force for initiation and propagation of the cracks.

In [13], authors followed a purely geometric approach to generalise the phase-field energetic concept towards the stress-based criteria, at which the influence of the inelastic deformation could be considered through the use of an alternative crack driving force. Using this approach, the influence of the bulk response in multi-physics problems can be expressed by the following constitutive relation for the evolution of the crack field:

$$\frac{d}{dt}\Gamma_{l_d} = \frac{1}{l_d} \int_{\Omega} (1-d)\mathcal{H} - \bar{\mathcal{R}}) \dot{d} dV \quad (4.44)$$

where $\bar{\mathcal{R}}$ is the local viscous crack resistance that can be directly related to the rate of the phase-field crack. This approach provides a basis for the phase-field problem to be coupled with various constitutive models, which has been addressed recently in the context of von Mises plasticity [38] and GTN damage model [15]. In the following section, the extension of the described phase-field approach to ductile fracture pursues this line of research which is directed towards a micromechanical damage criterion.

4.3.2 Extended formulation to the micromechanical damage framework

In this study, the generalisation of the phase-field approach to the ductile fracture concept is performed in a novel fashion using the micromechanical damage concept based on the Rousselier criterion. A crack initiation criterion thus needs to be defined, which distinguishes between the material deformation before and after a threshold value characterised on the basis of a critical value of porosity. The coupled problem is determined at the material level by utilising the phase-field degradation function within the constitutive relations, including the stress update and the consistent tangent operator.

Recalling the phase-field evolution equation expressed in Eq. (4.32), an alternative form of the crack driving force could be defined to establish a link between the phase-field crack problem and the inelastic damage law in use. Accordingly, a new crack driving

force is introduced based on the maximum value of a crack state function, S , which appears in the following expression:

$$\begin{cases} f \geq f_c & \mathcal{H} = \max_{\tau \in [0, t]} S(\mathbf{x}, \tau) \\ else & \mathcal{H} = 0 \end{cases} \quad (4.45)$$

being f_c the critical value of the void volume fraction which is considered as a threshold value at which void coalescence and material accelerated softening occurs thereafter. The state function can be defined, within a purely ductile context, based on the evolution of the state variables of the local constitutive model processed at each material point \mathbf{x} . The above crack driving force postulates the irreversibility of the crack phase-field $\dot{d} \geq 0$ and it gives us the possibility to link the diffusive crack concept to a wide range of constitutive frameworks, including the continuous damage models. In accordance to the pressure-dependent damage law of the present contribution, the state function may be defined based on the description of the damage dissipation, written as:

$$S = \eta \sigma_1 f D \exp\left(\frac{\sigma_h}{\rho \sigma_1}\right) \quad (4.46)$$

in which the phase-field crack starts to evolve based on the accumulation of damage after the criterion of Eq. (4.45) is met. In the above relation, η is a dimensionless numerical parameter to control the post-critical material softening and will be referred to as *fracture coefficient* henceforth.

Therefore, such critical state is being used herein as the onset of crack propagation, induced by the phase-field model, so that the material failure after this point is no longer characterised by the sole role of void volume fraction. The loss of material load-carrying capacity is, thus, influenced by the additional induced degradation given by the phase-field crack model, which could lead to an accelerated material degradation in the post-critical range. This can be, in another perspective, viewed as an alternative approach to model the void coalescence, which was addressed using different explicit criteria in literature such as Thomason coalescence criterion [35], as was investigated for instance in [34] in the context of Rousselier model. In theoretical terms, such representation can avoid the *conflicting role* of the damage fields, volume void fraction and the phase-field crack, by obeying to the specified crack initiation criterion.

4.3.3 Numerical implementation of the coupled multi-field problem

The solution of the coupled problem defined above is obtained through the global staggered integration (discussed in section 4.2.4) of the multi-field boundary value problem described in Eqs. (4.31) and (4.32), and the local integration of the constitutive micromechanical material framework. The latter solution is obtained via an implicit integration algorithm adopted for the class of pressure-dependent plasticity models in [74]. This procedure is defined in the UMAT interface in ABAQUS which gives the updated state variables and the crack driving force on a material point level at each load increment. This routine is processed in parallel with a direct sparse solver defined in an element level (UEL) to obtain the phase-field crack development as already clarified before, with the exception that the alternative form of the crack driving force in Eq. (4.45) is calculated in the material routine and transferred to the UEL interface through the `common` block. This procedure is schematically described in Figure 4.3.

In what follows, first the constitutive material description relevant to the class of pressure-dependent plasticity models including the Rousselier damage criterion is discussed. Then the integration procedure of the phase-field diffused damage model is explained, which is based on the local constitutive description integration of the damaged material using backward Euler method addressed in [74]. As for the numerical model implementation in the UMAT code, the determination of the tangent moduli consistent with the stress return algorithm is inevitable. In this regard, the explicit tangent formulation by Zhang [75] is utilised.

Elastoplastic constitutive framework

The constitutive material description in this section follows the thermodynamic principles and is formulated based on the internal variable approach, similar to the model described for the continuous damage criterion discussed in section 3.2.1. The additive decomposition of the strain tensor into the elastic ($d\boldsymbol{\varepsilon}^e$) and plastic ($d\boldsymbol{\varepsilon}^p$) components is written as:

$$d\boldsymbol{\varepsilon} = d\boldsymbol{\varepsilon}^e + d\boldsymbol{\varepsilon}^p \quad (4.47)$$

By considering infinitesimal deformations, the Cauchy stress tensor is obtained based on the elastic strain energy (ψ_e), given by:

$$\boldsymbol{\sigma} = \frac{\partial \psi_e}{\partial \boldsymbol{\varepsilon}^e} = \mathbf{D}^e : \boldsymbol{\varepsilon}^e \quad (4.48)$$

The plastic admissibility of the material is verified by the yield function φ :

$$\varphi(p, q, H^i) = 0 \quad (4.49)$$

at which for $\varphi \leq 0$ the material is in the elastic regime and for $\varphi > 0$ the material experiences the plastic deformations. The above yield function is represented in terms of the stress invariants and the set of the internal variables H^i , $i = 1, 2, \dots$, and within the context of the current damage model framework, the plastic hardening-related variable and the void volume fraction are considered as these variables. Bearing in mind that the constitutive model derivation herein is based on the internal variable approach, the rate of the plastic strain and the internal variables are given by:

$$d\boldsymbol{\varepsilon}^p = d\lambda \frac{\partial \Phi}{\partial \boldsymbol{\sigma}} \quad (4.50)$$

$$d\mathbf{H} = h(d\boldsymbol{\varepsilon}^p, \boldsymbol{\sigma}, \mathbf{H}) \quad (4.51)$$

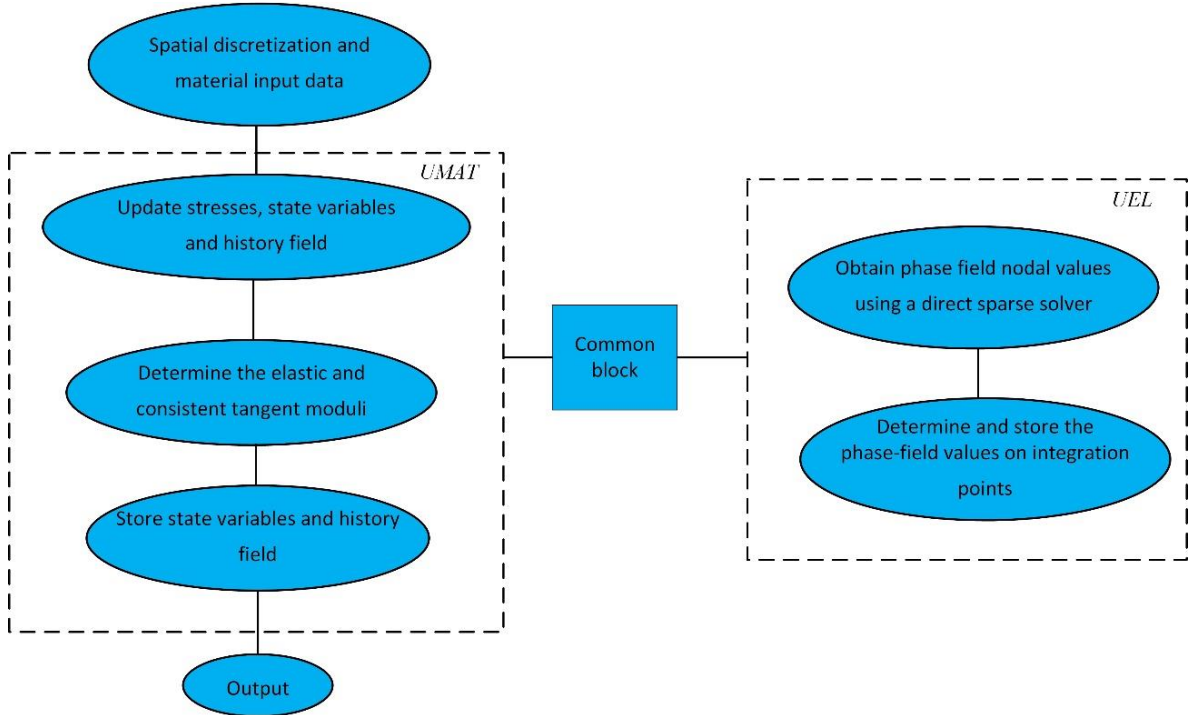


Figure 4.3 a) Schematic representation of the staggered solution procedure using Abaqus/Standard routines

where Φ is the plastic potential, $d\lambda$ is a positive scalar representing the plastic multiplier and \mathbf{H} is the set of internal variables. The rate of the plastic strain in Eq. (4.50) can be rewritten based on the contributions of the stress tensor as:

$$d\boldsymbol{\varepsilon}^p = d\lambda \left(-\frac{1}{3} \frac{\partial \Phi}{\partial p} \mathbf{I} + \frac{\partial \Phi}{\partial q} \mathbf{N} \right) \quad (4.52)$$

where \mathbf{N} is the unit vector normal to the yield surface. Alternatively, the above rate can be decomposed to the volumetric ($d\boldsymbol{\varepsilon}_v^p$) and deviatoric ($d\boldsymbol{\varepsilon}_d^p$) components, such that:

$$d\boldsymbol{\varepsilon}^p = d\boldsymbol{\varepsilon}_v^p + d\boldsymbol{\varepsilon}_d^p \quad (4.53)$$

where

$$d\boldsymbol{\varepsilon}_v^p = -\frac{d\lambda}{3} \frac{\partial \Phi}{\partial p} \mathbf{I} \quad (4.54)$$

$$d\boldsymbol{\varepsilon}_d^p = d\lambda \frac{\partial \Phi}{\partial q} \mathbf{N} \quad (4.55)$$

The set of expressions given in Eqs. (4.47), (4.48), (4.49), (4.50) and (4.51) are the core ingredients of the constitutive description that is expressible for the class of pressure dependent plasticity models including the Rousselier damage model herein. The above constitutive model is summarised in Box 4.1.

4.3.4 Integration algorithm of the phase-field diffused pressure-dependent plasticity model

The detailed integration of the above model coupled with the phase-field diffusive model is discussed in this section, which is based on the radial return algorithm addressed for the family of pressure-dependent plasticity models in [74] and under the premise of infinitesimal deformations. The influence of the phase-field degradation function is included in the expressions for the stress update and the plastic consistent tangent operator accordingly.

Within the framework of finite element method, the solution is achieved by updating the state variables at the integration points. By recalling the temporal discretisation described in integration algorithm in section 3.2.1, a pseudo time increment $\Delta t = t_{n+1} - t_n$ is

considered and the problem is to update the set of stresses and state variables at the beginning of the increment $(\boldsymbol{\sigma}_n, \boldsymbol{\varepsilon}_n, H_n)$ to their corresponding values at the end of the increment $(\boldsymbol{\sigma}_{n+1}, \boldsymbol{\varepsilon}_{n+1}, H_{n+1})$. By simplifying the notation, the subscripts of the variables at the beginning of the increment are omitted henceforth, unless otherwise stated. Given the strain increment $(\Delta\boldsymbol{\varepsilon})$ and elastic strain tensor $(\boldsymbol{\varepsilon}_{n+1}^e)$, the elastic constitutive relation is given by:

$$\boldsymbol{\sigma}_{n+1} = g_d \mathbf{D}^e : \boldsymbol{\varepsilon}_{n+1}^e = \boldsymbol{\sigma}_{n+1}^{tr} - g_d \mathbf{D}^e : \Delta\boldsymbol{\varepsilon}^p \quad (4.56)$$

where $\boldsymbol{\sigma}_{n+1}^{tr} = g_d \mathbf{D}^e : (\boldsymbol{\varepsilon}^e + \Delta\boldsymbol{\varepsilon})$ is the degraded elastic stress tensor which is linked to the elastic predictor step in the algorithm. Notice the diffusive field degradation function, g_d , is computed based on the information of the phase-field from the last converged increment that is retrieved from the UEL routine. The plastic admissibility limit is recalled from Eq. (4.49):

$$\Phi(p_{n+1}, q_{n+1}, H_{n+1}^i) = 0 \quad (4.57)$$

The increment of plastic strain in Eq. (4.50) may be rewritten in the following form:

$$\Delta\boldsymbol{\varepsilon}^p = \frac{1}{3} \Delta\epsilon_p \mathbf{I} + \Delta\epsilon_q \mathbf{N}_{n+1} \quad (4.58)$$

where

$$\Delta\epsilon_p = -\Delta\lambda \left(\frac{\partial\Phi}{\partial p} \right)_{n+1} \quad (4.59)$$

$$\Delta\epsilon_q = \Delta\lambda \left(\frac{\partial\Phi}{\partial q} \right)_{n+1} \quad (4.60)$$

yielding the following relation:

$$\Delta\epsilon_p \left(\frac{\partial\Phi}{\partial p} \right)_{n+1} + \Delta\epsilon_q \left(\frac{\partial\Phi}{\partial q} \right)_{n+1} = 0 \quad (4.61)$$

being $\Phi(p, q, H^i)$ the plastic potential and for an associative flow rule, it will coincide with the yield function, i.e., $\Phi = \varphi$. Next, the evolution of the state variables is given by:

$$\boldsymbol{\sigma}_{n+1} = -g_d p_{n+1} \mathbf{I} + \frac{2}{3} g_d q_{n+1} \mathbf{N}_{n+1} \quad (4.62)$$

$$\Delta H^i = h^i(\Delta\boldsymbol{\varepsilon}^p, \boldsymbol{\sigma}_{n+1}, H_{n+1}^\gamma) \quad (4.63)$$

Box 4.1. Constitutive description of the pressure-dependent plasticity models

1. Elastoplastic decomposition of strain rate:

$$d\boldsymbol{\varepsilon} = d\boldsymbol{\varepsilon}^e + d\boldsymbol{\varepsilon}^p$$

2. Elastic stress constitutive relation in an infinitesimal deformation analysis:

$$\boldsymbol{\sigma} = \frac{\partial \psi^e}{\partial \boldsymbol{\varepsilon}^e} = \mathbf{D}^e : \boldsymbol{\varepsilon}^e$$

3. Yield condition to verify the plastic admissibility condition:

$$\varphi(p, q, H^i) = 0$$

4. Plastic flow rule:

$$d\boldsymbol{\varepsilon}^p = d\lambda \frac{\partial \Phi}{\partial \boldsymbol{\sigma}} = d\lambda \left(-\frac{1}{3} \frac{\partial \Phi}{\partial p} \mathbf{I} + \frac{\partial \Phi}{\partial q} \mathbf{N} \right)$$

5. Evolution of the internal variables:

$$d\mathbf{H} = h(d\boldsymbol{\varepsilon}^p, \boldsymbol{\sigma}, H)$$

By substituting (4.58) into Eq. (4.56), the updated stress is calculated as:

$$\boldsymbol{\sigma}_{n+1} = \boldsymbol{\sigma}_{n+1}^{tr} - g_d K \Delta \epsilon_p \mathbf{I} - 2g_d G \Delta \epsilon_q \mathbf{N}_{n+1} \quad (4.64)$$

By linking Eq. (4.62) with Eq. (4.64), one can obtain:

$$\begin{aligned} -p_{n+1} \mathbf{I} + \frac{2}{3} q_{n+1} \mathbf{N}_{n+1} \\ = -p^{tr} \mathbf{I} + \frac{2}{3} q^{tr} \mathbf{N}^{tr} - K \Delta \epsilon_p \mathbf{I} - 2G \Delta \epsilon_q \mathbf{N}_{n+1} \end{aligned} \quad (4.65)$$

Subsequently, the updated values for the state variables are computed based on the following expressions:

$$p_{n+1} = p^{tr} + K \Delta \epsilon_p \quad (4.66)$$

$$q_{n+1} = q^{tr} - 3G \Delta \epsilon_q \quad (4.67)$$

$$\boldsymbol{\sigma}_{n+1} = -g_d p_{n+1} \mathbf{I} + \frac{2}{3} g_d q_{n+1} \mathbf{N}_{n+1} \quad (4.68)$$

$$\Delta H^i = h^i(\Delta \epsilon_p, \Delta \epsilon_q, p_{n+1}, q_{n+1}, H^i) \quad (4.69)$$

The above update procedure, alongside the Eq. (4.61) and the yield limit in Eq. (4.57), compose the overall nonlinear system of equations governing the class of pressure-dependent plasticity models. According to Aravas [74], the solution of the above problem is addressed by solving the nonlinear Eqs. (4.57) and (4.61) using Taylor series expansion as follows:

$$\begin{aligned}
& \Delta\epsilon_p \left(\frac{\partial\Phi}{\partial q} \right) + \Delta\epsilon_q \left(\frac{\partial\Phi}{\partial p} \right) \\
& + \partial\Delta\epsilon_p \left[\frac{\partial\Phi}{\partial q} + \Delta\epsilon_p \left(\frac{\partial^2\Phi}{\partial q \partial \Delta\epsilon_p} \right) + \Delta\epsilon_q \left(\frac{\partial^2\Phi}{\partial p \partial \Delta\epsilon_p} \right) \right] \\
& + \partial\Delta\epsilon_q \left[\frac{\partial\Phi}{\partial p} + \Delta\epsilon_p \left(\frac{\partial^2\Phi}{\partial q \partial \Delta\epsilon_q} \right) + \Delta\epsilon_q \left(\frac{\partial^2\Phi}{\partial p \partial \Delta\epsilon_q} \right) \right] \quad (4.70) \\
& + \sum_{\gamma=1}^{n_H} \partial H^\gamma \left[\Delta\epsilon_p \left(\frac{\partial^2\Phi}{\partial q \partial (H^\gamma)} \right) + \Delta\epsilon_q \left(\frac{\partial^2\Phi}{\partial p \partial (H^\gamma)} \right) \right] \\
& = 0
\end{aligned}$$

$$\begin{aligned}
& \Phi + \left(\frac{\partial\Phi}{\partial p} \frac{\partial p}{\partial \Delta\epsilon_p} + \frac{\partial\Phi}{\partial q} \frac{\partial q}{\partial \Delta\epsilon_p} \right) d\Delta\epsilon_p + \left(\frac{\partial\Phi}{\partial p} \frac{\partial p}{\partial \Delta\epsilon_q} + \frac{\partial\Phi}{\partial q} \frac{\partial q}{\partial \Delta\epsilon_q} \right) d\Delta\epsilon_q \\
& + \sum_{\gamma=1}^{n_H} \frac{\partial\Phi}{\partial H^\gamma} dH^\gamma = 0 \quad (4.71)
\end{aligned}$$

where $n_H = 2$ is the number of internal variables that in the above introduced for the present material model. Following Eq. (4.69) the describe two internal variables in this material context, one can define the following functions:

$$k^1 = \Delta\mathbf{H}^1 - h^1(\Delta\epsilon_p, \Delta\epsilon_q, p_{n+1}, q_{n+1}, H^1, H^2) \quad (4.72)$$

$$k^2 = \Delta\mathbf{H}^2 - h^2(\Delta\epsilon_p, \Delta\epsilon_q, p_{n+1}, q_{n+1}, H^1, H^2) \quad (4.73)$$

The derivatives of the internal variables thus can be calculated as:

$$\begin{aligned}
dH^1 = & -\frac{1}{w} (J_{11} \partial\Delta\epsilon_p + J_{12} \partial\Delta\epsilon_q) \\
& - \frac{1}{w} \left(\frac{\partial p}{\partial \Delta\epsilon_p} J_{21} \partial\Delta\epsilon_p + \frac{\partial q}{\partial \Delta\epsilon_q} J_{22} \partial\Delta\epsilon_q \right) \quad (4.74)
\end{aligned}$$

$$dH^2 = -\frac{1}{w}(L_{11}\partial\Delta\epsilon_p + L_{12}\partial\Delta\epsilon_q) - \frac{1}{w}\left(\frac{\partial p}{\partial\Delta\epsilon_p}L_{21}\partial\Delta\epsilon_p + \frac{\partial q}{\partial\Delta\epsilon_q}L_{22}\partial\Delta\epsilon_q\right) \quad (4.75)$$

where the coefficients J_{ij} , L_{ij} and w are given in Appendix A.

By substituting Eq. (4.51) into Eq. (4.70), the above problem can be re-casted into the following nonlinear equations which may be solved by the Newton iterations for the correction values c_p and c_q :

$$A_{11}c_p + A_{12}c_q = b_1 \quad (4.76)$$

$$A_{21}c_p + A_{22}c_q = b_2 \quad (4.77)$$

The constants A_{ij} and b_i are given in the Appendix B. Subsequently, $\Delta\epsilon_p$ and $\Delta\epsilon_q$ are updated using the following equations:

$$\Delta\epsilon_p^{k+1} = \Delta\epsilon_p^k + c_p \quad (4.78)$$

$$\Delta\epsilon_q^{k+1} = \Delta\epsilon_q^k + c_q \quad (4.79)$$

which will be used in the evolution equations stated in the update procedure described beforehand. In the above relations, k is the Newton iteration number and the radial return algorithm converges when the correction values satisfy a prescribed tolerance. Upon convergence achievement, the state variables and the crack driving force are updated. The above integration procedure is summarized in Box 4.2.

4.3.5 Derivation of the consistent tangent moduli

The above integration procedure including the stress return algorithm is implemented via FE-based implicit user material (UMAT) code in ABAQUS. This essentially defines the task to determine the tangent matrix consistent with the algorithm which has a direct influence on convergence of the solution. Herein, an explicit definition of consistent tangent moduli based on [75] is adopted and revisited. The notations in this section and the complementary relations in Appendices are chosen to be close enough to the notation in the cited reference. This approach has also been used by recent studies such as [32] in which authors developed an enhanced Rousselier model coupled with XFEM.

In the derivation process of the linearization moduli, this approach avoids matrix inversions which is reportedly problematic specifically in 3D problems and the micromechanically-motivated models. This procedure is particularly more efficient than the Euler backward scheme such as the one proposed by Aravas [74], where one matrix inversion is inevitable.

Based on the decomposition of stress tensor into hydrostatic and deviatoric parts, the deviatoric stress may be written as:

$$\mathbf{s}_{n+1} = 2G(\boldsymbol{\epsilon}_d^e + \Delta\boldsymbol{\epsilon} - \Delta\boldsymbol{\epsilon}_d^p) \quad (4.80)$$

where $\boldsymbol{\epsilon}_d^e = \boldsymbol{\epsilon}_d^{e\ tr} = \boldsymbol{\epsilon}_d^e + \Delta\boldsymbol{\epsilon}_d$ is the elastic deviatoric strain component. By recalling $\mathbf{N} = \frac{3}{2q}\mathbf{s}$ and substituting the Eq. (4.58) into the Eq. (4.80), one can read:

$$\mathbf{s}_{n+1}^{tr} = \left(1 + \frac{3G}{q}\Delta\epsilon_q\right)\mathbf{s}_{n+1} = 2G\boldsymbol{\epsilon}_d^e \quad (4.81)$$

The inner product of the above relation with itself yields:

$$q_{n+1} + 3G\Delta\epsilon_q = 2G\sqrt{\frac{3}{2}\boldsymbol{\epsilon}_d^e : \boldsymbol{\epsilon}_d^e} \quad (4.82)$$

By defining the right hand side of the above equation as $q_{n+1}^{tr} = 2G\sqrt{\frac{3}{2}\boldsymbol{\epsilon}_d^e : \boldsymbol{\epsilon}_d^e}$ and differentiation, one can obtain:

$$\partial q_{n+1} - \partial q_{n+1}^{tr} - 3G\partial\Delta\epsilon_q = 0 \quad (4.83)$$

which can be written as:

$$\partial q_{n+1} - 3G\left(\frac{\mathbf{s}_{n+1}^{tr}}{q_{n+1}^{tr}}\partial\boldsymbol{\epsilon}_d^e - \partial\Delta\epsilon_q\right) = 0 \quad (4.84)$$

The variation of the above equation with respect to all variables gives:

$$\left(1 + \frac{3G}{q_{n+1}}\Delta\epsilon_q\right)\partial\mathbf{s}_{n+1} + \frac{3G\mathbf{s}_{n+1}}{q_{n+1}}\left(\partial\Delta\epsilon_q - \frac{\Delta\epsilon_q}{q_{n+1}}\partial q_{n+1}\right) - 2G\partial\boldsymbol{\epsilon}_d^e = 0 \quad (4.85)$$

Box 4.2. Integration procedure of the Rousselier damage model coupled with the phase-field fracture approach

1. Given the value of strain increment $\Delta \boldsymbol{\epsilon}$ and the set of state variables $(\boldsymbol{\sigma}, \boldsymbol{\epsilon}^e, \boldsymbol{\epsilon}^p, \bar{\boldsymbol{\epsilon}}^p, f)$ at time t_n compute the value of strain at time t_{n+1} .
2. Determine the elastic trial stress: $\boldsymbol{\sigma}^{tr} = \mathbf{D}^e : \boldsymbol{\epsilon}_{n+1}^e$.
3. Determine the invariants of stress tensor: $p^{tr} = \frac{1}{3} \boldsymbol{\sigma}^{tr} : \mathbf{I}$, $q^{tr} = \sqrt{\frac{3}{2} \boldsymbol{s}^{tr} : \boldsymbol{s}^{tr}}$
4. Determine the value of Δf using Newton Raphson iterations and update f .
5. Retrieve phase-field crack from common block and determine the stress degrading function $g_d = (1 - d)^2 + \kappa$.
6. Compute the yield function: $\varphi^{tr} = \varphi(p^{tr}, q^{tr}, \bar{\boldsymbol{\epsilon}}_n^p, f_n)$
7. Plastic admissibility condition; if $\varphi^{tr} \leq 0$ go to 8, otherwise go to 9.
8. Store the state variables $(\cdot)_{n+1} = (\cdot)^{tr}$ and go to the next load increment.
9. Plastic corrector stage; set Newton Raphson iteration counter $k = k + 1$ with $k_{initial} = 0$ to solve set of nonlinear equations:
$$\varphi(p^{k+1}, q^{k+1}, \bar{\boldsymbol{\epsilon}}^{p^{k+1}}, f^{k+1}) = 0$$

$$\Delta \epsilon_p^{k+1} \left(\frac{\partial \phi}{\partial q} \right) + \Delta \epsilon_q^{k+1} \left(\frac{\partial \phi}{\partial p} \right) = 0$$
10. Upon the convergence achievement go to 11. otherwise go to 9 until $k = k_{max}$.
11. Update state variables and the crack state function;
$$p = p^{tr} + \Delta \epsilon_p \quad , \quad q = q^{tr} - 3G \Delta \epsilon_q \quad , \quad \boldsymbol{s}^{tr} = \boldsymbol{s}^{tr} \left(\frac{q}{q^{tr}} \right)$$

$$\boldsymbol{\sigma}_{n+1} = g_d (\boldsymbol{s} - p \mathbf{I})$$

$$\boldsymbol{\epsilon}_{n+1}^p = \boldsymbol{\epsilon}_n^p + \Delta \epsilon_p \quad , \quad \bar{\boldsymbol{\epsilon}}_{n+1}^p = \bar{\boldsymbol{\epsilon}}_n^p + \Delta \epsilon_q$$

$$f_{n+1} = (1 - f_n) \Delta \epsilon_p$$

$$S = \eta \sigma_1 f_{n+1} D \exp \left(\frac{p}{\rho \sigma_1} \right)$$
12. If $n < n_f$ then $n = n + 1$ with n_f as the maximum number of load increments.

By replacing the Eq. (4.84) into Eq. (4.85) and re-arranging, the following relation is obtained:

$$\partial \boldsymbol{s}_{n+1} = 2G \frac{q_{n+1}}{q_{n+1}^{tr}} \partial \boldsymbol{\epsilon}_d^e + \left[\frac{9G^2 \Delta \epsilon_q}{q_{n+1} (q_{n+1}^{tr})^2} \boldsymbol{s}_{n+1} : \boldsymbol{s}_{n+1}^{tr} \right] : \partial \boldsymbol{\epsilon}_d^e - \frac{3G \boldsymbol{s}_{n+1}}{q_{n+1}} \partial \Delta \epsilon_q \quad (4.86)$$

By introducing $\mathbf{J} = \mathbf{I}:\mathbf{I}$ as the fourth order identity tensor and recalling the relation for \mathbf{N}_{n+1} , the above relation may be re-grouped as:

$$\partial \mathbf{s}_{n+1} = \left[2G \frac{q_{n+1}}{q_{n+1}^{tr}} \mathbf{J} + \frac{4G^2 \Delta \epsilon_q}{q_{n+1}^{tr}} \mathbf{N}_{n+1}:\mathbf{N}_{n+1} \right] : \partial \boldsymbol{\epsilon}_d^e - 2G \mathbf{N}_{n+1} \partial \Delta \epsilon_q \quad (4.87)$$

For cases with three direct strain components, one can read:

$$\partial \boldsymbol{\epsilon}_d^e = \left(\mathbf{J} - \frac{1}{3} \mathbf{I}:\mathbf{I} \right) : \partial \boldsymbol{\epsilon} \quad (4.88)$$

and

$$\partial p_{n+1} = -K \mathbf{I}:\partial \boldsymbol{\epsilon}_{n+1} + K \partial \Delta \epsilon_p \quad (4.89)$$

$$\partial (\sigma_{m\ n+1} \mathbf{I}) = (K \mathbf{I}:\mathbf{I}) : \partial \boldsymbol{\epsilon}_{n+1} - K \mathbf{I} \partial \Delta \epsilon_p$$

By differentiating the Eq. (3.17) and combining Eqs. (4.88) and (4.89)₂ into Eq. (4.87), we obtain:

$$\partial \boldsymbol{\sigma}_{n+1} = \mathbf{Z}:\partial \boldsymbol{\epsilon}_{n+1} - K \mathbf{I} \partial \Delta \epsilon_p - 2G \mathbf{N}_{n+1} \partial \Delta \epsilon_q \quad (4.90)$$

where

$$\mathbf{Z} = 2G \frac{q_{n+1}}{q_{n+1}^{tr}} \mathbf{J} + \left(K - \frac{2G}{3} \frac{q_{n+1}}{q_{n+1}^{tr}} \right) \mathbf{I}:\mathbf{I} + \frac{4G^2 \Delta \epsilon_q}{q_{n+1}^{tr}} \mathbf{N}_{n+1}:\mathbf{N}_{n+1} \quad (4.91)$$

For simplicity in notation, the subscript of the variables are omitted from now on in this section unless otherwise specified. Taking the variations of nonlinear Eqs. (4.57) and (4.61) with respect to $\boldsymbol{\sigma}_{n+1}$, gives:

$$\begin{aligned} & \partial \Delta \epsilon_p \left(\frac{\partial \Phi}{\partial q} \right) + \partial \Delta \epsilon_q \left(\frac{\partial \Phi}{\partial p} \right) + \Delta \epsilon_p \left(\frac{\partial^2 \Phi}{\partial p \partial q} \frac{\partial p}{\partial \boldsymbol{\sigma}} + \frac{\partial^2 \Phi}{\partial q^2} \frac{\partial q}{\partial \boldsymbol{\sigma}} \right) \partial \boldsymbol{\sigma} \\ & + \Delta \epsilon_q \left(\frac{\partial^2 \Phi}{\partial p^2} \frac{\partial p}{\partial \boldsymbol{\sigma}} + \frac{\partial^2 \Phi}{\partial p \partial q} \frac{\partial q}{\partial \boldsymbol{\sigma}} \right) \partial \boldsymbol{\sigma} \\ & + \left(\Delta \epsilon_p \frac{\partial^2 \Phi}{\partial q \partial H^1} + \Delta \epsilon_q \frac{\partial^2 \Phi}{\partial p \partial H^1} \right) \partial H^1 \\ & + \left(\Delta \epsilon_p \frac{\partial^2 \Phi}{\partial q \partial H^2} + \Delta \epsilon_q \frac{\partial^2 \Phi}{\partial p \partial H^2} \right) \partial H^2 = 0 \end{aligned} \quad (4.92)$$

$$\left(\frac{\partial \Phi}{\partial p} \frac{\partial p}{\partial \boldsymbol{\sigma}} + \frac{\partial \Phi}{\partial q} \frac{\partial q}{\partial \boldsymbol{\sigma}} \right) \partial \boldsymbol{\sigma} + \frac{\partial \Phi}{\partial H^1} \partial H^1 + \frac{\partial \Phi}{\partial H^2} \partial H^2 = 0 \quad (4.93)$$

The differentiations of the internal variables may be written based on the Eqs. (4.72) and (4.73) as:

$$dH^1 = -\frac{1}{w} (J_{11} d\Delta\epsilon_p + J_{12} d\Delta\epsilon_q) - \frac{1}{w} \left(J_{21} \frac{\partial p}{\partial \sigma} + J_{22} \frac{\partial p}{\partial \sigma} \right) d\sigma \quad (4.94)$$

$$dH^2 = -\frac{1}{w} (L_{11} d\Delta\epsilon_p + L_{12} d\Delta\epsilon_q) - \frac{1}{w} \left(L_{21} \frac{\partial p}{\partial \sigma} + L_{22} \frac{\partial p}{\partial \sigma} \right) d\sigma \quad (4.95)$$

Substituting Eqs. (4.94) and (4.95) into Eqs. (4.92) and (4.93) leads to a set of two nonlinear equations as:

$$\bar{A}_{11} \partial \Delta\epsilon_p + \bar{A}_{12} \partial \Delta\epsilon_q = (B_{11} \mathbf{I} + B_{12} \mathbf{N}) : \partial \sigma \quad (4.96)$$

$$d\bar{A}_{21} \partial \Delta\epsilon_p + \bar{A}_{22} \partial \Delta\epsilon_q = (B_{21} \mathbf{I} + B_{22} \mathbf{N}) : \partial \sigma \quad (4.97)$$

where the coefficients \bar{A}_{ij} and B_{ij} are given in Appendix C. By substituting Eq. (4.90) into Eqs. (4.96) and (4.97), one can read:

$$\partial \Delta\epsilon_p = (C_{11} \mathbf{I} + C_{12} \mathbf{N}) : \mathbf{Z} : \partial \epsilon \quad (4.98)$$

$$\partial \Delta\epsilon_q = (C_{21} \mathbf{I} + C_{12} \mathbf{N}) : \mathbf{Z} : \partial \epsilon \quad (4.99)$$

where the coefficients C_{ij} are given in Appendix D. To link the variation of the stress with strain and obtain the desired expression for the consistent tangent moduli, the set of Eqs. (4.98) and (4.99) is inserted into Eq. (4.90), gives:

$$\partial \sigma = \mathbf{M} : \mathbf{Z} : \partial \epsilon \quad (4.100)$$

where

$$\mathbf{M} = \mathbf{J} - \mathbf{M}^I - \mathbf{M}^N$$

$$\mathbf{M}^I = K(C_{11} \mathbf{I} : \mathbf{I} + C_{12} \mathbf{I} : \mathbf{N}) \quad (4.101)$$

$$\mathbf{M}^N = 2G(C_{21} \mathbf{N} : \mathbf{I} + C_{22} \mathbf{N} : \mathbf{N})$$

By multiplying \mathbf{M} and \mathbf{Z} , the following explicit form of the consistent tangent moduli for family of pressure-dependent plasticity models is obtained:

$$\mathbf{D}^p = d_0 \mathbf{J} + d_1 \mathbf{I} : \mathbf{I} + d_2 \mathbf{N} : \mathbf{N} + d_3 \mathbf{I} : \mathbf{N} + d_4 \mathbf{N} : \mathbf{I} \quad (4.102)$$

where

$$\begin{aligned}
d_0 &= 2G \frac{q}{q^{tr}} \\
d_1 &= K - \frac{2G}{3} \frac{q}{q^{tr}} - 3K^2 C_{11} \\
d_2 &= \frac{4G^2}{q^{tr}} \Delta \epsilon_q - 4G^2 C_{22} \\
d_3 &= -2GK C_{12} \\
d_4 &= -6GK C_{21}
\end{aligned} \tag{4.103}$$

It worth to note that the tangent is symmetric if $C_{12} = 3C_{21}$. To take into consideration the influence of the phase-field evolution within the mechanical problem solution, the degradation of the phase-field is multiplied by the above tangent.

In this study, the above formulation for the tangent including the derivatives of variables are coded into the UMAT routine, which is essential to obtain a converged solution of the implicit algorithm.

5 Numerical results

The main body of the numerical simulations and results corresponding to the material models described in the previous chapters are presented in this chapter. Several popular benchmarks are adopted from literature to analyse the predictability and performance of the discussed algorithms, with the emphasis on the crack initiation and propagation. These fracture benchmarks are selected in a way to cover a wide range of stress states, based on the type of loading conditions and geometrical aspects.

The primary aspects of the numerical modelling hereinafter could be described as follows:

1. Identification of the material parameters using the literature/laboratory-based data from the experimental tests.
2. Determination of the material hardening following the provided laboratory data of engineering stress versus strain curves.
3. Monitoring the material plastic deformation and damage localisation during the loading process.
4. Observation of the initiating crack zone due to the extensive localisation of plastic deformation and damage accumulation.
5. Topological observation of the crack propagation, which can include crack branching/merging until the final material rupture.
6. Quantitative analysis by comparing the global material response of the finite element simulation with the experimental data tests.
7. Mesh objectivity study in regards with the nonlocal gradient regularisation method.

The numerical study in this chapter first starts with validation of the phase-field staggered solution strategy that is described in the previous chapter in the absence of ductile damage material coupling. Then a series of numerical simulations are carried out to evaluate the performance of the coupled phase-field diffusive ductile fracture model and, at some points, relevant comparisons with the results from local approaches to fracture are highlighted. Last section is devoted to numerical assessment of the nonlocal gradient

regularisation method implemented using the thermo-mechanical finite element procedure discussed in section 4.1.3, focusing on mesh sensitivity analysis.

5.1 Phase-field solution method validation in brittle setting

As it was described in the previous chapter, the multi-field solution of the phase-field problem is obtained using a staggered solution strategy by considering a *competition* between the phase field and displacement field. A combination of UEL and UMAT modules in ABAQUS is utilised, where the phase-field equation is treated via a direct sparse solver embedded in the Abaqus UEL code and the mechanical field as well as the history field is computed using the UMAT subroutine. A common block is served to transfer data including the history field in between the codes.

To initialise the code and verify the performance of the staggered algorithm, we confine ourselves to the brittle setting at this point with the focus on the comparison between the numerical and analytical solutions based on a simple one-dimensional example.

5.1.1 Verification of the solution on a single element

A single 2D plane strain 4 node quadrilateral element formulated with reduced integration method (CPE4R) is considered. The dimensions of the element are $1 \times 1 \text{ mm}^2$ in x and y directions, where it is subjected to tensile and shear loading conditions, as depicted in Figure 5.1. The elastic properties are taken as $E = 180 \text{ GPa}$ and $\nu = 0.28$. The phase field length scale parameter $l_d = 0.005 \text{ mm}$ and the critical energy release rate $\mathcal{G}_c = 20.9 \text{ N/mm}$ are adopted which are given as the entries for the material input property in the UEL code. Concerning tensile loading, $\varepsilon_x = \varepsilon_{xy} = 0$ and $\varepsilon_y \neq 0$, one can obtain the reference stress as $\sigma_0 = D_{22}\varepsilon_y$, where $D_{22} = \frac{E(1-\nu)}{(1+\nu)(1-2\nu)}$ is obtained based on the Hooke's law. Having the reference elastic energy $\psi_0 = \frac{1}{2}\sigma_0\varepsilon_y$, the phase field parameter may be analytically obtained via solution of the minimisation problem in Eq. (4.20), given by:

$$d = \frac{2\psi_0}{2\psi_0 + \frac{G_c}{l_d}} \quad (5.1)$$

Using the quadratic phase-field degradation function in Eq. (4.28), the stress tensor and the elastic tangent are degraded, respectively determined by $\sigma_y = g(d)\sigma_{y0}$ and $\mathbf{D}^e = g(d)\mathbf{D}^e$ and are introduced in the user module (UMAT). The numerical simulation is carried out using static analysis and displacement-controlled boundary condition with the axial displacement increment $\Delta u_y = 0.001 \text{ mm}$ per step (total number of 1000 increments).

The force $F_y = \sigma_y A_0$ versus displacement graphs for the analytical solution and the simulation are given in Figure 5.2 and a very close agreement is observed. Figure 5.3 depicts the successful validation of the algorithm through high accordance between the numerical and analytical solutions for the phase field evolution history.

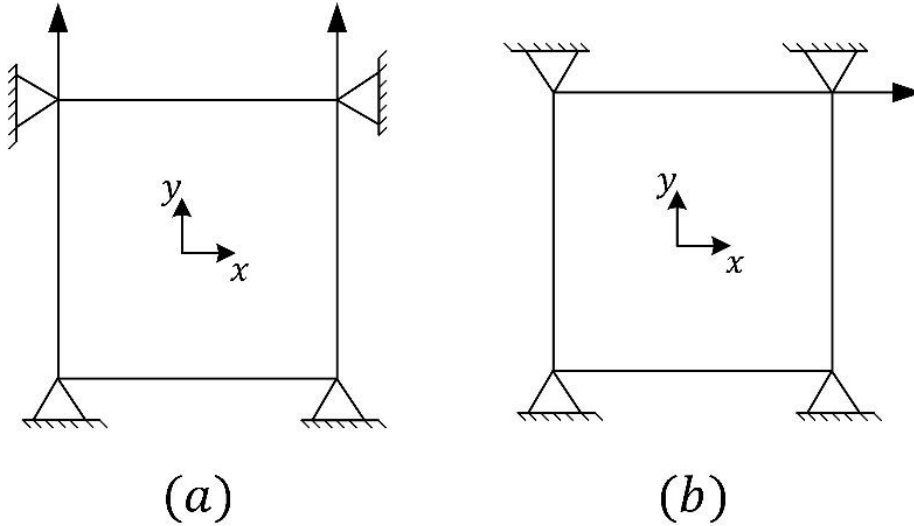


Figure 5.1 Single plane strain element under a) tensile and b) shear loading

The same procedure is followed for the simple shear case on the same element (Figure 5.1(b)), and the verified force-displacement results are presented in Figure 5.4. Attention is drawn to the adequately small size of the time increments to obtain the accurate solution. The length scale sensitivity of the model is illustrated in Figure 5.5 for the element under tension via the stress-strain and phase-field history curves. These results are in conformity with the critical stress (σ_c) and its corresponding strain (ε_c) values in the following expressions for the used quadratic degradation function, as a decline in the maximum force is observed for a larger length scale value:

$$\sigma_c = \frac{9}{16} \sqrt{\frac{E\mathcal{G}_c}{6l_d}} \quad , \quad \varepsilon_c = \sqrt{\frac{\mathcal{G}_c}{6l_d E}} \quad (5.2)$$

Based on these expressions, the phase-field diffusive problem coincides with the Griffith discrete crack approach in the limit of $l_d \rightarrow 0$, where the stress goes to infinity.

5.1.2 Phase-field crack in 2D analysis

The numerical analysis of the phase-field crack solution in the brittle setting is pursued in this section. Two of well-known 2D fracture benchmarks are analysed through the evolution of phase-field crack and the performance of the staggered solution algorithm is verified by comparing to the crack propagation patterns that were reported in literature.

Single edge notched tensile specimen:

A single edge tensile notched specimen is analysed under the tensile loading conditions. The elastic properties and the critical energy values used in the simulation are chosen as $E = 210 \text{ GPa}$, $\nu = 0.28$ and $\mathcal{G}_c = 20.9 \text{ N/mm}$. The geometry and boundary conditions of the single edge notched tensile (SENT) specimen is depicted in Figure 5.6 (a), where a horizontal notch with half size of the squared plate is considered.

The part is discretized with plane stress quadrilateral elements (CPS4) whereby the minimum element edge size of $b_h = 0.005 \text{ mm}$ is assumed in the vicinity of the areas prone to crack development. The phase-field crack length parameter value of $l_d = 0.01 \text{ mm}$ is adopted. Displacement-controlled monotonic loading is imposed on the top edge of the specimen at the first step with $\Delta u_y = 0.01 \text{ mm}$ for 60 increments and then $\Delta u_y = 0.001 \text{ mm}$ for the second step until the end of the loading in order to precisely capture the fracture process.

The evolution of the crack consisting of initiation, propagation and branching/merging is illustrated via the contours of phase-field in Figure 5.6 (b-d), showing a horizontal crack propagation path, similar to the results presented in [69].

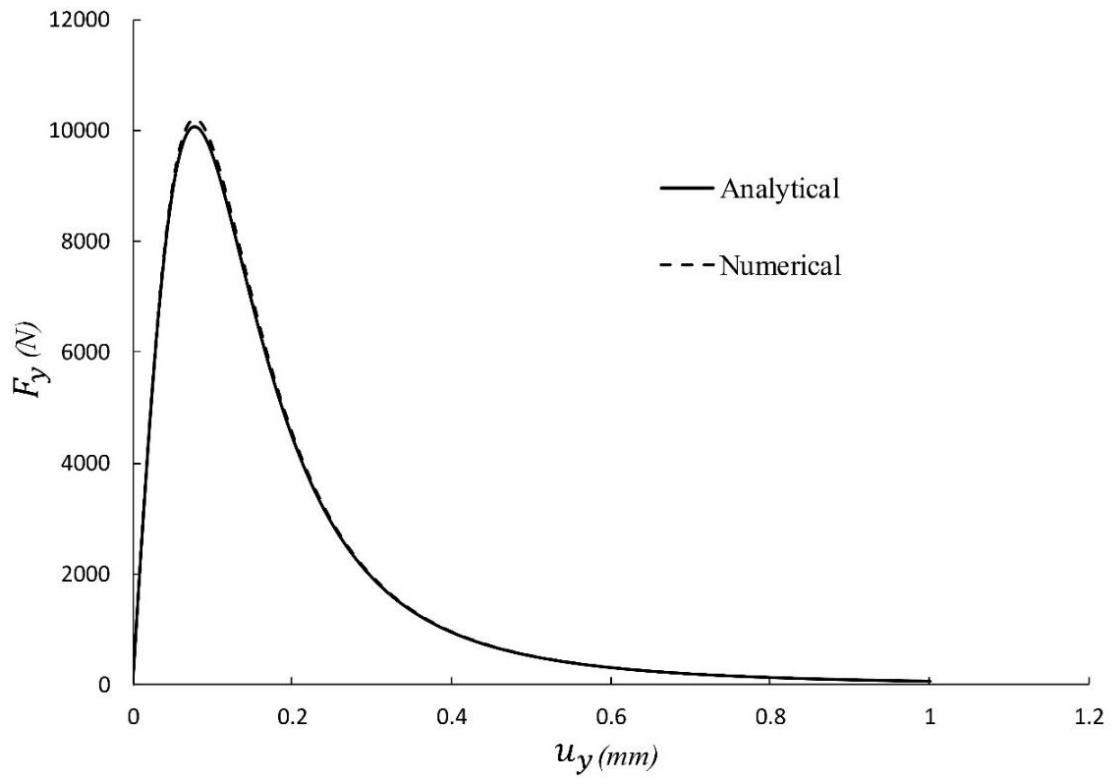


Figure 5.2 Analytical versus numerical load history for the single tensile element

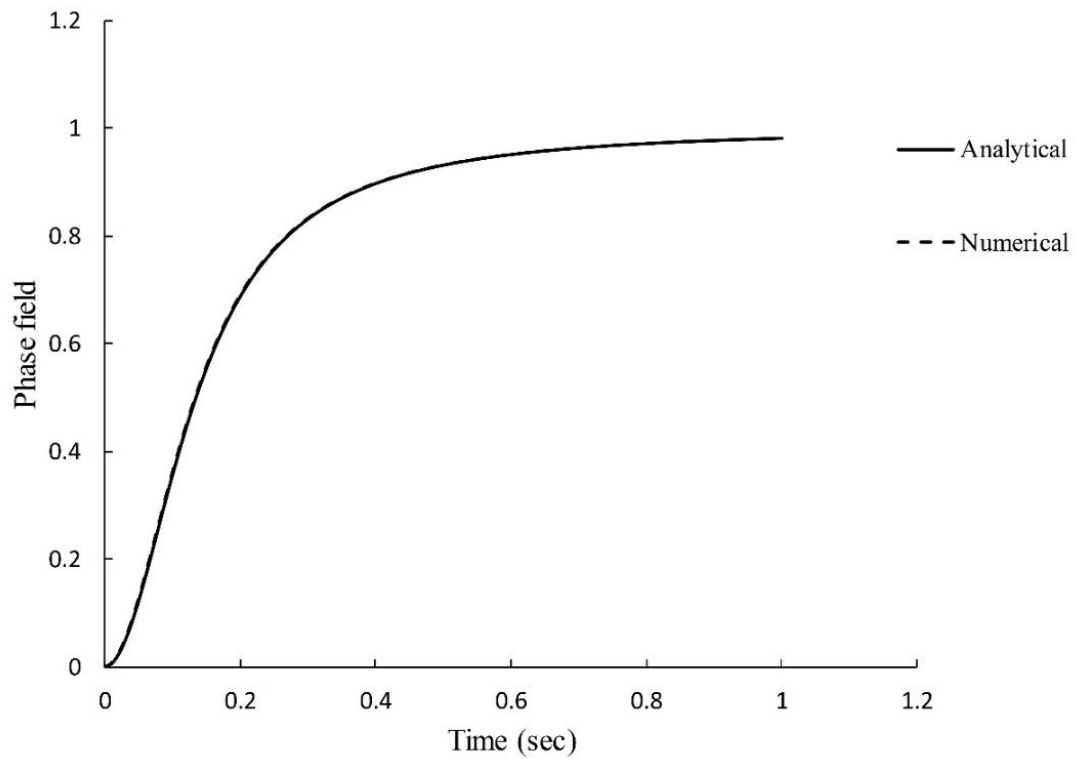


Figure 5.3 Analytical versus numerical phase field history for the single tensile element

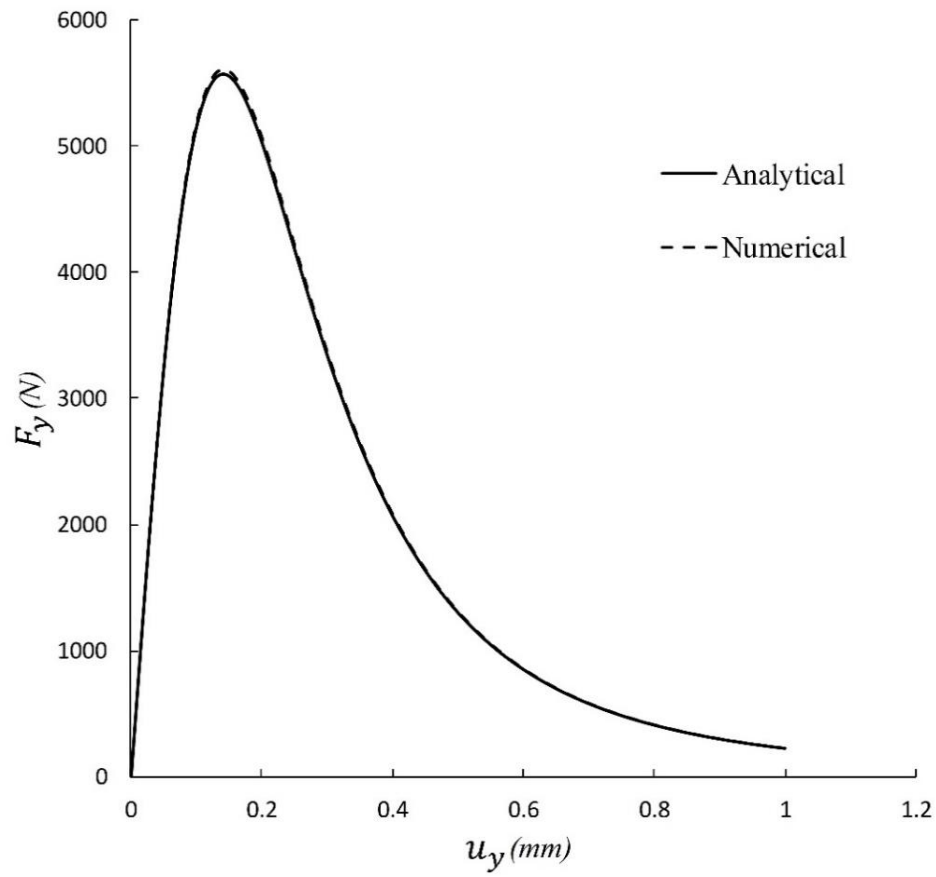


Figure 5.4 Analytical versus numerical load history for the single shear element

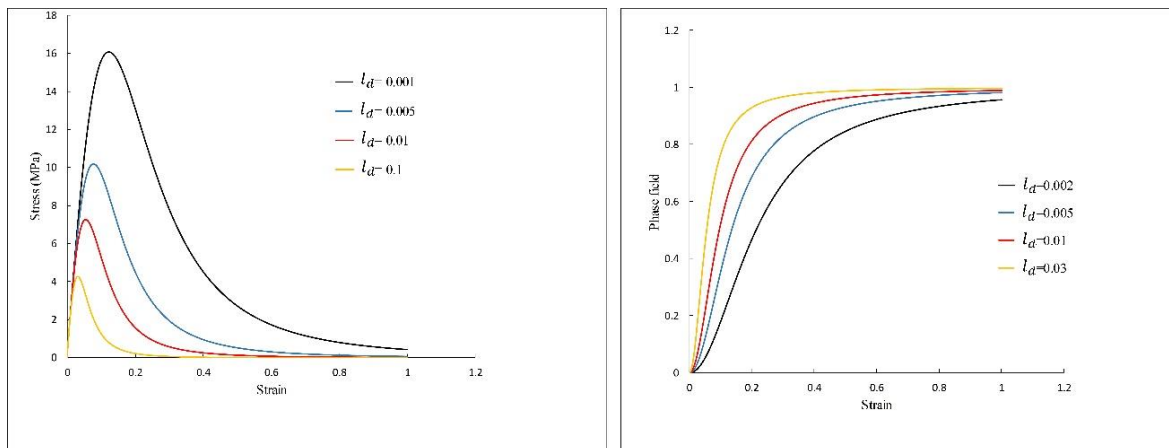


Figure 5.5 Length scale sensitivity of the phase-field problem for the single tensile element

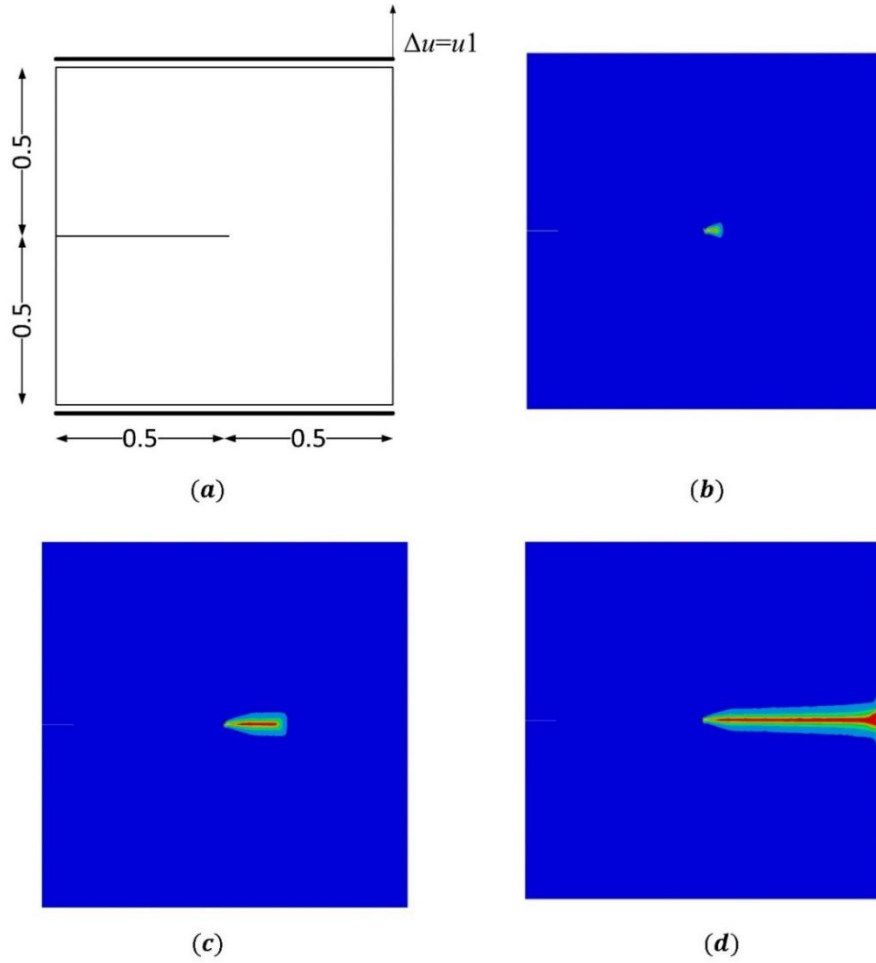


Figure 5.6 Single edge notched tensile test a) geometry and boundary conditions and crack development at b) $u_1 = 0.005 \text{ mm}$, c) $u_1 = 0.00622 \text{ mm}$ and d) $u_1 = 0.00705 \text{ mm}$

Double asymmetrical notched specimen:

The second fracture benchmark is the double asymmetrical notched specimen, loaded on the vertical direction with a monotonic incremental displacement of $\Delta u_y = 0.001 \text{ mm}$ throughout the process. The misaligned pre-cracked solid geometry and boundary conditions are shown in Figure 5.7 (a), as previously tested in [76,77], among others.

The crack development, branching and merging pattern is of interest in this benchmark considering the geometrical aspects. The set of parameters are chosen as the same of the previous example, namely $E = 210 \text{ GPa}$, $\nu = 0.28$ and $\mathcal{G}_c = 20.9 \text{ N/mm}$. The spatial discretisation is performed using plane strain quadrilateral elements (CPE4R) with minimum edge size of $b_h = 0.1 \text{ mm}$ near the critical areas, resulted in 44751 total

number of elements. The length scale is opted as $l_d = 0.2 \text{ mm}$ that is large enough having in view the finite element mesh discretisation.

The contour plots of the phase-field are depicted in Figure 5.7 (b-d) at three sequential displacements, showing the initiation of cracks at the notch tips, evolution of the cracks horizontally and their clockwise extension in a curvilinear pattern. The obtained crack topology is in a high accordance with the simulated results in the literature, for instance in [76].

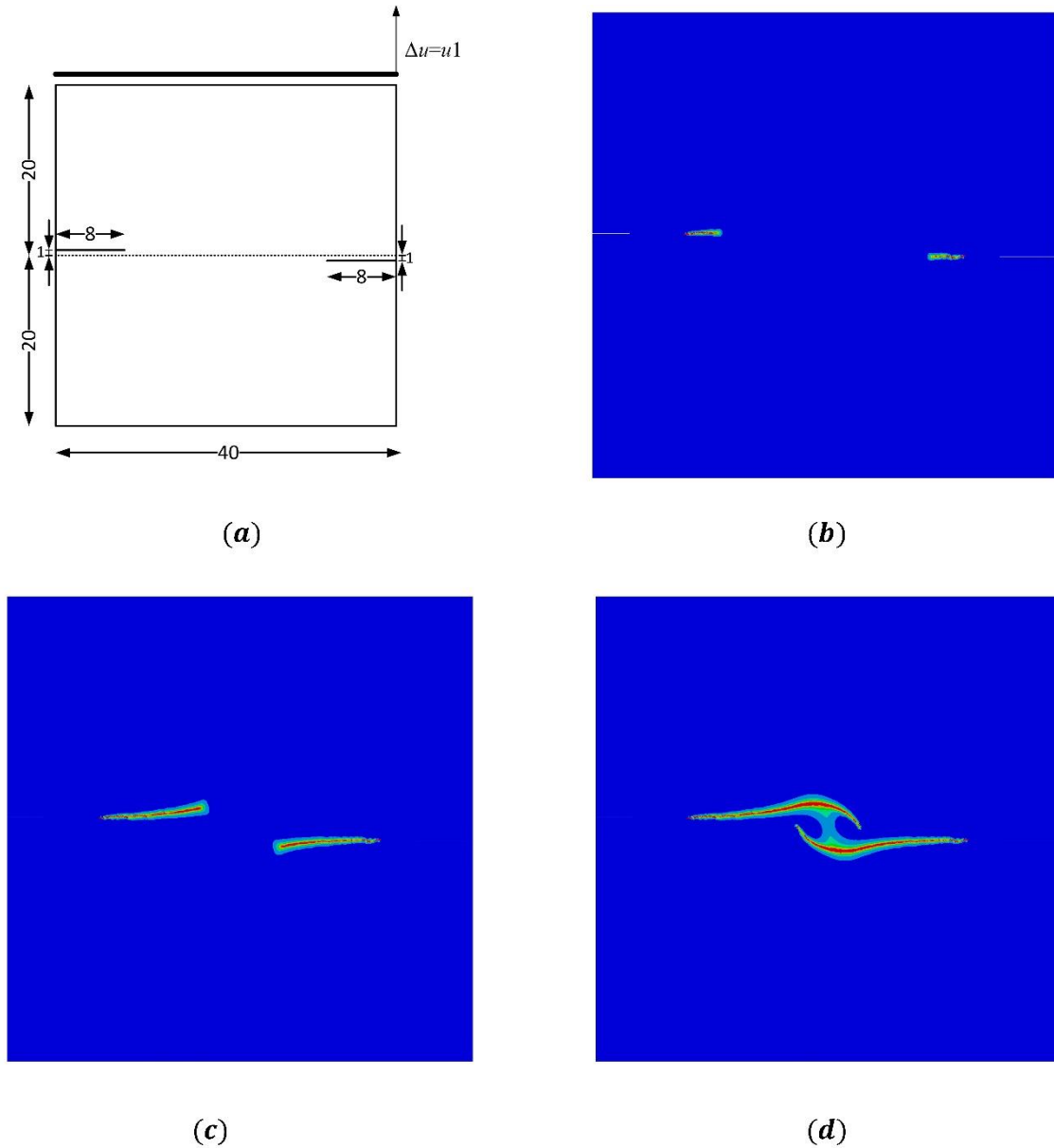


Figure 5.7 Double asymmetrical notched sample a) geometry and boundary conditions and crack development at b) $u_1 = 0.0296 \text{ mm}$, c) $u_1 = 0.0386 \text{ mm}$ and d) $u_1 = 0.05 \text{ mm}$

5.2 Numerical modelling of fracture using the phase-field coupled ductile fracture model:

In this section the analysis of the performance of the phase-field model coupled with ductile damage law is assessed. The validation procedure on several benchmark tests from literature consists of the following steps:

1. Identification of the parameters related to the local damage model description.
2. Adoption of suitable parameters related to the phase-field diffusive equation.
3. Monitoring of the accumulation of damage through the evolution of the void volume fraction until the initiation of crack upon the limit to the critical value.
4. Observation of the crack propagation in the post-critical regime through the evolution of the phase-field crack parameter.
5. Comparisons with the literature data via crack trajectory analysis and qualitative assessment of the global material response.

The benchmarking samples are chosen to cover wide range of stress states based on the type of loading and geometrical aspects. The plane problem configuration is considered throughout the simulations. As a standard procedure, the performance of the coupled model algorithm is initially verified on a single plane element in the following section.

5.2.1 Verification of the coupled model on a single element

A single quadrilateral plane strain element (CPE4R) under tension is adopted (Figure 5.1 (a)). A monotonic tensile loading condition is considered as the bottom edge of the element is fixed and a displacement of 0.01 mm/sec is applied on the top edge of the element. This test runs for initial validation of the code and more importantly the role of the fracture coefficient in the material softening regime. Since the actual crack propagation is not of interest, the phase-field length scale parameter does not need to follow the common criterion to be essentially larger than the element size.

The structural response is analysed through the axial stress versus strain curve variations, for different fracture coefficient parameters, in the plots of Figure 5.8. The elastoplastic plot refers to the graph that is obtained via the built-in standard von Mises plasticity model

available in ABAQUS material library and the non-diffusive response is attributed to the *local* Rousselier damage model, in which *local* term henceforth represents to the procedure in which the damaged material model is processed without the activation of the phase-field diffusive solver.

One can clearly observe the higher ductility of the local model against the diffusive model, whereby in the coupled model the softening is accelerated as the fracture coefficient is increasing. This behaviour is visible in the post coalescence regime starts from the point where vertical displacement reaches $u_2 = 0.49 \text{ mm}$. This point is associated with the prescribed crack initiation criterion based on the critical value of the void volume fraction $f_c = 0.01$.

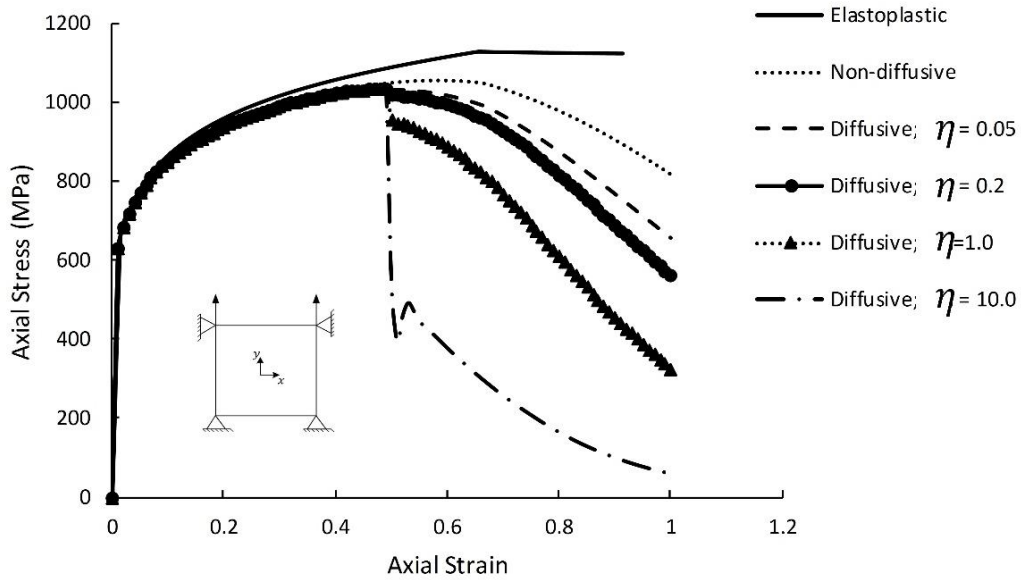


Figure 5.8 Influence of the fracture coefficient on the material response of the single element using the diffusive ductile fracture model

5.2.2 Tensile test on round bars

The coupled and local damage models are assessed on a smooth round bar (SRB) and a notched round bar (NRB) with notch radius of 20 mm under tensile loading, as have been experimentally and numerically addressed in Li et al. [78]. The geometry and dimension of the samples are depicted in Figure 5.9. The material behaviour is first addressed with the utilisation of the CDM-based ductile damage laws, including the Lemaitre and

Rousselier models. The intention here is to evaluate and compare the predictive ability of these material models in the softening regime until the material rupture, primarily through the observation of the stress response.

The material data of Al-6061(T6) that is chosen for both samples is presented in Table 5.1. The experimental procedure in [78] is performed under the velocity of 1 mm/min to obtain the rate-independent material response, which ensures the applicability of the material models of our study in these samples. The isotropic material hardening is assumed using the power law $R = 561(0.015 + \bar{\epsilon}^p)^{0.11}$, which is obtained based on an inverse finite element procedure in [78]. The parameters of Rousselier damage are chosen as $D = 2$ and $\sigma_1 = \frac{2\sigma_y}{3} \approx 236 \text{ MPa}$ as suggested in [79] in both examples. Only one quarter of the specimens are simulated by defining proper symmetries. The spatial discretisation is performed using four-node quadrilateral bilinear axisymmetric elements with reduced integration method (CAX4R) where structured mesh pattern is assumed and the finest element distribution is considered in the areas of crack with the edge sizes $b_h = 0.2 \text{ mm}$ and $b_h = 0.16 \text{ mm}$, respectively for SRB and NRB samples.

The simulations that correspond to the Rousselier local material model are carried out to reveal the influence of the initial porosity on the material global response. Considering that this study concerns the phase-field model ductile description based on the Rousselier model, the graphs related to the implemented Lemaitre damage model are solely presented for comparison purposes at this step, whereby the version of the model that is accompanied with the damage threshold definition is considered.

The stress response based on the Rousselier and Lemaitre local damage models (indicated by “RSL” and “LM” in plots respectively) are demonstrated via the force-displacement graphs for the SRB and NRB samples in Figure 5.10 and Figure 5.11, respectively. By comparing the results with the experimental data, the effect of the initial porosity on the material softening behaviour may be clearly observed. In the post critical regime, the Rousselier damage model response is in closer agreement with the experimental curve for the value of initial porosity $f_0 = 0.0001$. This can be closely related to the graph obtained by Lemaitre model for $\bar{\epsilon}_c^p = 0.5$.

Table 5.1 Material parameters of Al-6061(T6) used for the numerical modelling of tensile samples

Parameter	Symbol	Value	unit
Young's modulus	E	68.9	GPa
Poisson's ratio	ν	0.33	—
RSL parameter	σ_1	236.0	MPa
RSL parameter	D	2.0	—
LM parameter	r_1	6.0	—
LM parameter	r_1	1.0	—
LM parameter	ε_c^p	0.05,0.1,0.3,0.5	—
Initial porosity	f_0	0.0001,0.002	—
Critical porosity	f_c	0.043	—
Critical energy release rate	\mathcal{G}_c	0.018	kN/mm
length parameter	l_d	0.3	mm
Fracture coefficient	η	0.1,1.0,5.0	—

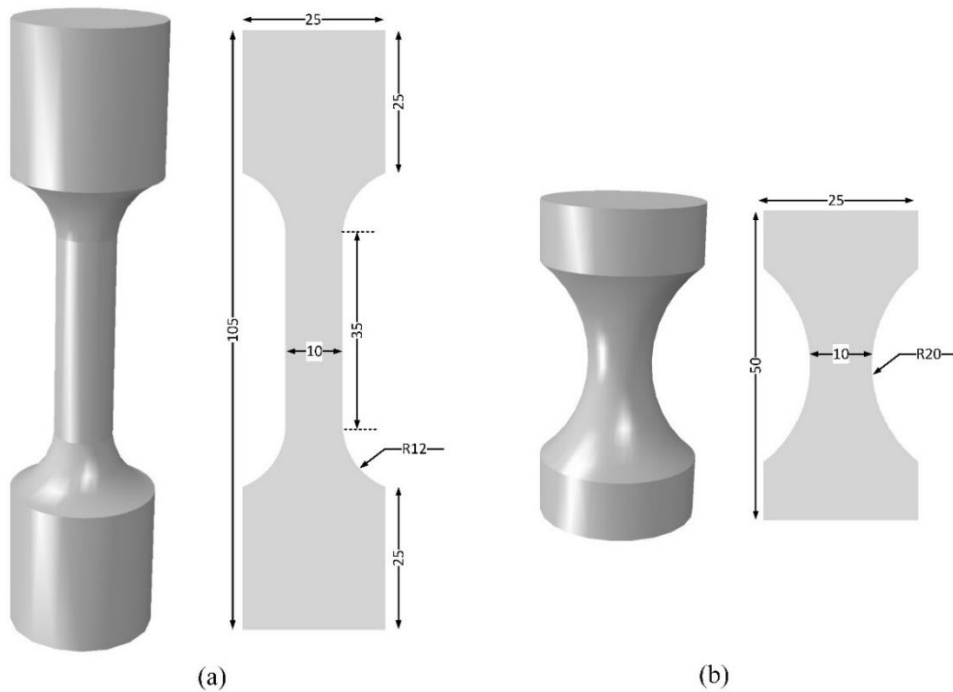


Figure 5.9 Tensile test on a) smooth round bar and b) notched round bar with notch radius of 20; dimensions are in mm

By performing similar simulation procedure for the NRB sample, one can see the good accordance of the Rousselier material response to the experimental one for the initial porosity of $f_0 = 0.002$, where the Lemaitre model could not capture the accelerated material softening after the displacement of $u_1 \approx 1 \text{ mm}$. Therefore, the identified values for the initial void volume fraction are $f_0 = 0.0001$ and $f_0 = 0.002$ and are being used in the following simulations for the SRB and NRB samples, respectively. From the experiments in [78] and image analysis, the latter value for f_0 and the critical value of $f_c = 0.043$ were determined to be used for simulation using porous damage criterion therein.

The global response obtained by the phase-field ductile fracture model is indicated in Figure 5.12. The variations of the results are compared in terms of the fracture coefficient, whereby increasing its value significantly induced more material degradation due to a higher value for crack driving force, hence a larger phase-field value. Also in both samples, an acceptable correlation between the simulated results with the unit value of fracture coefficient and the experiments of Li et al. [78] can be found.

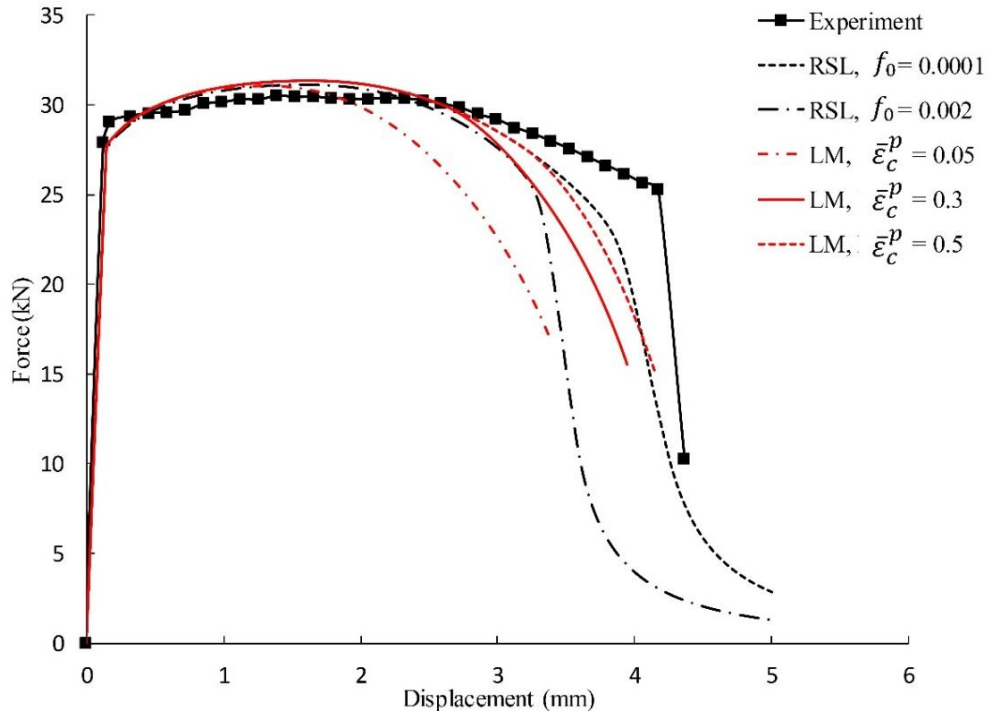


Figure 5.10 Force vs. displacement using local damage models for the SRB sample

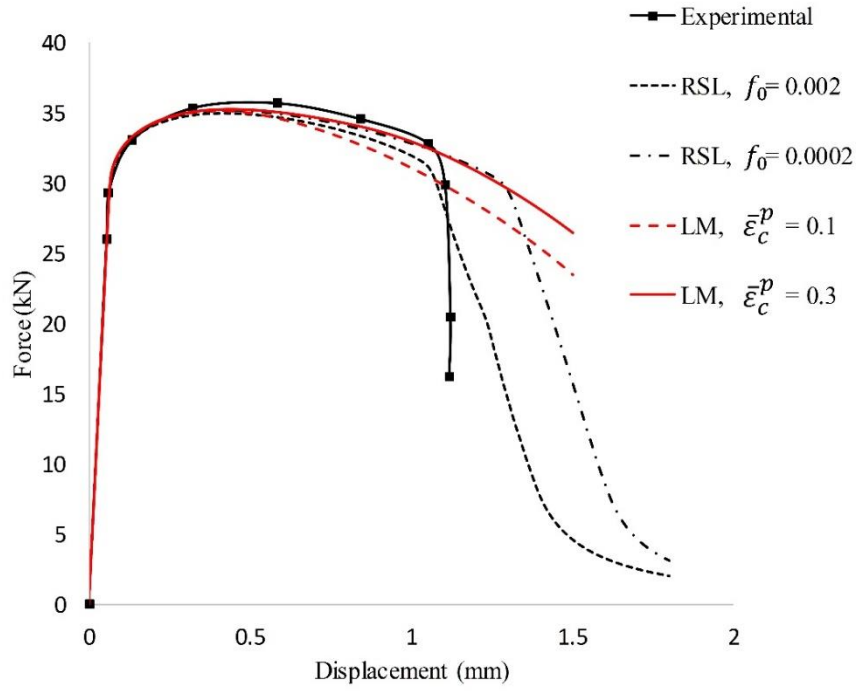


Figure 5.11 Force vs. displacement using local damage models for the NRB sample

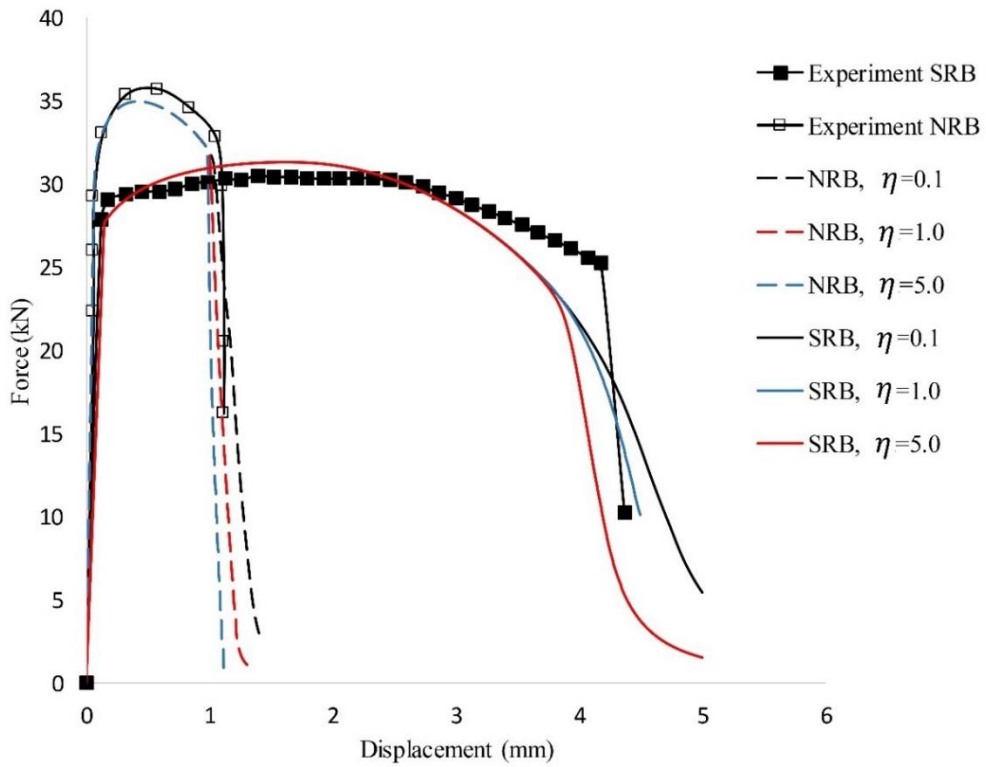


Figure 5.12 Influence of the fracture coefficient on the global response of the SRB and NRB samples using the coupled phase-field ductile fracture model

The contour plots of the NRB tensile test are indicated in Figure 5.13, where the evolution of the equivalent plastic strain ($\bar{\epsilon}^p$), void volume fraction (f) and the phase-field (d) are presented for different load increments. The void volume fraction evolves from the prescribed initial value, $f_0 = 0.002$, alongside the plastic deformation throughout the simulation. Upon the time increment that it coincides with the prescribed critical value, $f_c = 0.043$, the crack initiation criterion is met.

Subsequent to this point, the crack propagation is modelled by the development of the phase-field crack that is induced by the evolution of the void volume fraction that takes effect in the crack driving force. Accordingly, the crack grows from the centre of the specimen towards the notch roots horizontally. This may be in conformity with the observations in [78] in which a large distribution of voids were identified in the centre of the specimen by fractographic analysis. The plots of the void volume fraction are presented from the initial value to the critical value, in this example within the increments of $u_1 = 0.842 \text{ mm}$ to $u_1 = 0.992 \text{ mm}$.

The variation of the triaxiality along the bottom edge of the quarter of specimens is represented in Figure 5.14. The graphs are taken when the deformation reaches the critical level, i.e. when crack initiates, showing the highest value in the centre of the specimens. The curves of Figure 5.15 depict the stress triaxiality changes against the equivalent plastic strain. One can see that it initiates from around $\tau = 0.33$ and $\tau = 0.66$, respectively for the NRB and SRB samples and that it increases rapidly during the localisation of the plastic deformations. This can be closely related to the graphs of triaxiality that were reported in [78].

5.2.1 Tensile test on asymmetrical notched specimen:

Crack propagation and merging is investigated in the asymmetrical notched specimen under tension, which was studied in [80], among others. The geometry and boundary conditions of the specimen are illustrated in Figure 5.16, where a monotonic displacement-controlled load is applied on the upper part of the specimen in the vertical direction as the horizontal movement is prohibited. The lower part of the specimen is fixed. The thickness of the specimen is 3 mm . The material parameters and the elastic properties and hardening function are chosen in conformity with Al-5005 and a nonlinear hardening function used according to [80]. The set of material data is given in Table 5.2. Regarding the value of the critical energy release rate, authors therein conducted several

tests on a compact tension (CT) specimen for the aluminium samples and obtained the value based on the initial crack length until the onset of the crack propagation.

The simulation herein is carried out with two-dimensional plane stress quadrilateral elements formulated with reduced integration method (CPS4R), in which a structured mesh with higher density is adopted within the potential region for fracture (with element edge size $b_h = 0.4 \text{ mm}$). The non-diffusive i.e. the *local* Rousselier model is initialized by adopting $\sigma_1 = \frac{2\sigma_y}{3} \approx 75 \text{ MPa}$ and $D = 2$ in a similar manner to the previous example.

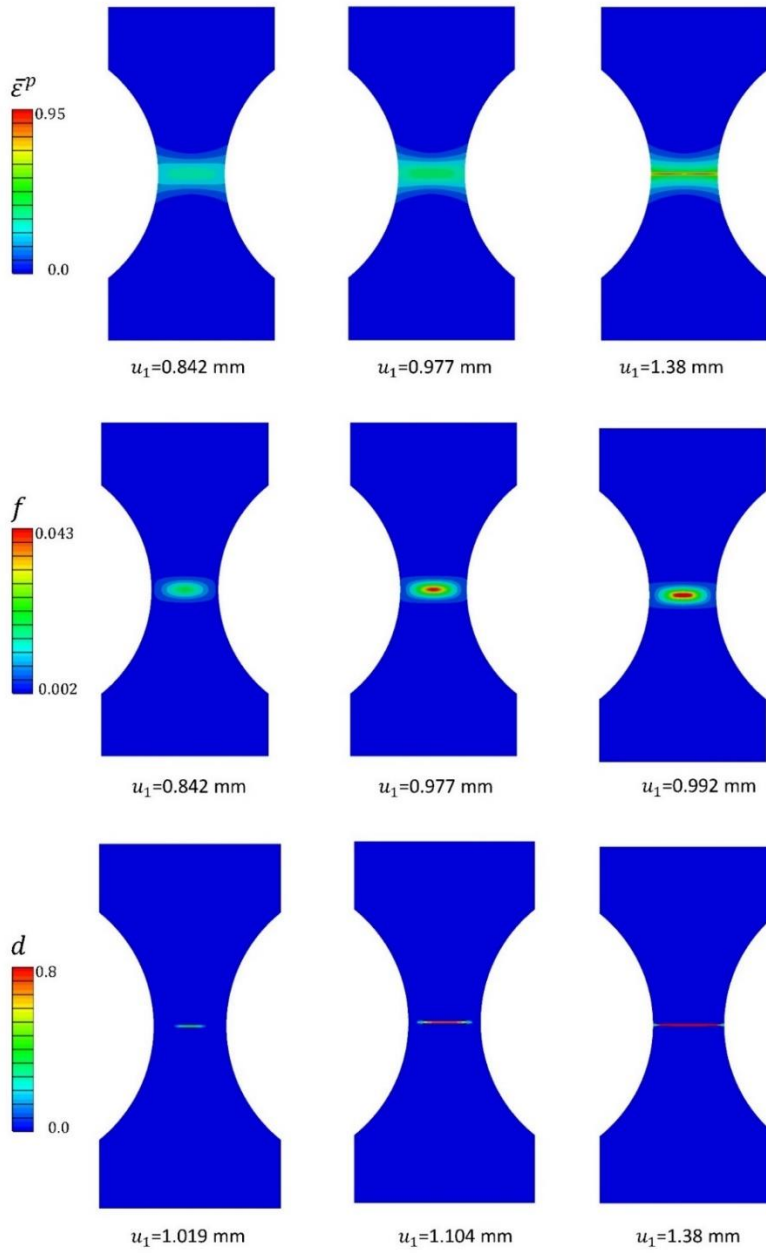


Figure 5.13 Contour plots of the equivalent plastic strain, void volume fraction and phase-field at different load increments

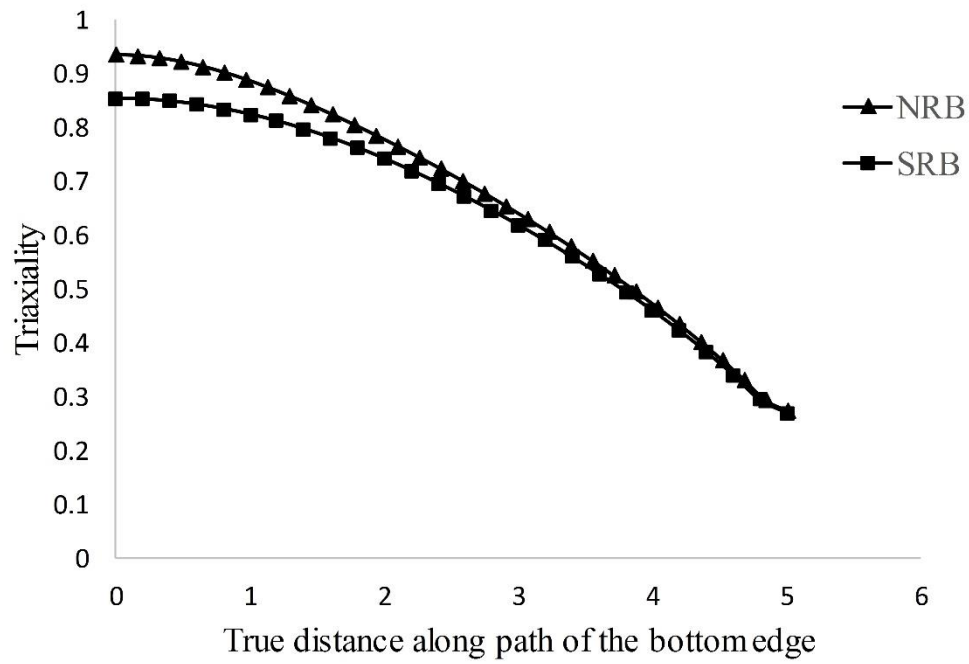


Figure 5.14 Stress triaxiality distribution along the bottom edge of the quarter of tensile test specimens

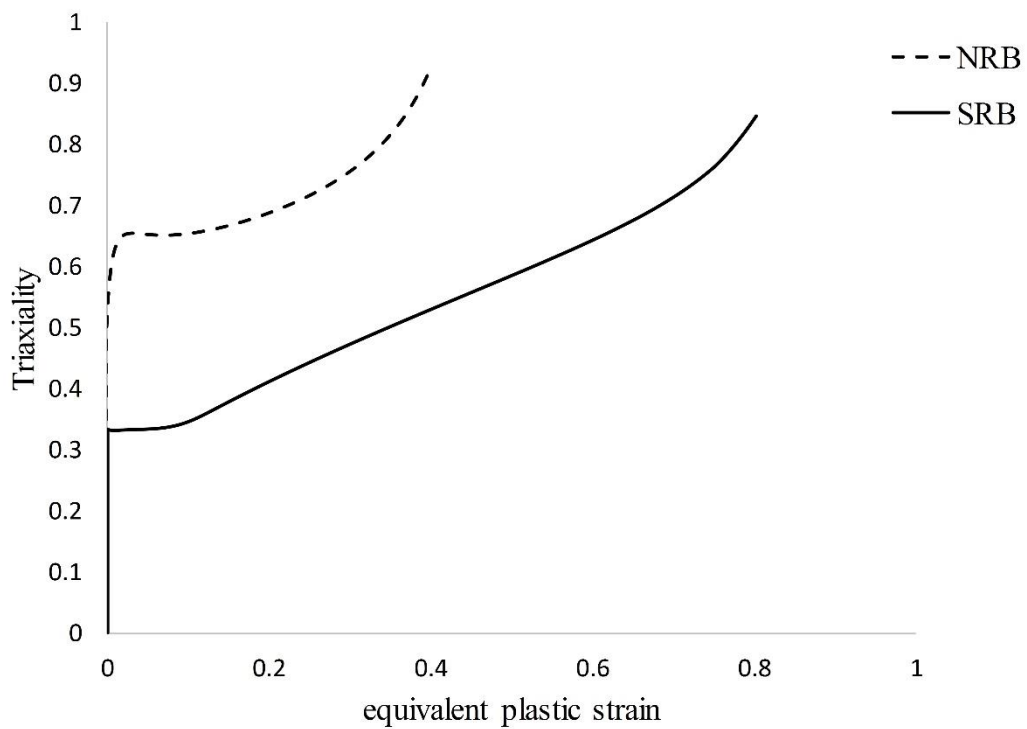


Figure 5.15 Stress triaxiality versus the equivalent plastic strain for the tensile test specimens

Due to the lack of experimental data to identify the initial porosity value, at an initial step, this parameter needs to be determined. According to the graphs presented in Figure 5.17, the simulation results from the value of $f_0 = 0.0005$ produced the closest material softening response compared to the experimental data and hence will be used for the phase-field-coupled simulations on this specimen. Following this, the phase-field related parameters are introduced as an input to the UEL module according to the reference, whereby the length scale is chosen $l_d = 1.3$ to be large enough according to the smallest element size.

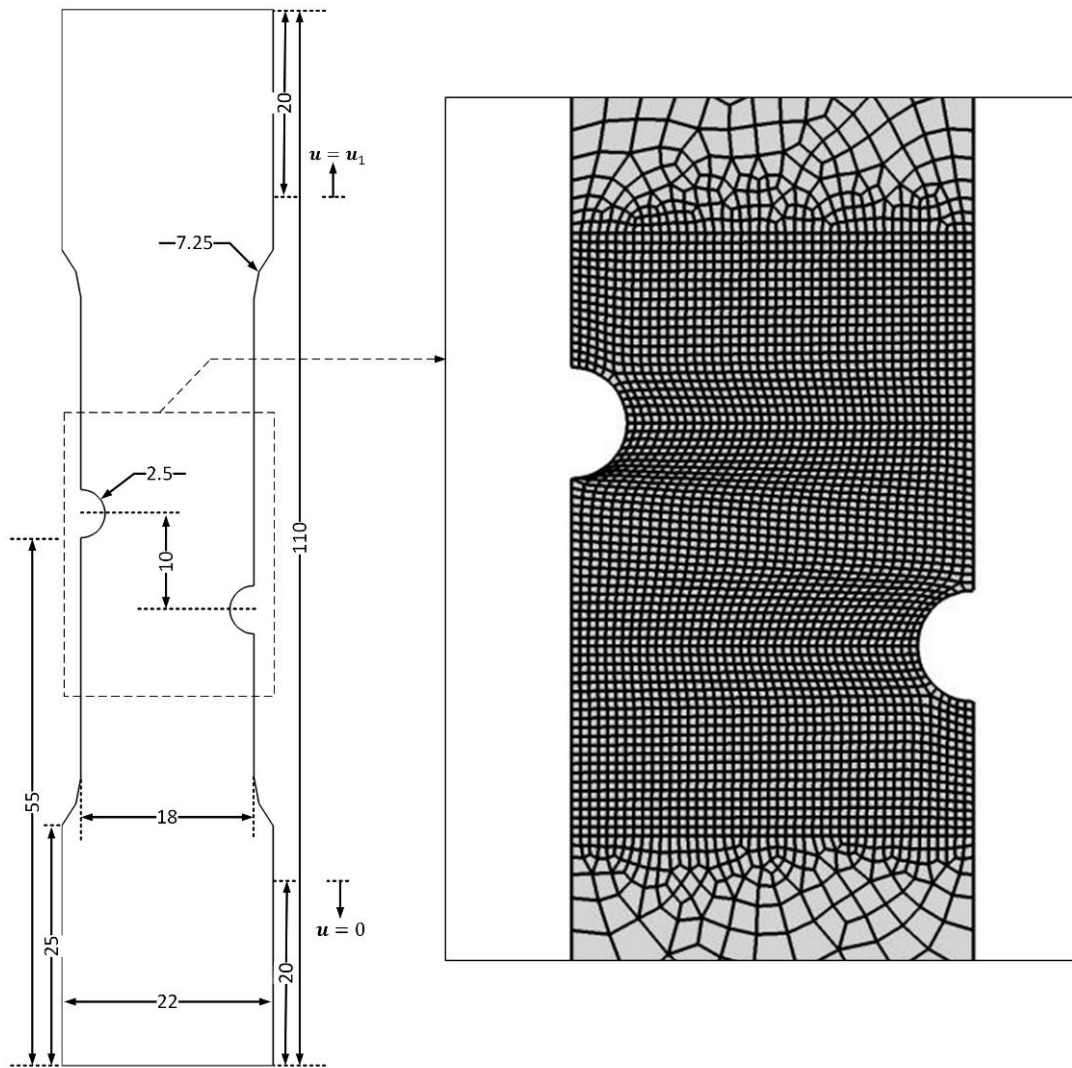


Figure 5.16 Asymmetrical notched specimen under tensile loading; geometry, boundary conditions and the mesh discretization of the critical region; dimensions are in *mm*

Using a unit fracture coefficient, the influence of the critical void volume fraction is represented in the plots of Figure 5.18, where the graph related to the value of $f_c = 0.02$ is in a closest agreement with the reference results. Using this value, the damage initiated once the plastic deformation starts and accumulates around the displacement of $u_1 = 0.82 \text{ mm}$ (point *A*). Then the void volume fraction reaches the critical value of f_c at $u_1 = 1.5 \text{ mm}$ (point *B*), where it is determined as the point of crack initiation and onset of the phase-field evolution process.

The damage profile is indicated via the contours of Figure 5.19, whereby the initiation, accumulation and critical damage states are spotted at the notch tips. The contour plots of Figure 5.20 demonstrate the evolution of the equivalent plastic strain and phase-field crack in the post-critical material deformation level ($f > f_c$). One can see the progression of the crack profile along the 45 degrees shear band, in which closely resembles the fracture patterns after tensile test in Figure 5.21 as was observed in [80]. The stress concentration is depicted through the contour plots of axial stress and the equivalent von Mises stress in Figure 5.22 at various stages of the failure in deformed configuration.

Table 5.2 Material parameters used for the numerical modelling of asymmetrical notched tensile test

Parameter	Symbol	Value	unit
Young's modulus	E	70.9	GPa
Poisson's ratio	ν	0.34	—
Hardening function	$R(\alpha)$	$113 - (113 - 135)e^{-24.5\alpha}$	MPa
RSL parameter	σ_1	75.0	MPa
RSL parameter	D	2.0	—
Initial porosity	f_0	0.0005	—
Critical porosity	f_c	0.02	—
Critical energy release rate	G_c	254.66	N/mm
length parameter	l_d	1.3	mm
Fracture coefficient	η	1.0	—

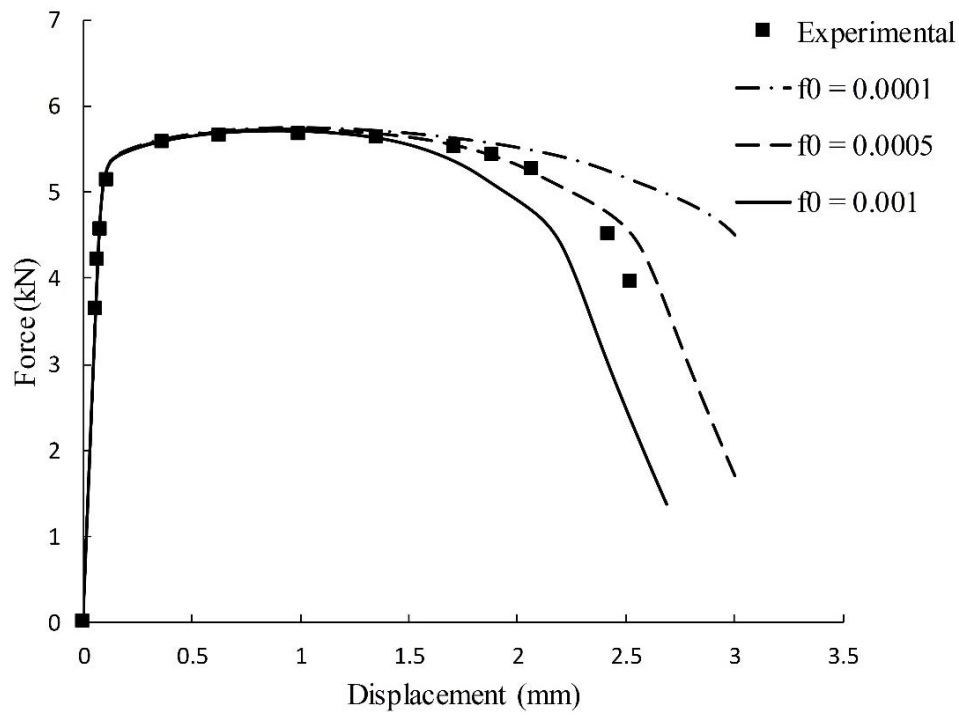


Figure 5.17 Force vs. vertical displacement using local Rousselier damage model for the asymmetrical notched specimen

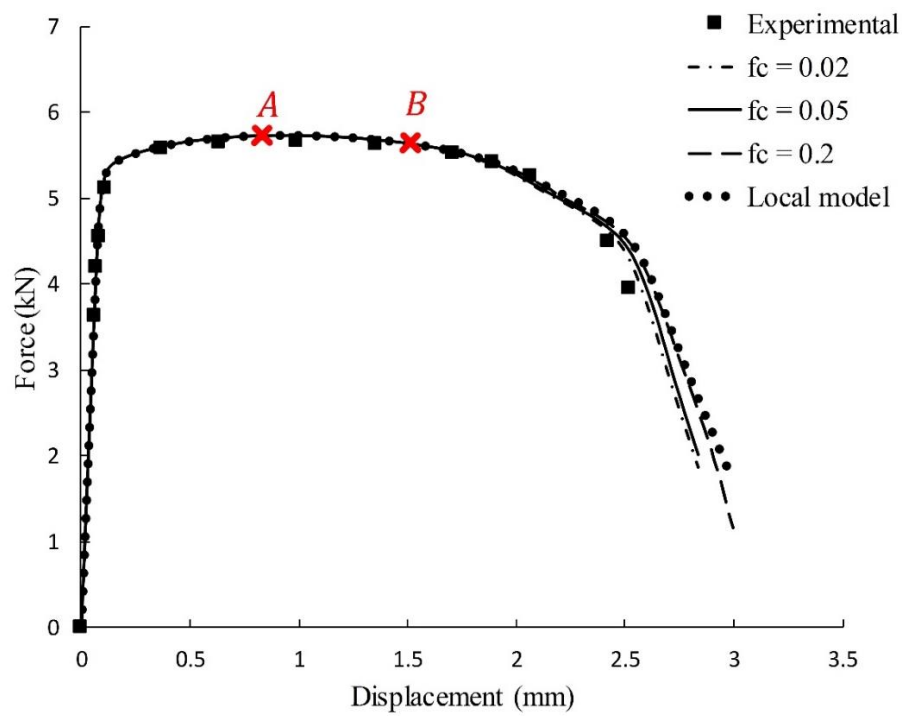


Figure 5.18 Force vs. vertical displacement using diffusive Rousselier damage model for the asymmetrical notched specimen

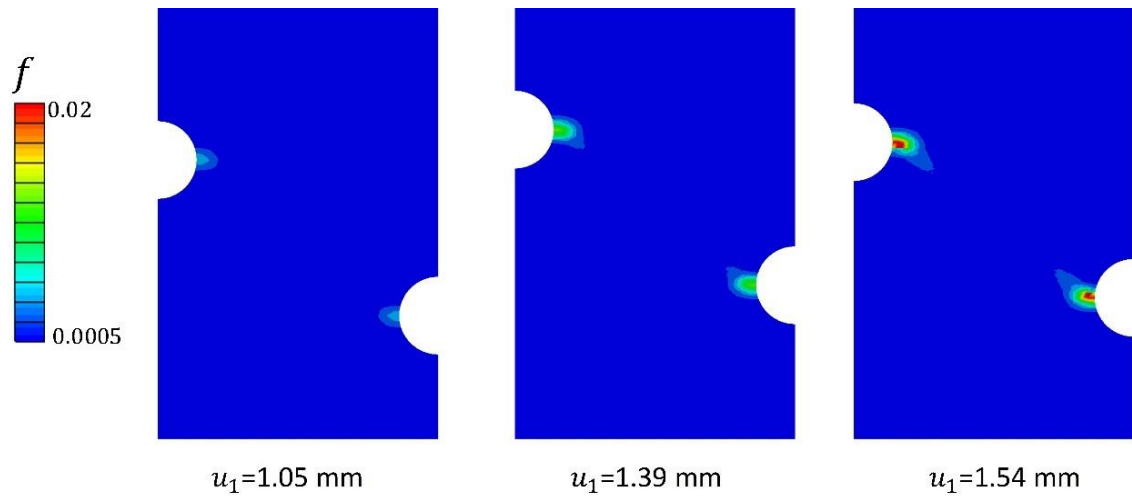


Figure 5.19 Damage profile in the asymmetrical notched specimen at different deformation levels

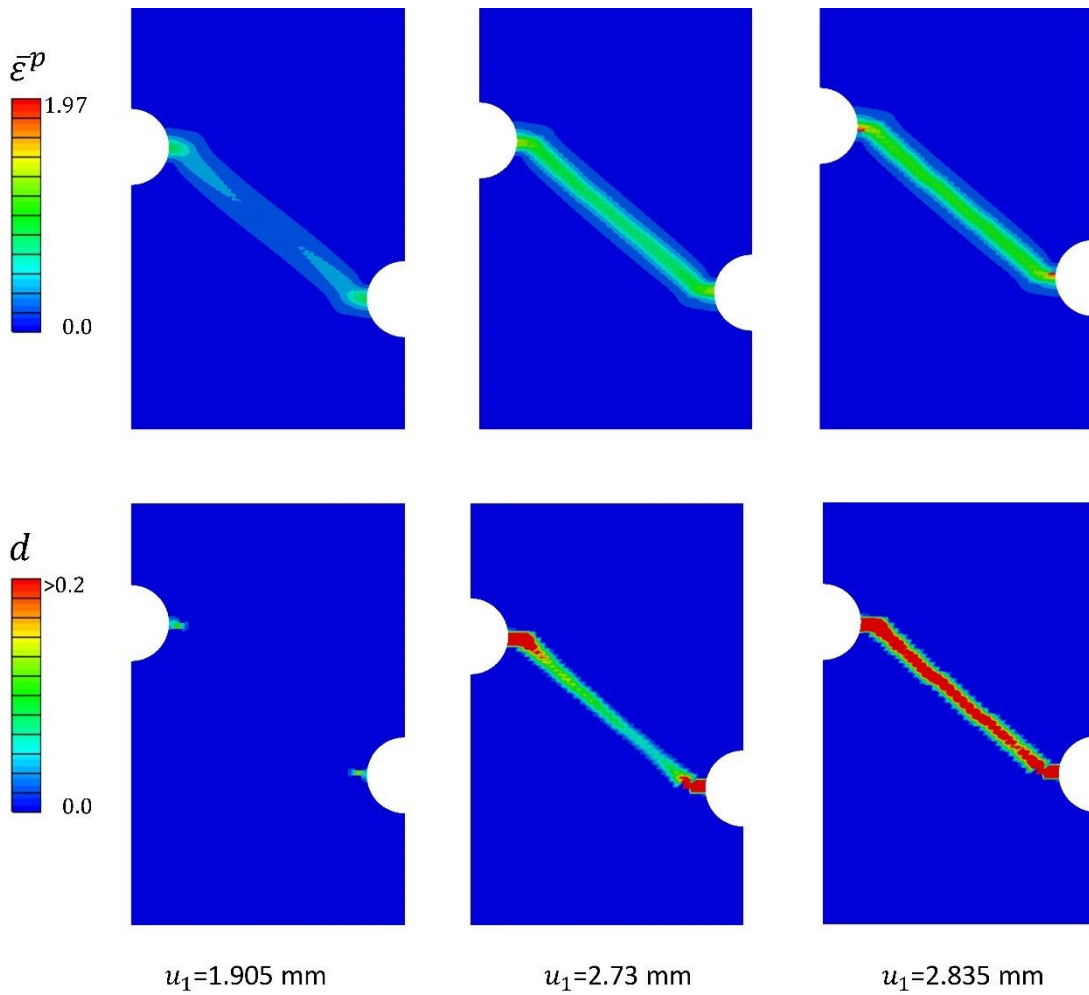


Figure 5.20 Evolution of equivalent plastic strain and phase-field crack in asymmetrical notched specimen in the post-critical deformation regime

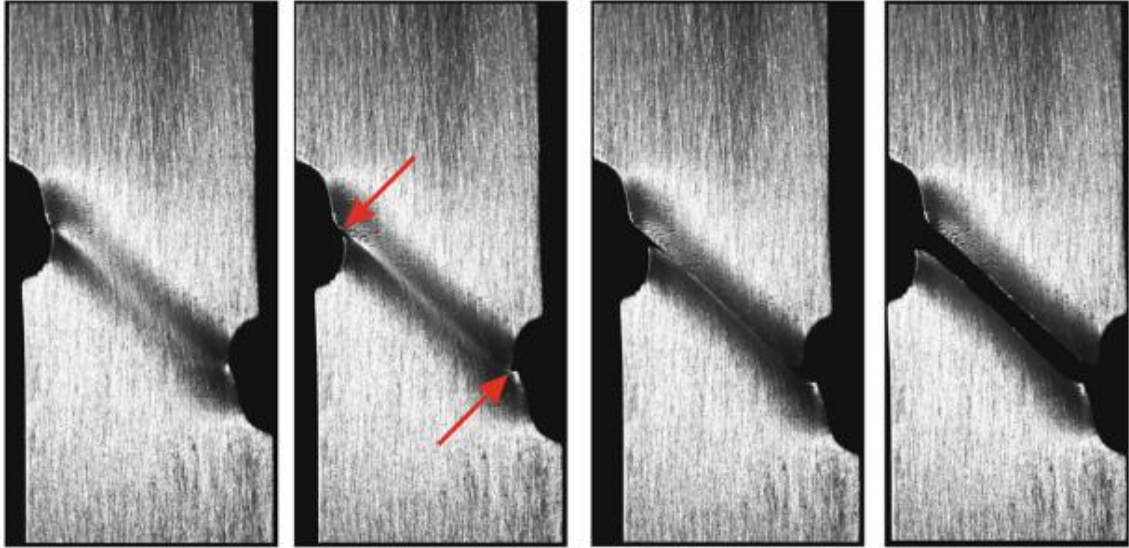


Figure 5.21 Experimental observation of fracture in asymmetrical notched specimen conducted in [80]

5.2.1 Shear sample

The material failure on a shear specimen is investigated in this section. The specimen shape is built using electrical discharge machining (EDM) to favour a shear localisation at the deformed area with low level of triaxiality, as addressed in [28,81]. The sample geometry and boundary conditions are depicted in Figure 5.23 (a). In the reference work, the specimen is cut from a sheet with thickness of 2.0 mm and this value is used in the numerical simulation herein.

The material parameters used in the numerical simulation are given in Table 5.3, which are based on Al5052P-H34 and in conformity with data provided in [81]. Observation through the scanning electron macroscopic images therein showed a highly elongated set of voids in the reference work, which confirms the shear fracture in the resisting area of the sample at the central region. The failed specimen after tensile loading is shown in Figure 5.23 (b).

The simulation is carried out using plane elements in order to circumvent the excessive computational effort of the 3D analysis. The specimen is discretised with the total number of 2658 plane stress quadrilateral elements with reduce integration method (CPS4R). As before, the mesh discretisation follows with adopting a larger population of elements in the area of fracture. The elastic properties and material hardening data are chosen

according to the reference data. By adopting a unit value for the fracture coefficient and length parameter of the value $l_d = 0.08 \text{ mm}$, the force-deflection results from the phase-field coupled model are plotted in Figure 5.24 for different values of the initial porosity against the experimental curve from [81], which clearly shows a better accordance of the results to the initial porosity of $f_0 = 0.0005$.

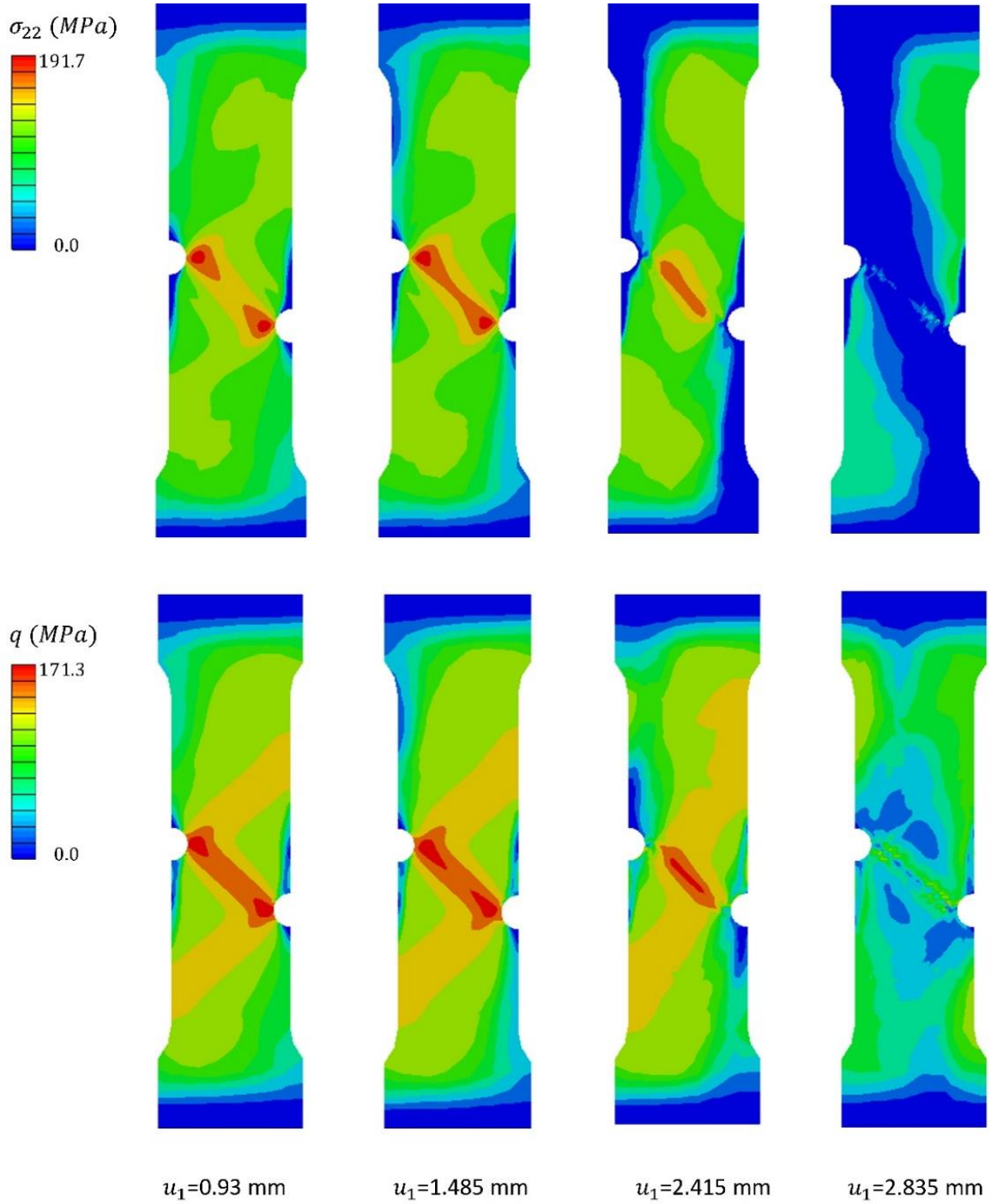


Figure 5.22 Contour plots of the axial and equivalent stresses at different deformation levels

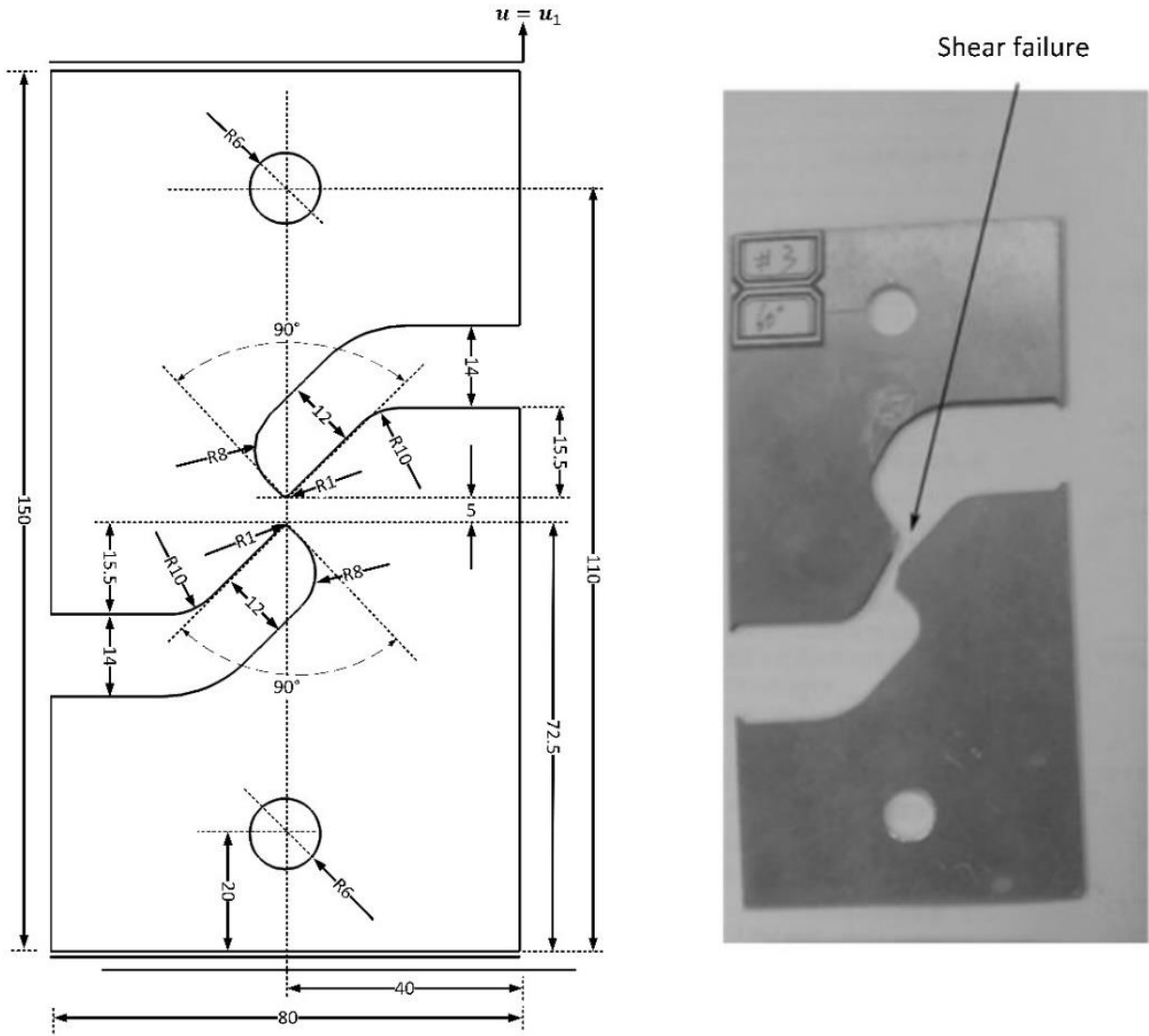


Figure 5.23 a) Geometry and boundary condition of the shear sample; b) fractured specimen [81]

The length scale sensitivity of the model is depicted in the graphs of Figure 5.25 for three values of the phase-field length parameter, $l_d = 0.03, 0.08, 0.12 \text{ mm}$. The smallest adopted value led to the least material softening in the post-critical state, as the consequence of the crack driving force decrease and hence the smaller degradation induced by the phase-field crack order parameter. Similar behaviour can be observed from the graphs related to different values of the fracture coefficient that are given in Figure 5.26, as the highest value $\eta = 2.0$ essentially yielded a steeper softening curve after the initiation of cracks.

The contour plots of the equivalent plastic strain and the phase-field parameter are illustrated in Figure 5.27. The final pattern of the propagated crack is in a good accordance with the failed specimen after the tensile test, which proves the predictive ability of the algorithm to handle shear-induced failure situations. This could be attributed to the characteristic of the yield surface that corresponds to the underlying damage model based on the Rousselier criterion.

Table 5.3 Material parameters used for the numerical modelling of shear sample

Parameter	Symbol	Value	unit
Young's modulus	E	62.735	GPa
Poisson's ratio	ν	0.33	—
Hardening function	$R(\alpha)$	$264.5 - (264.5 - 182.8)e^{-24.5\alpha}$	MPa
RSL parameter	σ_1	177.0	MPa
RSL parameter	D	2.0	—
Initial porosity	f_0	0.0002, 0.0005, 0.001	—
Critical porosity	f_c	0.05	—
Critical energy release rate	\mathcal{G}_c	10.0	N/mm
length parameter	l_d	0.03, 0.08, 0.12	mm
Fracture coefficient	η	1.0	—

The stress distribution in different material deformation levels are demonstrated in the contour plots of the equivalent von Mises and axial stresses in Figure 5.28, which show the stress concentration in the central region of the specimen.

5.3 Nonlocal gradient regularisation analysis

The primary numerical results to verify the performance of the nonlocal gradient approach in damage regularisation are presented in this section. The finite element implementation in this part is based on the solution strategy in the context of thermomechanical problem that was discussed in section 4.1.3. Following the discussions therein, the efficiency and simplicity of the numerical implementation of the temperature-displacement problem could be beneficial in such gradient regularisation methods, whereby the heat conduction equation is made compatible with the diffusive equation in

gradient problem and the calculations of the stresses and internal variables are primarily followed in the material point level in the UMAT module.

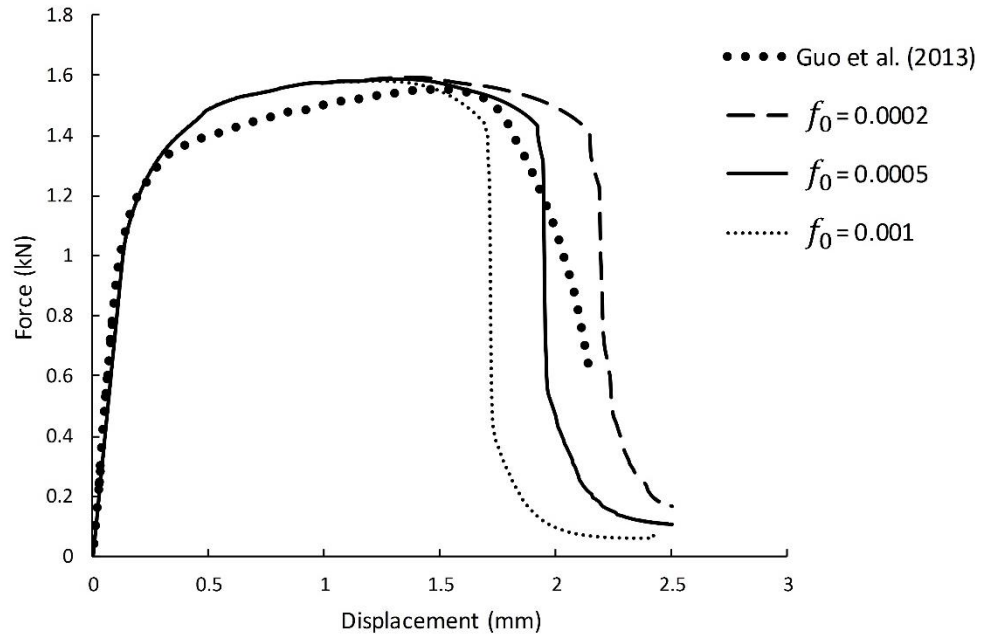


Figure 5.24 Force vs. vertical displacement using diffusive Rousselier damage model for the shear specimen

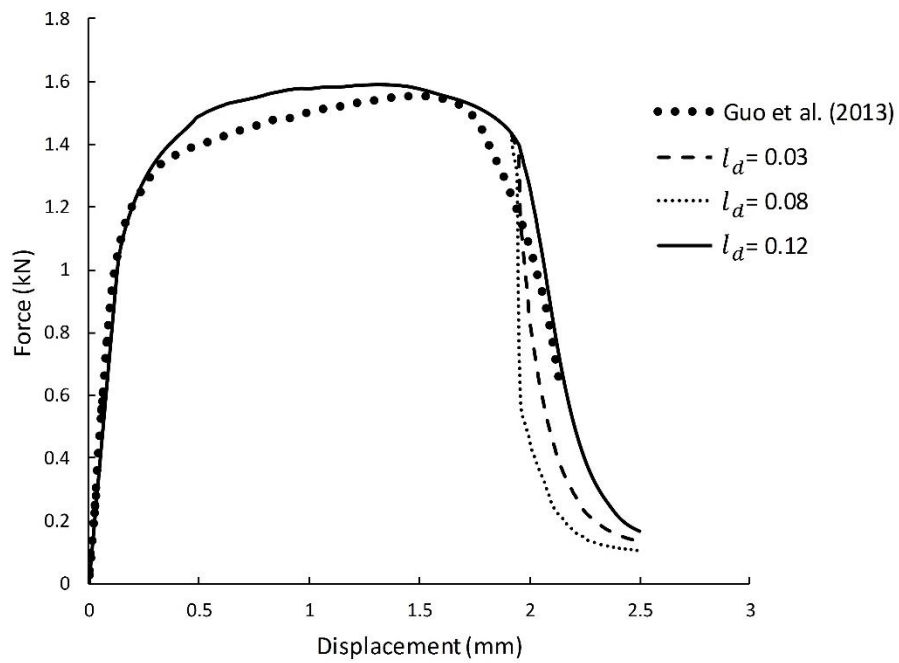


Figure 5.25 Length scale sensitivity of the diffusive Rousselier damage model for the shear specimen

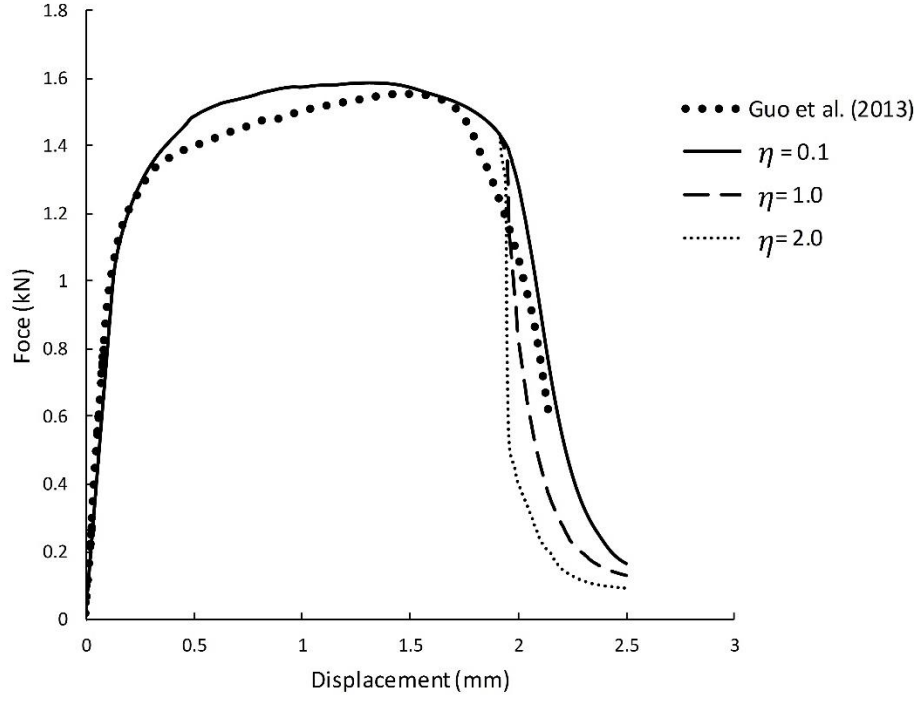


Figure 5.26 Influence of the fracture coefficient on the global response of the diffusive Rousselier damage model for the shear specimen

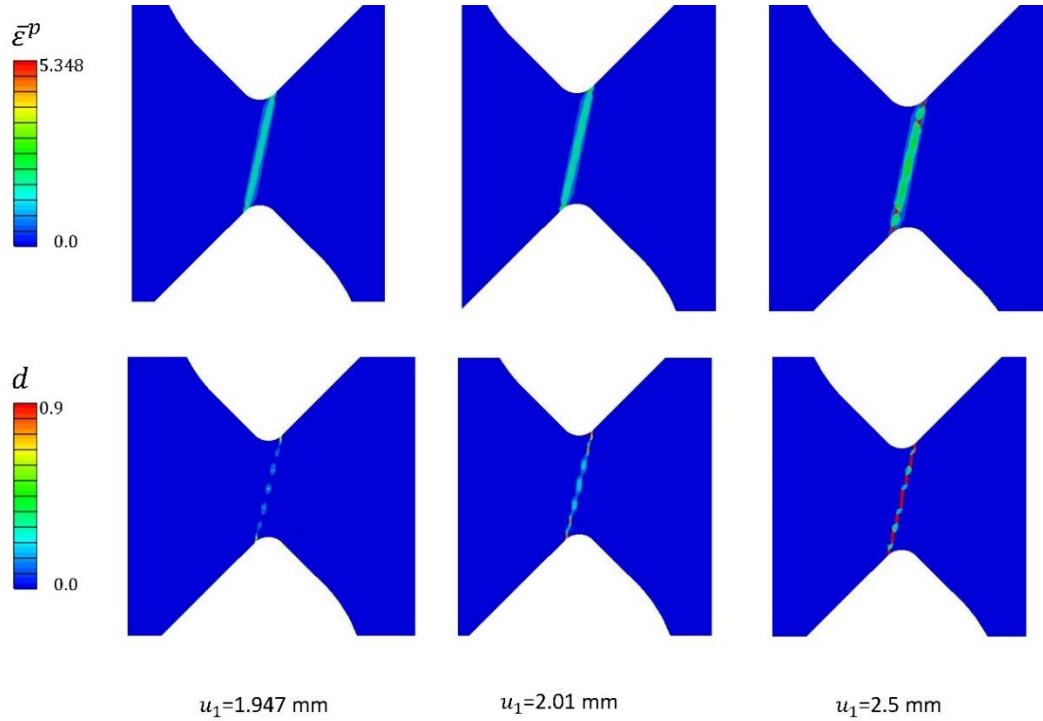


Figure 5.27 Contours of the equivalent plastic strain and phase-field profiles in the material post-critical regime for the shear specimen at different deformation levels

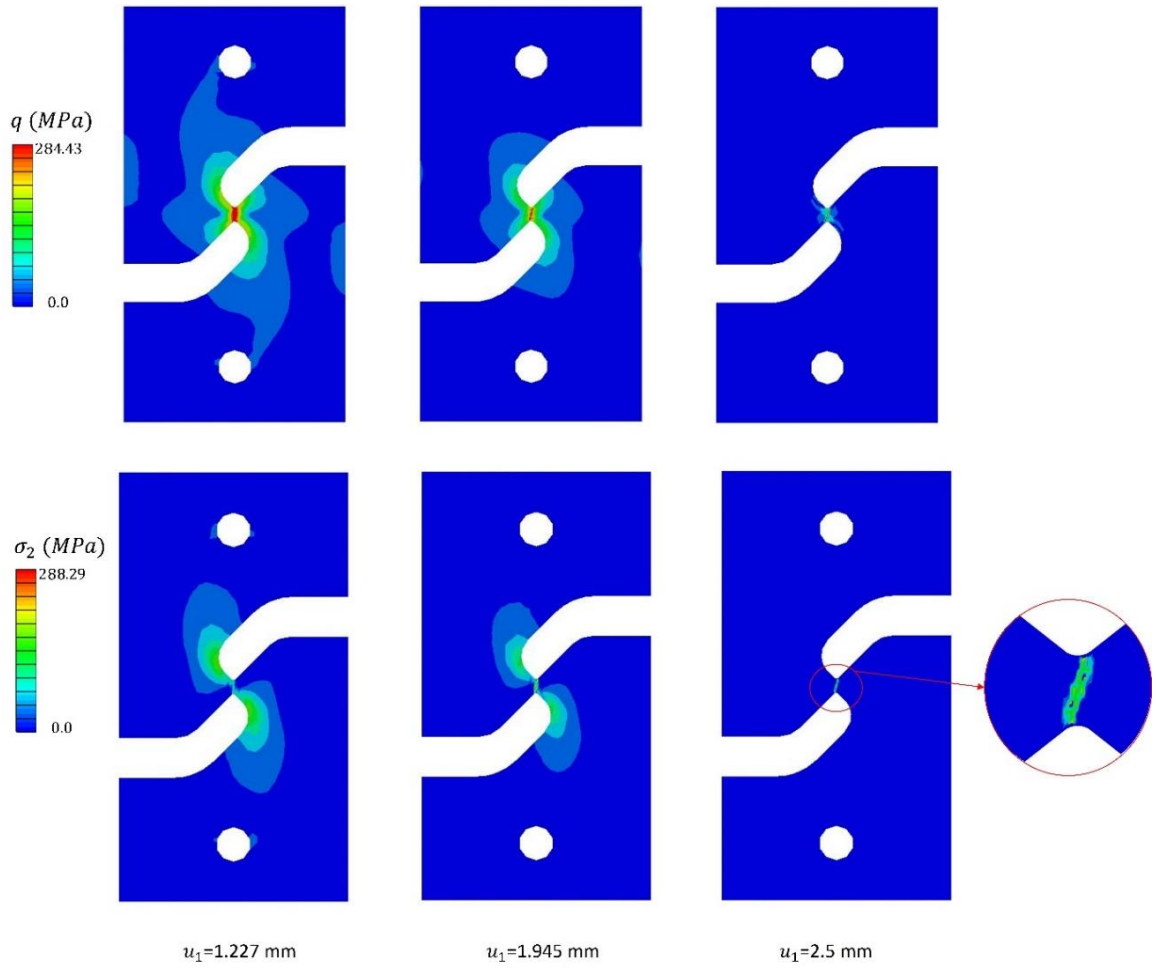


Figure 5.28 Contours of the equivalent stress and the axial stress in the material post-critical regime for the shear specimen at different deformation levels

Numerical simulations in the present section are carried out based on the local Lemaitre ductile damage model that is coded in the material routine. The nonlocal Helmholtz type equation is defined in the HETVAL routine as the conductivity is set to the length parameter in the gradient problem and the coupling of the mechanical problem with the nonlocal field is performed based the modified constitutive model described in section 4.1.2.

5.3.1 Flat grooved tensile specimen

To show the numerical capabilities in reducing the influence of the mesh topology on the material global response, a flat grooved tensile specimen with the notch radius of 2.58 mm and out-of-plane thickness of 50 mm is considered following the numerical

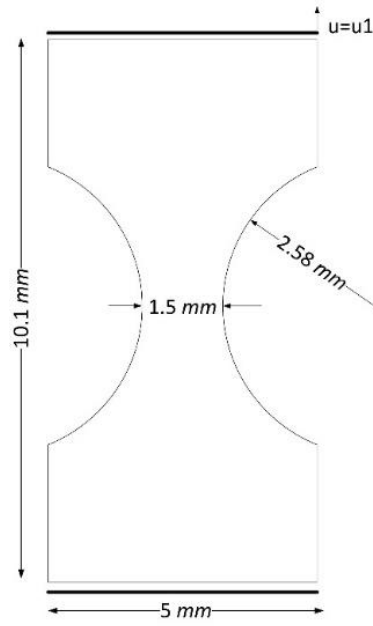
analysis that was discussed in [82]. The in-plane sample geometry is represented in Figure 5.29 (a). Only one quarter of the specimen is modelled using proper symmetries. Three different structured mesh densities with the size of $b_h = 0.25 \text{ mm}$, $b_h = 0.125 \text{ mm}$ and $b_h = 0.094 \text{ mm}$ are adopted in numerical simulations which are depicted in Figure 5.29 (b-d). The element type is of quadrilateral thermal plane strain elements (CPE4T) is used. The material parameters used in the simulations are given in Table 5.4.

Assuming the imposed displacement of $u_1 = 0.2 \text{ mm}$ and setting the value for the conductivity keyword in ABAQUS input file to the length parameter value, the simulations are carried out on all meshes. The local and nonlocal damage profiles are illustrated in Figure 5.30. The localisation of the damage occurs at the center of the specimen and it evolves along a 45° shear band. In the plots nonlocal damage field is found to be more broadened than the local counterpart, whereby expectedly the numerical simulation yields lower values for nonlocal damage field than the local ones. The resolution of the mesh dependency can be better revealed in the graphs of Figure 5.31 and Figure 5.32.

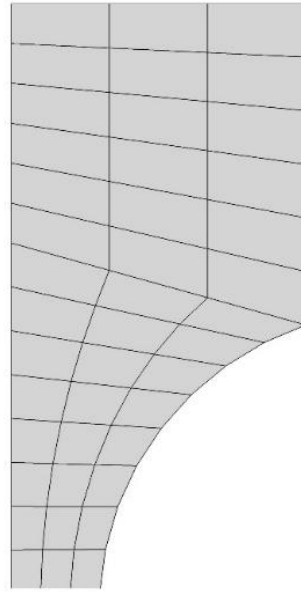
Clearly the performance of the adopted nonlocal algorithm could be approved where a less discrepancy found between the graphs correspond to the nonlocal damage model than those related to the local one. The force versus deflection curves are plotted against the numerical results in [83] where authors investigated the performance of the integral-type nonlocal damage methodology.

Table 5.4 Material parameters used for the numerical modelling of flat grooved sample

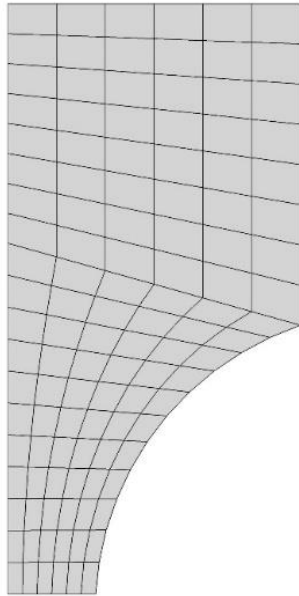
Parameter	Symbol	Value	unit
Young's modulus	E	210.	GPa
Poisson's ratio	ν	0.3	—
Hardening function	$R(\alpha)$	$700 + 300(\alpha)^{0.3}$	MPa
LM parameter	r_1	3.0	MPa
LM parameter	r_2	1.0	—
Nonlocal length parameter	l_N	0.1	mm



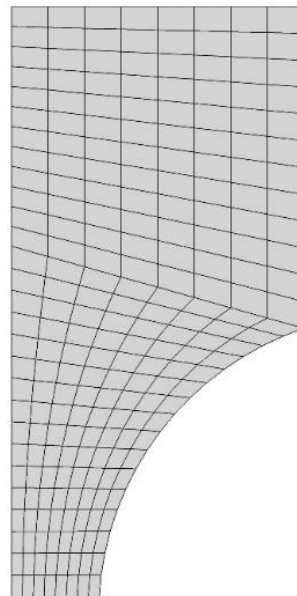
(a)



(b)



(c)



(d)

Figure 5.29 a) Flat-grooved sample geometry and discretisation of the quarter of sample with element edge size of b) $b_h = 0.25 \text{ mm}$, c) $b_h = 0.125 \text{ mm}$ and d) $b_h = 0.094 \text{ mm}$

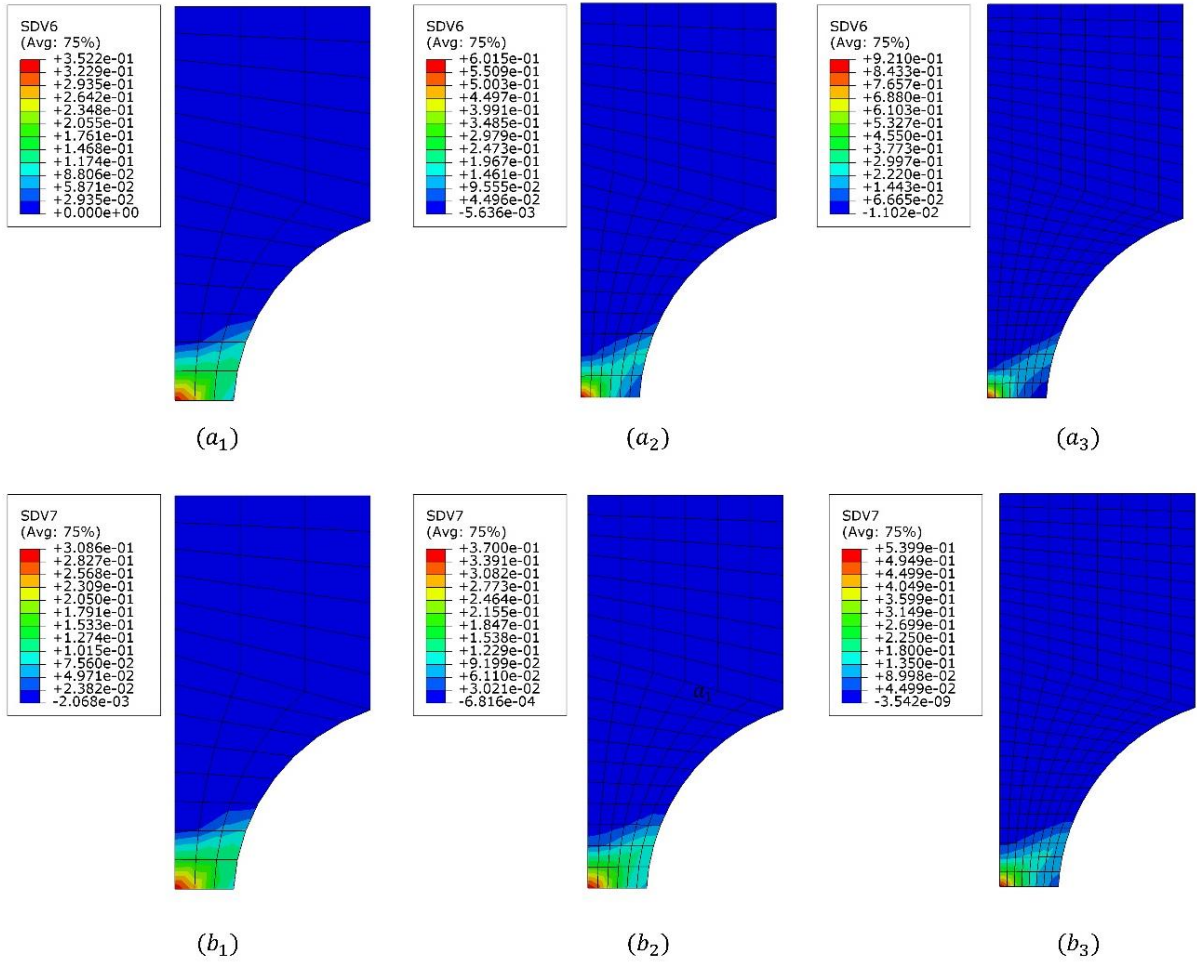


Figure 5.30 Evolution of the internal damage represented via the $(a_1 - a_3)$ local field and $(b_1 - b_3)$ nonlocal field

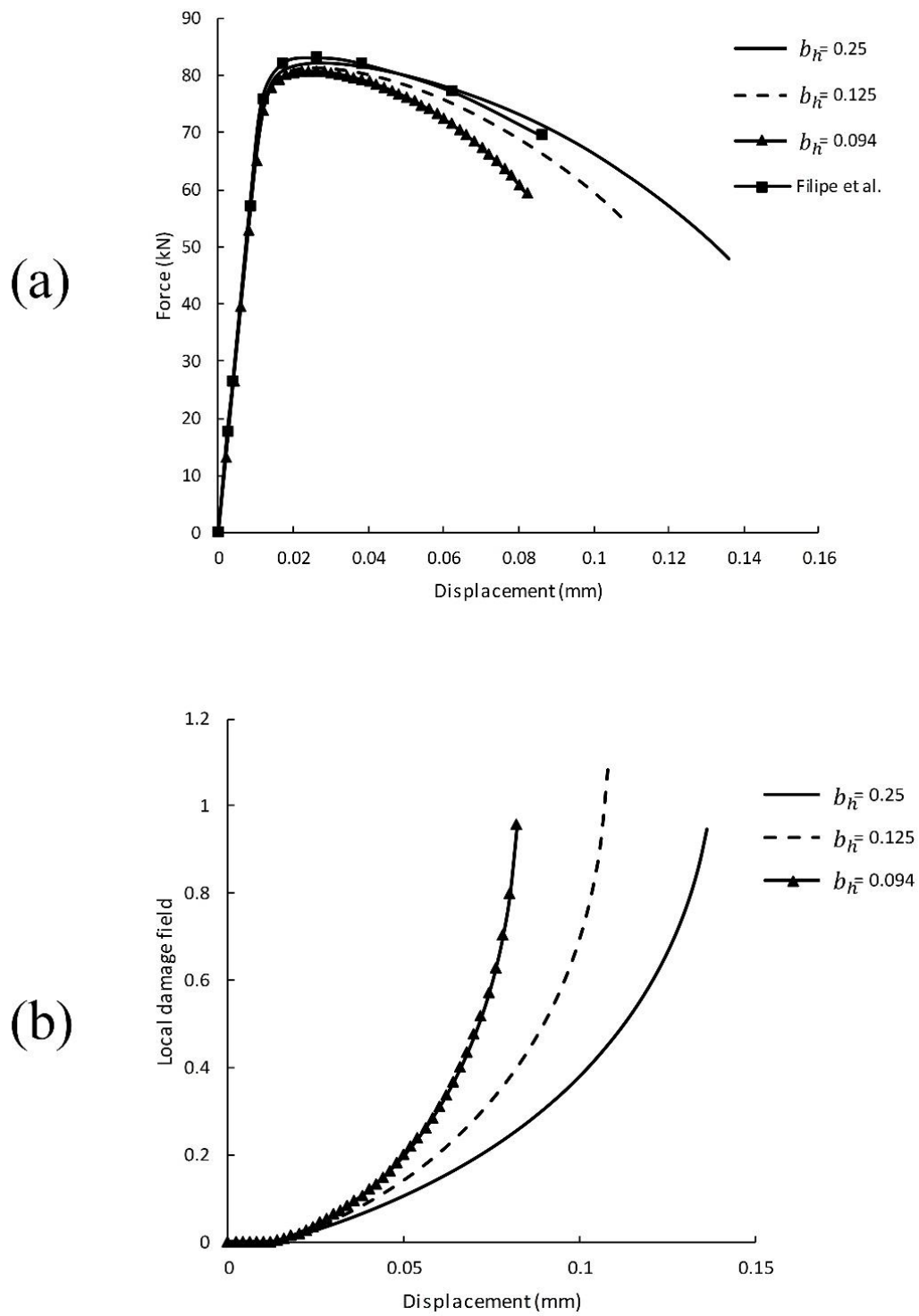


Figure 5.31 a) Force versus deflection obtained from the local damage model and b) evolution of the local damage field

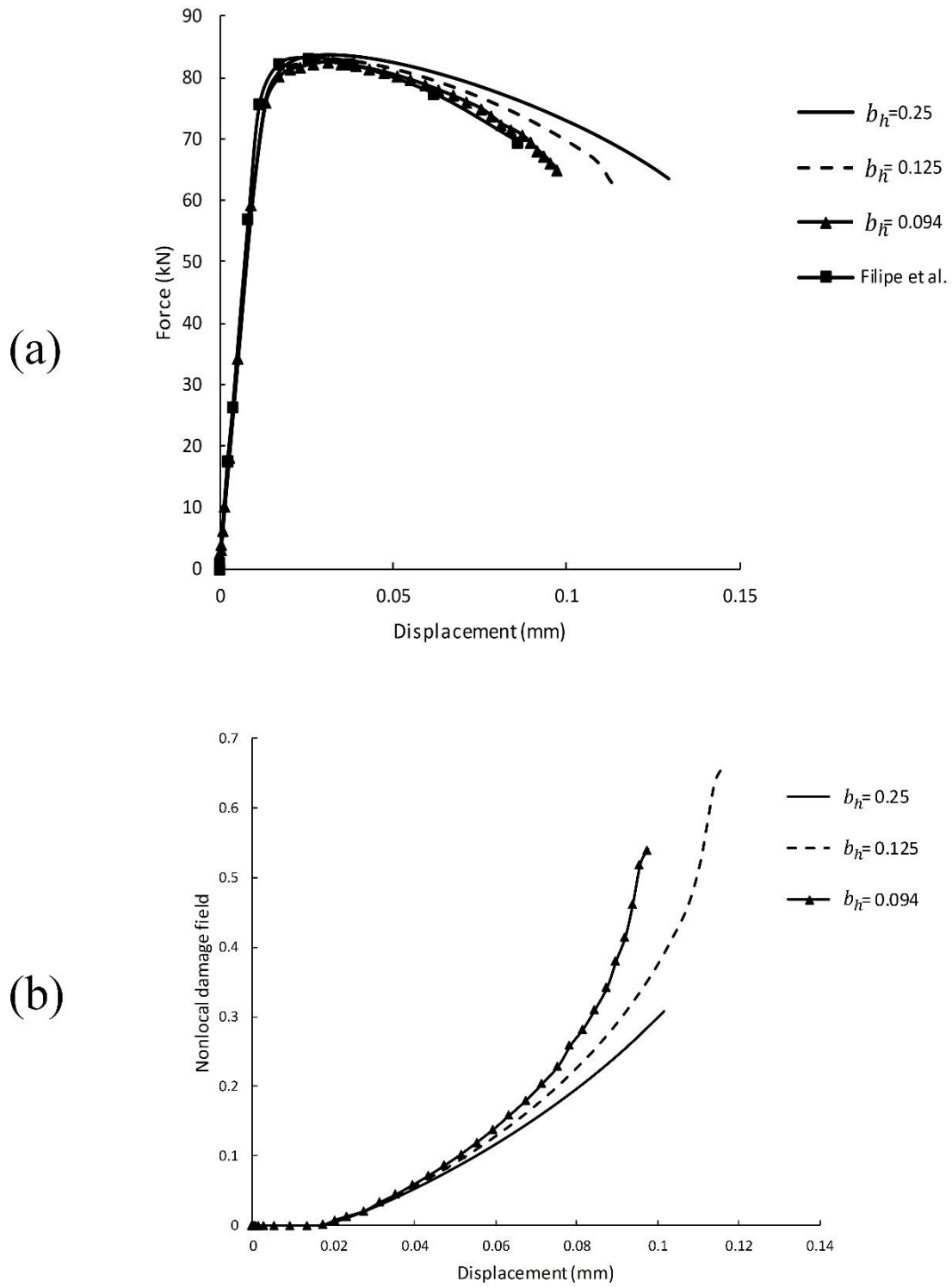


Figure 5.32 *a)* Force versus deflection obtained from the nonlocal gradient damage model and *b)* evolution of the nonlocal damage field

6.Experimental and numerical modelling of fracture in additively manufactured steel components

Through the course of last few years, the application of the laser-based manufacturing processes became more significant in wide range of industrial sectors, including automotive, biomedical, aerospace, among others. To date, one of the most regarded forms of these processes namely the additive manufacturing (AM) or commonly known as the three-dimensional (3D) printing, has marked a significant influence in production of metal components with better mechanical properties and improved thermal stability than the conventional metal alloys. However, the issues arisen from the material development or processing perspectives have led to an extensive scientific research in this area in recent years.

Directed energy deposition (DED) is addressed in the literature as one of the efficient laser-based additive manufacturing processes. Its origin can be traced back to the welding technology where the material deposition is conducted by flowing an inert gas over the melt pool. The fabrication of the metallic components using this process is performed by deposition of feedstock, in the form of either powder or wire, directly into a molten pool, at which the 3D component is built layer by layer. The powder-fed DED was first introduced by the Sandia National Laboratories back in 1995 and it became more popular since the advent of laser engineer net shaping (LENS) technology, where the parts can be directly produced from the computer aided design (CAD) software. The superiority of this technology over the other laser-based manufacturing processes is linked to its fast stacking speed and ability to build materials with high strength and melting points.

Nevertheless, some limitations are still felt at the industrial scale regarding laser-based manufactured processes in what concerns process parameters and their effect on the

microstructure and consequently on the overall behaviour of the parts produced. In particular, mechanical properties and microstructural study on stainless steel 316L laser-based manufactured components were addressed in [84–87]. Properties of directed energy deposition processed materials were analysed [88], showing the influence of laser power, powder flow rate, scan speed and molten pool size on the morphology of porosity and anisotropy, where authors found significant effect of the location and orientation of the fabricated samples on the mechanical properties and fracture behaviour after tensile testing. In another effort, among many other research activities, the influence of the building direction on the mechanical properties, microstructure and machinability of the AM processed stainless steel 316L was addressed in [89].

At this stage, it is also important to assess if existing models used for ductile failure in metals can be used for additive manufactured components. In that direction, an assessment is attempted in this work, having in mind that a similar pattern of internal degradation in ductile metallic materials is observed, characterised by a sequence of growth and coalescence of micro-voids that precedes macro-crack propagation and final material rupture.

In this section, the microstructural study of SS 316L alloys fabricated with DED manufacturing process is studied. The main body of research in this section is two-fold. The experimental aspects of the manufacturing process are briefly discussed in the first part of the chapter which has been totally performed at COMTES FHT a.s. research organisation in Czech Republic. This part includes concise explanation of the DED fabrication process for the steel components herein and discussion on fractographic images taken from the failed tensile samples.

The second part is devoted to the numerical analysis on the manufactured samples for tensile testing with emphasis on the porosity growth and accumulation of damage upon loading the structure. After determination of material model parameters, including initial void volume fraction using inverse FEM and generalised mixture rule (GMR) approach, the coupled phase-field fracture model that was discussed in chapter 4 is utilised due to its verified predictive ability to address failure of ductile materials. Several discussions are made by concentrating on the microstructural aspects of the processed components and the performance of the finite element algorithm in the post-critical material regime.

6.1. Experimental procedure

DED manufacturing process is classified under seven AM technologies, which according to ASTM F2792-12a, defined as a process in which a “focused thermal energy is used to fuse materials by melting as they are deposited”. The heat source is typically either a laser, electron beam or plasma arc to produce a melt pool on a substrate, at which the feedstock in the form of powder (powder-fed) or wire (wire-fed) is injected through the nozzle on the molten pool. Through the material deposition, the components are fused layer by layer. The possibility to obtain heterogeneous processed components, due to the flexibility in changing materials' compositions at each layer by simply adjusting feeding materials and process parameters, is one of the pivotal features of DED manufacturing processes [90,91]. The microstructure of DED fabricated components is in general highly dense with minimum flaws and high cooling rate due to solidification [90]. The thickness of the deposited layer of material may vary between 0.1 to a few millimeters in thickness [92].

In this study, Powder Blown (PB) DED process is utilised for fabrication of the metallic components fed from an austenitic AISI 316L stainless steel in powder form. A scanning electron microscopy (SEM) image of the powder used is shown in Figure 6.1. A deposition system, printer InssTek MX600 3D was employed to fabricate a cube with dimension $35\text{ mm} \times 35\text{ mm} \times 35\text{ mm}$, at which the miniature tensile specimens were excised. A fiber laser beam with the diameter of $800\text{ }\mu\text{m}$ which carries Argon gas as the shielding inert gas is used. The fabrication parameters that are used in the DED procedure are specified in Table 6.1. Chemical composition through the weight percentage of the substances (wt%) and thermo-physical properties of initial powder are given in Table 6.2 and Table 6.3, respectively.

In order to build the specimens layer by layer, metal fabrication procedure follows the patterns (orientations) that are depicted in Figure 6.2. The miniature-sized specimens were machined by wire electrical discharge machining (EDM) from the cube. A total of 15 specimens in 3 orientations (5 specimens per orientation) as shown in Figure 6.3 were extracted. To distinguish the samples based on their distance from the cube surface, henceforth, the samples are named for each orientation as $T1i$, $T2i$ and $T3i$, where $i = 1, 5$.

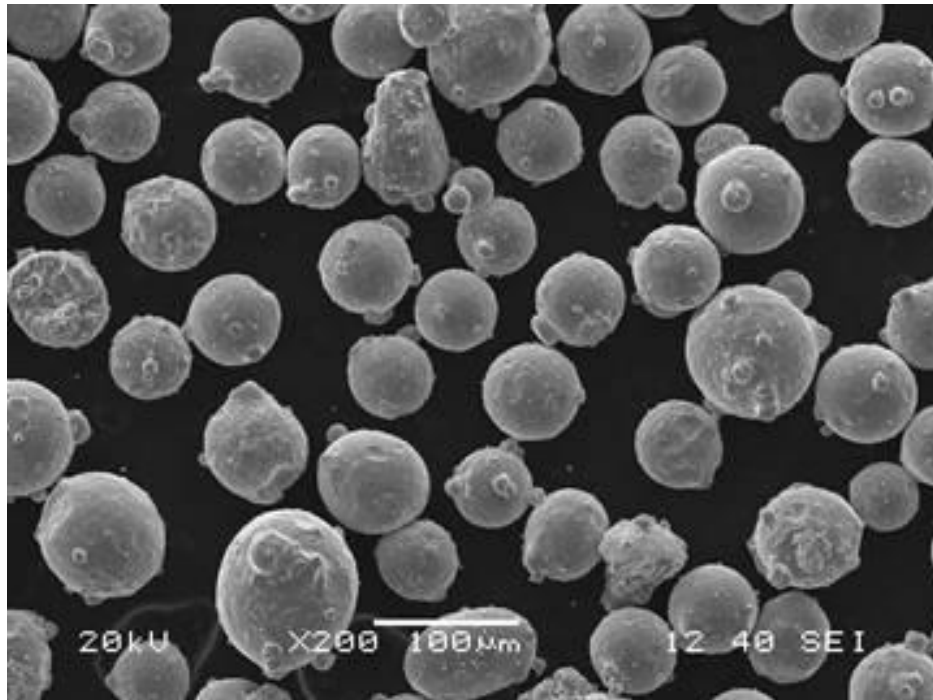


Figure 6.1 SEM image of stainless steel 316L powder feed material used in DED process

Table 6.1 Fabrication parameters employed in the DED process

Parameters	Value	Unit
Laser spot diameter	0.8	<i>mm</i>
Laser power	417	<i>W</i>
Scanning speed	14.166	<i>mm/s</i>
Layer thickness	0.25	<i>mm</i>
Track overlap	0.5	<i>mm</i>
Powder feeding rate	3	<i>g/s</i>

Table 6.2 Chemical Composition of stainless steel 316L

Element	C	Cr	Cu	Mn	Mo	N	Ni	P	S	Si
(wt %)	0.009	16.82	0.31	1.74	2.08	0.029	10.26	0.03	0.024	0.27

Table 6.3 Thermo-physical properties of stainless steel 316L initial powder

Parameters	Value	Unit
Liquidus temperature	1723	K
Solidus temperature	1553	K
Density	7966	Kg/m^3
Latent heat	256400	J/Kg

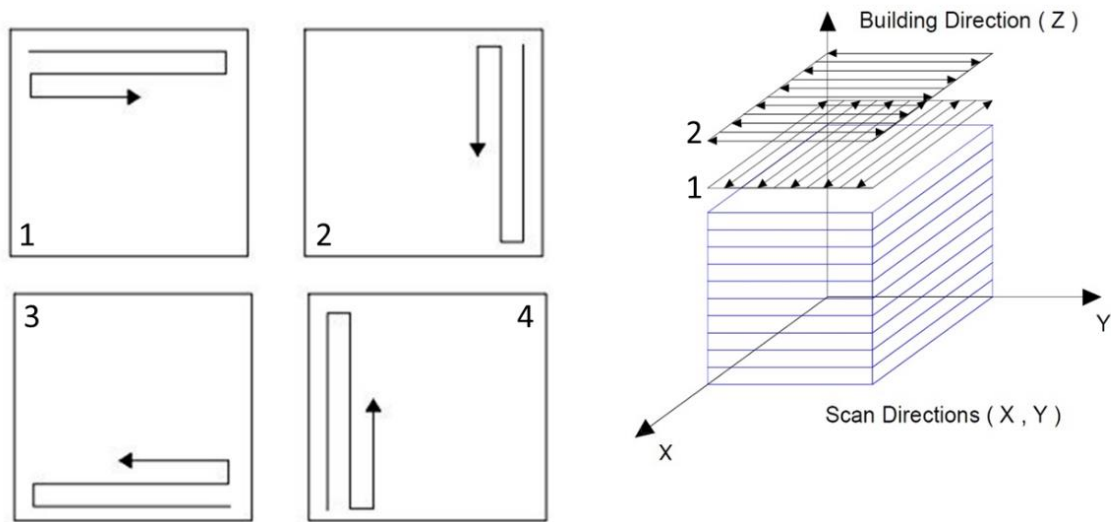


Figure 6.2 Metal filling patterns during the fabrication process

Schematic of the coupon fabrication based on the building direction is depicted in Figure 6.4. One can see for the building direction of 0° for sample groups $T2i$ and $T3i$, the loading direction is parallel to the sliced layer in contrast to the building direction of 90° conducted for samples $T1i$, where the loading is applied perpendicular to the layers. This property has been revealed to be influential in tensile properties such as ultimate tensile strength or elongation [89].

The geometry of the tensile test sample is depicted in Figure 6.5. Strain is measured by an optical extensometer which is fixed to the specimen and the gauge length in all samples was considered 11 mm. The failed specimens after the tests are represented in Figure 6.6, which shows the fracture within the gauge length range for all the samples, considering some discrepancy in fracture locations. This can be related to the diverse patterns of pre-existing voids which will be addressed in the next section.

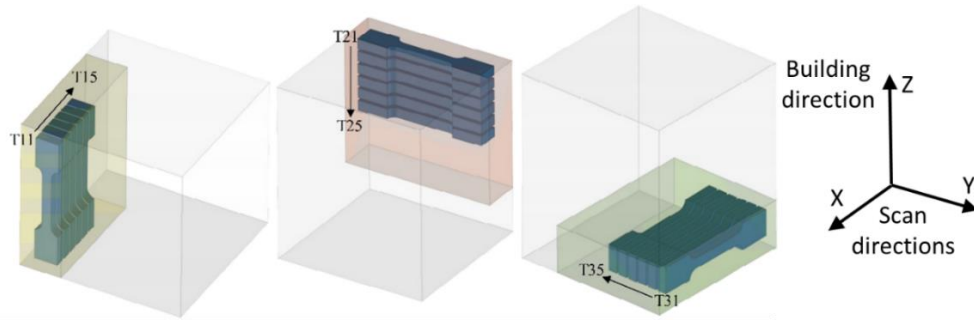


Figure 6.3 DED-processed 316L cubic component with test specimens in three orientations

The material engineering stress-strain data for all samples are illustrated in Figure 6.7. A higher yield and ultimate tensile strength can be observed for sample groups $T2i$ and $T3i$ that are fabricated perpendicular to the loading direction, i.e. building direction of 0° , than the $T1i$ sample group. The latter group with the building direction of 90° exhibits lower yield and ultimate tensile strength and highest value of elongation than the other two groups. The mechanical properties of the samples are given in Table 6.5.

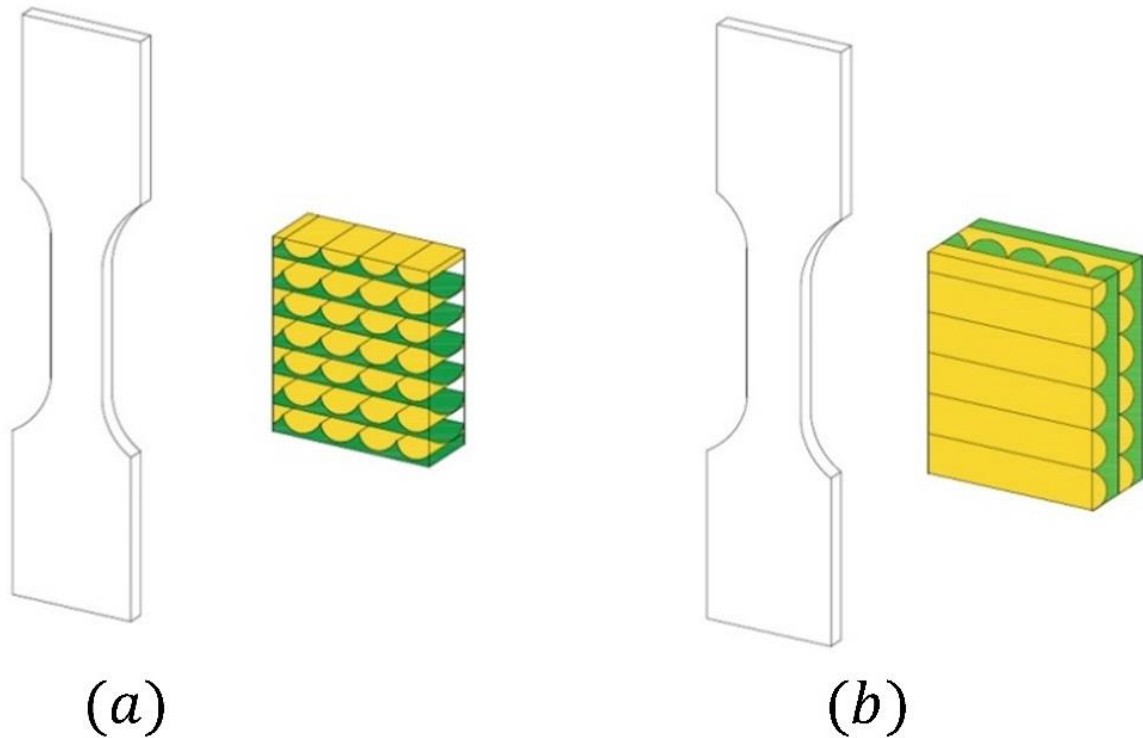


Figure 6.4 Schematic of the building directions during the fabrication process for a) sample group $T1i$ and b) sample groups $T2i$ and $T3i$

6.1.1. Microstructural observations

Micro-void defects or porosities have been found as one of the common causes of degraded mechanical properties in additively manufactured samples, which were studied in different types of powder including steel alloys, for instance in [87,93–95]. Interlayer and intralayer defects are two common types of porosity that may occur respectively due to an insufficient power delivery during the melting process, which leads to lack of fusion and gas entrapment throughout the deposition process (vaporization porosity), in which spherical gas pores transfer to the as-fabricated component. While the former porosity type can be controlled by adjusting the process parameters, the latter is typically associated with the inert shielding gas, herein the Argon gas, and is distributed in random locations within the fabricated component.

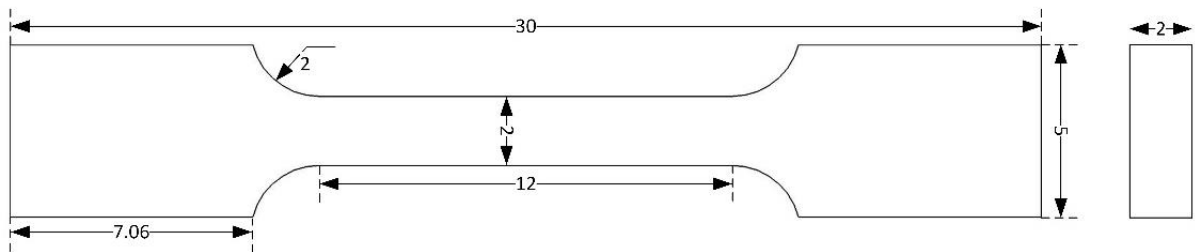


Figure 6.5 Geometry of the tensile test samples (dimensions in *mm*)



Figure 6.6 Deformed and fractured tensile test specimens

Table 6.4 Mechanical properties of the samples

Specimen	Temp. °C	a ₀ mm	b ₀ mm	a _u mm	b _u mm	R _{p0,2} MPa	R _m MPa	A _g %	A ₅ %	Z %
T11	23	2,00	2,00	1,08	1,10	453,3	657,4	43,4	63,9	70,1
T12	23	2,00	2,00	1,18	1,11	452,0	650,5	45,2	62,7	67,3
T13	23	2,00	1,99	1,08	1,05	461,4	654,1	44,7	65,9	71,3
T14	23	2,01	2,00	1,02	1,11	467,6	652,3	45,1	67,2	72,0
T15	23	2,00	2,00	0,98	1,02	460,1	654,3	45,3	64,8	75,1
Average						458,9	653,7	44,7	64,9	71,2
St. Dev.						6,3	2,6	0,8	1,8	2,9
T21	23	2,00	2,01	1,22	1,07	457,2	654,3	37,7	52,5	67,5
T22	23	2,00	2,00	1,06	1,02	475,3	666,6	35,9	53,4	72,9
T23	23	1,99	2,00	1,07	1,17	464,9	671,2	36,0	53,0	68,5
T24	23	2,00	1,99	1,10	0,98	468,4	671,9	35,0	52,1	73,0
T25	23	1,99	2,01	1,14	1,12	485,2	672,0	34,9	50,9	68,2
Average						470,2	667,2	35,9	52,4	70,0
St. Dev.						10,6	7,5	1,1	0,9	2,7
T31	23	2,00	2,00	1,08	1,14	464,2	669,6	34,5	51,3	69,1
T32	23	1,99	2,00	1,18	1,24	492,1	674,5	35,4	50,7	63,0
T33	23	2,00	2,00	1,03	1,08	507,9	677,9	35,9	56,1	72,3
T34	23	1,99	1,99	1,10	1,22	523,1	686,8	34,4	53,7	66,0
T35	23	2,00	2,00	0,95	1,04	514,1	678,3	33,9	56,8	75,5
Average						500,3	677,4	34,8	53,7	69,2
St. Dev.						23,1	6,3	0,8	2,8	5,0

The global energy density (GED) is referred to as a useful measure that establishes a link between the interlayer and intralayer porosities in DED processes. This parameter is quantified through a combination of several process parameters [95,96]. Figure 6.8 schematically represents the link between the GED and porosity in DED manufacturing processes.

Regarding the micromechanical observations herein, the test specimens were hot mounted in resin under heat and high pressure, and polished porosity analysis by microscopy. Microscopic images were captured, stitched, and analyzed using a NIKON ECLIPSE MA200 in SW NIS-elements AR as is illustrated in Figure 6.9.

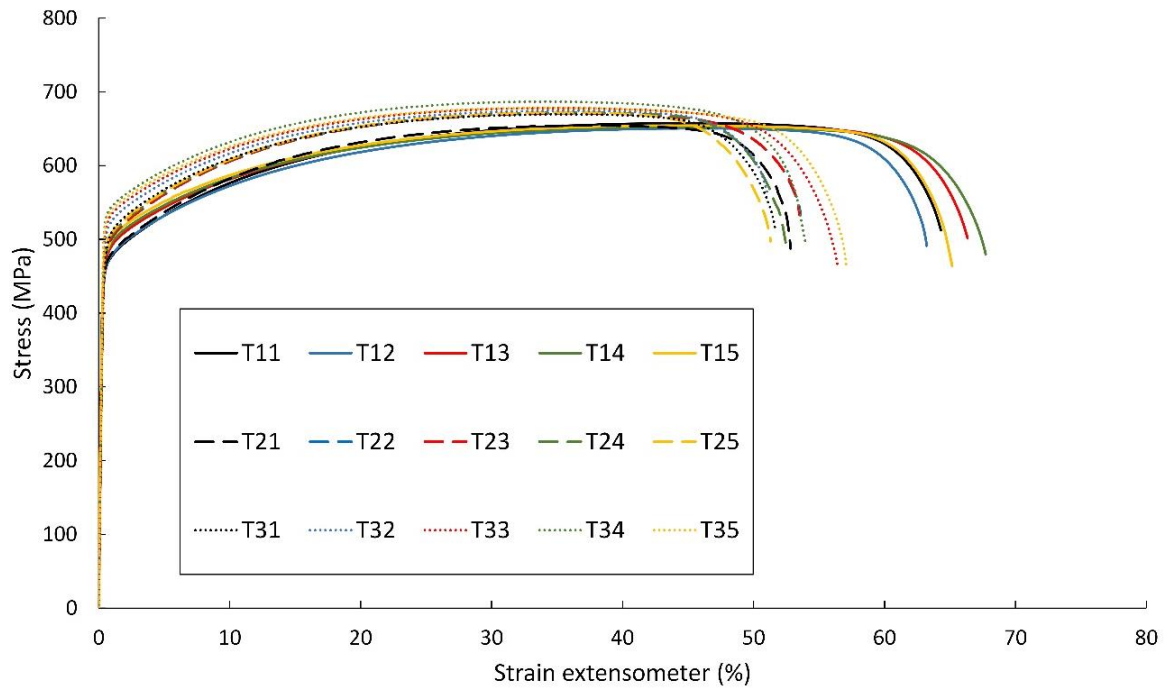


Figure 6.7 The engineering stress versus strain graphs taken from tensile samples

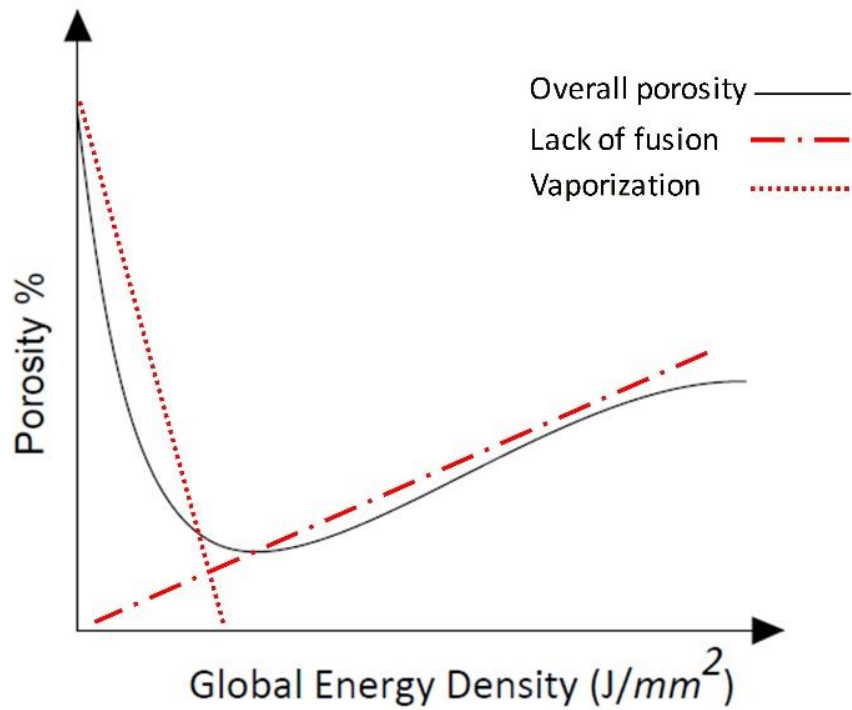


Figure 6.8 Relationship between the porosity and global energy density function in DED processes

After the tests, the fracture surfaces were observed through the post-mortem micrographs on all broken specimens. Using fractographic images from, for example, T11 sample that is depicted in Figure 6.10 (a, b), where one can see cup-cone like fracture pattern, where the crack initiation region is spotted around the center of the sample as shown by the red dotted circle. The SEM micrograph of this region is demonstrated in Figure 6.10 (c), exhibits small dimples that are distributed all over the fracture surface. Following this image, a distribution of equiaxed dimples are observed which reveals the porosity growth under high level of triaxiality that could be linked to the mode I fracture in the central region of the sample.

6.2. Numerical analysis of fracture in DED processed samples

The numerical study in this section follows the coupled phase-field ductile fracture material model that was discussed in section 4.3. The numerical implementation of the coupled multi-field finite element problem is based on the staggered solution method described in section 4.2.4 where the finite element solution is obtained using ABAQUS package.

In what follows, the simulation results correspond to the tensile test samples of *T11* and *T31* are of the main concern. Due to the comparison purposes and brevity, the sample group of *T2i* is left out from the numerical simulation, as they are fabricated on the same building direction as sample group *T3i* based on Figure 6.4.

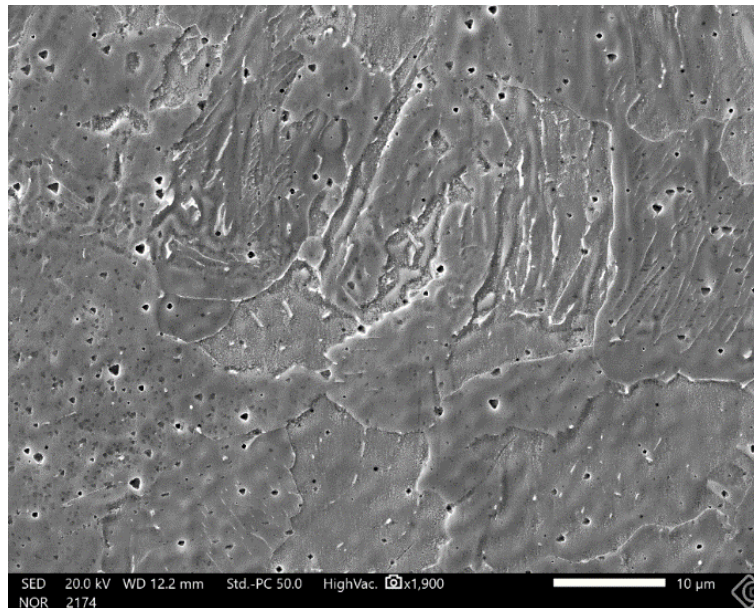


Figure 6.9 Porosity observation in the fabricated samples before the test

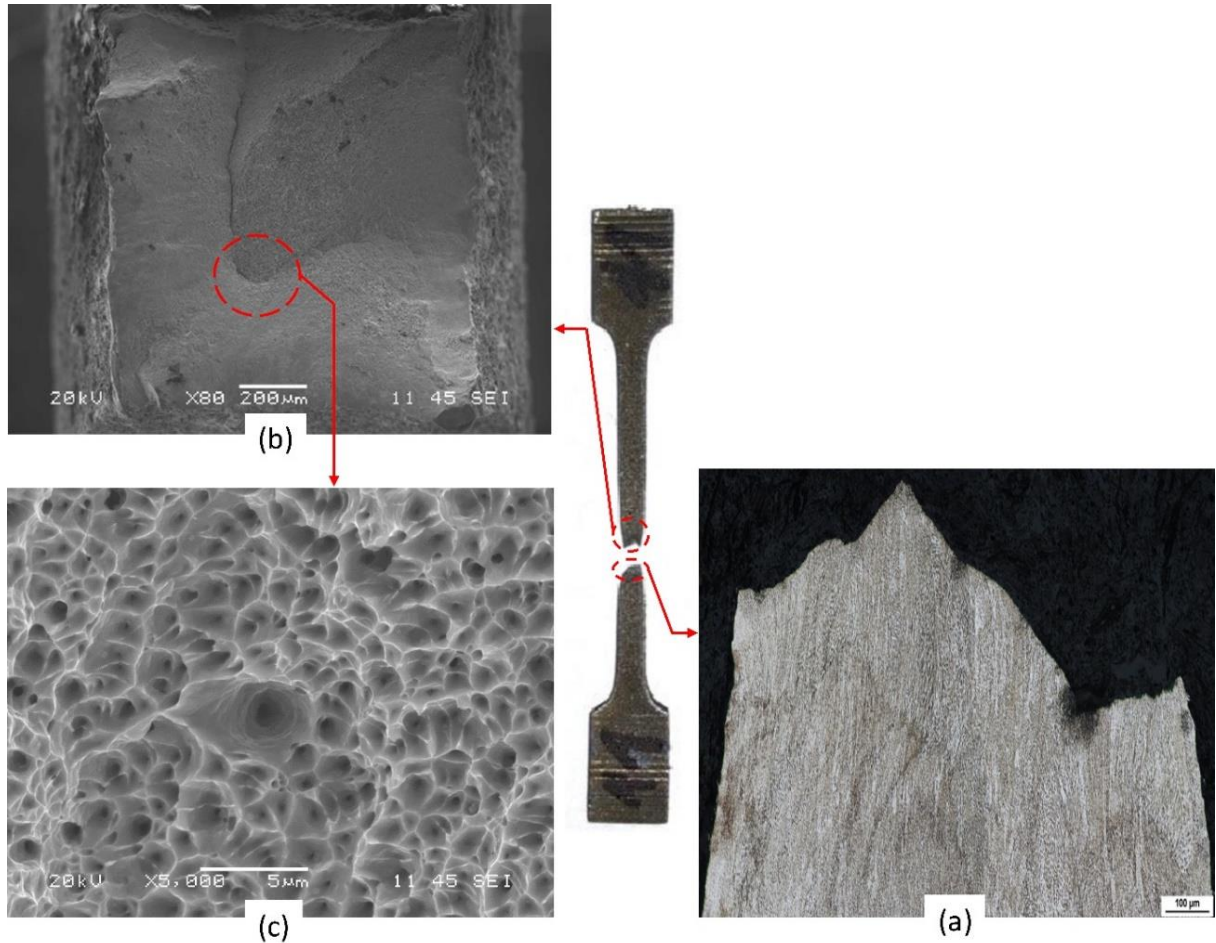


Figure 6.10 (a, b) Fracture surfaces, (c) Identified defects dominated by crack initiation

6.2.1. Determination of the material parameters

Following the Rousselier flow potential expressed in section 3.2.3, a set of parameters, corresponding to the material hardening and softening, needs to be determined. The material hardening data is characterised based on the engineering stress-strain laboratory data, as was given in Figure 6.7. In this regard, the true strain and true stress for the samples T11 and T31 are calculated using the relations $\varepsilon_T = (1 + \varepsilon_N)$ and $\sigma_T = \sigma_N(1 + \varepsilon_N)$ where ε_N and σ_N are, respectively, the engineering strain and stress. Using this information, the effective plastic strain can be computed by the following relation:

$$\alpha = \varepsilon_T - \sigma_T/E \quad (6.1)$$

The desired hardening data suitable for ABAQUS implementation could be obtained by fitting the hardening curve with the graph of the true stress versus plastic strain making use of the following Ludwik's law:

$$R(\alpha) = \sigma_y + \bar{K}\alpha^n \quad (6.2)$$

where σ_y is the material yield stress from the provided experimental data, α is the internal hardening variable, i.e. the equivalent plastic strain, K is the strength coefficient and n is the hardening exponent.

Based on [97], the Rousselier model parameters are set to $D = 2.0$ and $\sigma_1 = \frac{2\sigma_y}{3}$ for all numerical simulations. Therefore, $\sigma_1 = 302.2 \text{ MPa}$ and $\sigma_1 = 309.5 \text{ MPa}$ are used in the simulation of T11 and T31, respectively. The set of the material parameters for both samples are given in Table 6.5

The simulation is carried out with 2D four-node quadrilateral plane stress elements formulated by reduced integration method. A higher mesh density with unstructured distribution is used in the central area prone to the cracking, with the element edge size $b_h = 0.08 \text{ mm}$, amounting to 3622 total number of the elements. The boundary condition settings are considered as follows: the bottom edge of the specimen is fixed and a displacement-driven boundary condition is applied at the top edge of the sample as its horizontal movement is prohibited.

The initial value of void volume fraction can be associated with the shape, size or distance of the voids. In this study, the numerical model without the influence of the phase-field diffusion is used to calibrate initial porosity value by comparing against the laboratory data.

Considering the gauge length of 11 mm for all tensile test experimentations, variation of the force-displacement is compared with the experimental data from T11 and T31 samples in Figure 6.11 and Figure 6.12, respectively. Clearly, a faster growth rate of the voids can be observed from the graphs of the evolution of void volume fraction for higher value of their corresponding initial value, which is also addressed in [98]. As expected, the lowest displacement at fracture is obtained for $f_0 = 0.001$ and $f_0 = 0.0009$ from samples T11 and T31, respectively. Following this, the values of $f_0 = 0.00025$ and $f_0 = 0.0009$ are in the closest agreement with the experimental test data for T11 and T31 specimens, respectively. Therefore, these values will be used in the following phase-field model simulations.

Table 6.5 Material parameters for the DED-processed AISI 316L steel alloy used for the numerical modelling of tensile test on T11 and T31 specimens

	Parameter	Symbol	Value	unit
	Young's modulus	E	192.0	GPa
	Poisson's ratio	ν	0.33	—
T11	Model parameter	σ_1	302.2	MPa
	Model parameter	D	2.0	—
	Initial porosity	f_0	0.00025, 0.0005, 0.001	—
	Initial yield	σ_y	453.85	MPa
	Strength coefficient	\bar{K}	1078	MPa
	Hardening exponent	n	0.81	
T31	Initial yield	σ_y	464.2	MPa
	Strength coefficient	\bar{K}	1036	MPa
	Hardening exponent	n	0.76	
	Model parameter	σ_1	309.5	MPa
	Model parameter	D	2.0	—
	Initial porosity	f_0	0.00025, 0.0005, 0.0009	—

6.2.2. An approach to identify initial porosity values using Generalised Mixture Rule (GMR)

In this section, an approach based on the generalised mixture rule (GMR) is utilised to determine and verify the values of initial void volume fraction that were obtained in the section 6.2.1. The GMR provides a rigorous, unified expression that relates the poly-phase composite structures and the respective component properties, which has been addressed in solid materials [99], rocks [100] and in DED manufactured components [88], among others. Within the scope of the present work, this approach could reflect the link between the overall mechanical property of the produced components and the volume fraction of the voids in each sample, considering the porous structure as a special case of a two-phase composite. The GMR expression for a two-phase composite is given by:

$$M_c^J = (1 - V_w)M_s^J + V_wM_w^J \quad (6.3)$$

where M_c is the mechanical property of the overall composite that is written as a monotonically, increasing function of the V_w as the volume of the porous phase and M_s and M_w , which are respectively the mechanical properties of the nonporous (bulk) phase and the second phase (herein air). The J fractal parameter contains information about the microstructure of the component and is controlled by shape, size and distribution, i.e. connectivity and continuity of the pores. It has been found that the J -factor parameter value is dependent on the microstructural description of the cavity pores, and thus mechanical properties which makes it an intriguing topic of research in material design. Interested readers are referred to [99] for more discussions on this matter.

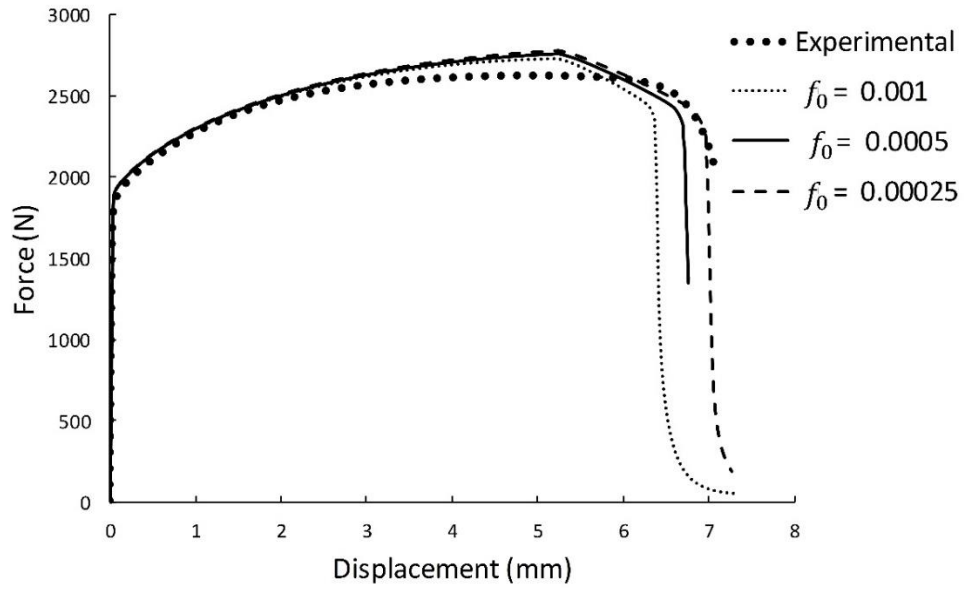
The porosity volume fraction can be related to the mechanical properties of porous materials through the following linear relation:

$$\frac{M_c}{M_s} = (1 - f)^{1/J} = V_s = \left(\frac{\rho_c}{\rho_s}\right)^{1/J} \quad (6.4)$$

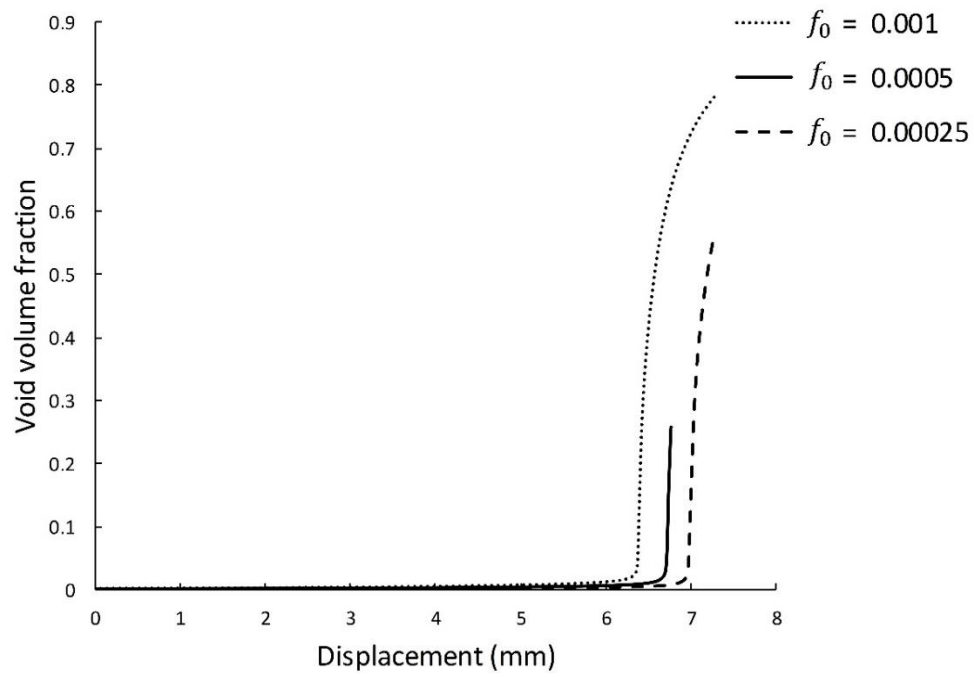
being $V_s = 1 - V_w$ the volume of the bulk and ρ_c and ρ_s are the density of the composite and bulk phases, respectively. After expanding Eq. (6.164) into power series and considering low porosity values $f < 0.1$ applicable for the DED processed samples of the present study, this equation can be approximated by

$$\frac{M_c}{M_s} = 1 - \frac{1}{J}f \quad (6.5)$$

Calculation of the J -factor parameter is carried out based on the procedure that was elaborated in [88]. This process requires calculating the melt pool cross section in different directions and thermal strains derived from different thermal gradients in every direction. The influence of process parameters such as laser power (W) has to be taken into account, while throughout the process, distribution of ellipsoid pores with dimensions a, b and c are considered as are shown in Figure 6.13.

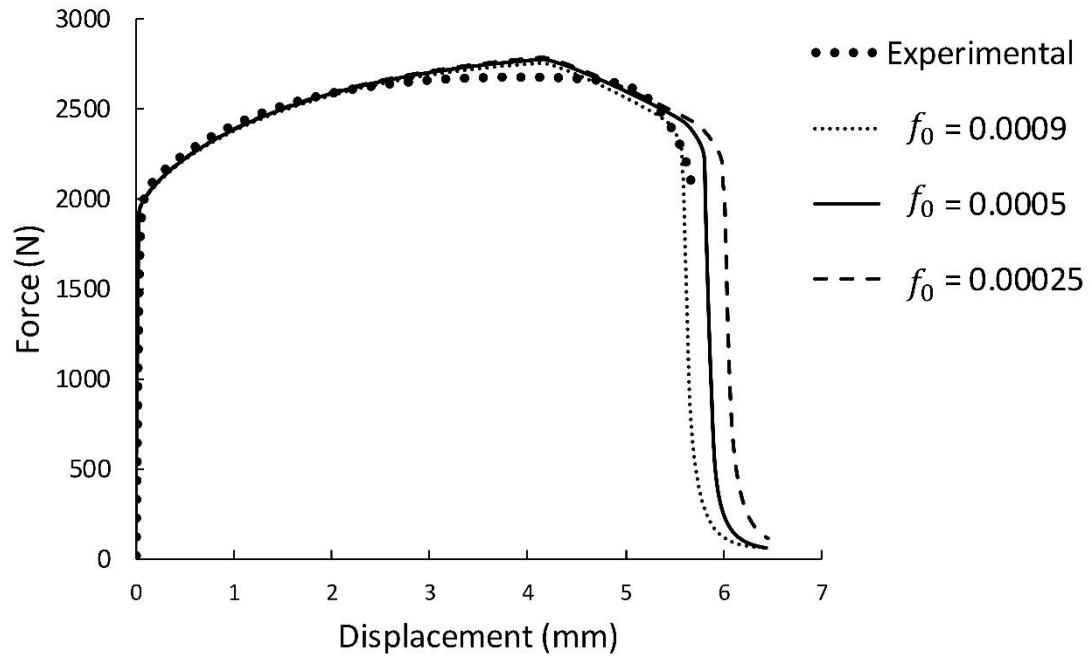


(a)

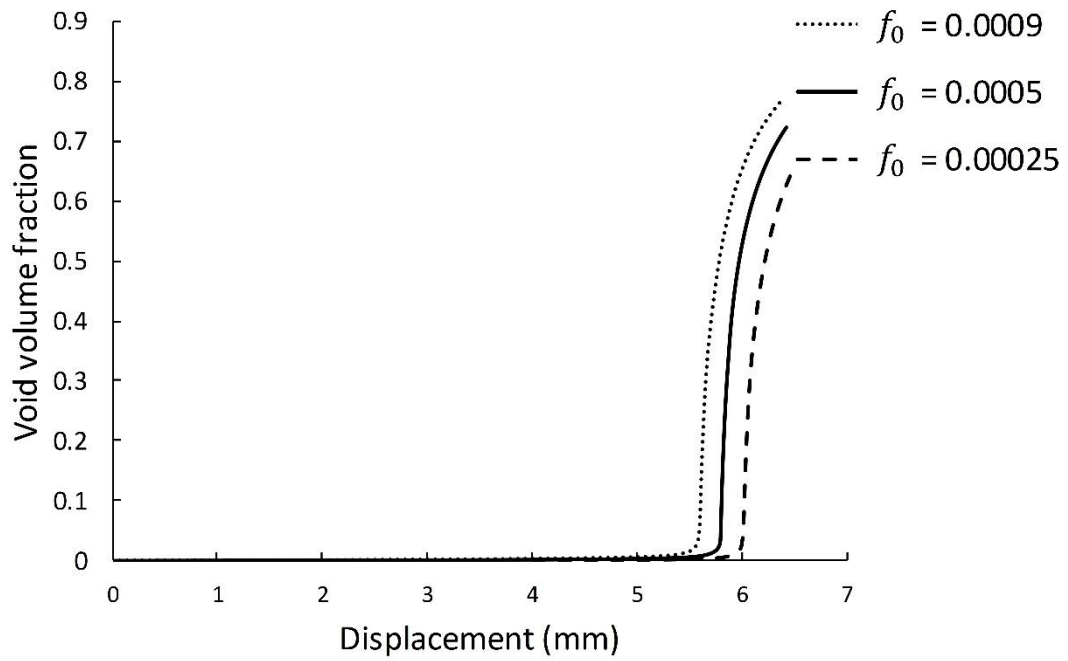


(b)

Figure 6.11 (a) Force versus displacement and (b) void volume fraction evolution for sample T11 using the local Rousselier model



(a)



(b)

Figure 6.12 (a) Force versus displacement and (b) void volume fraction evolution for sample T31 using the local Rousselier model

The dimension of the melt pool cross sections can be determined using the following relations:

$$A_{\vec{e}_x} = l \left(\frac{Q}{v(2l - h)} - t \right) \quad (6.6)$$

$$A_{\vec{e}_y} = (2l - h) \left(\frac{Q}{v(2l - h)} - t \right) \quad (6.7)$$

$$A_{\vec{e}_z} = l(2l - h) \quad (6.8)$$

with $Q = q^*/\rho_{\text{powder}}$ as the volumetric powder flow where q^* is the mass powder flow (mm/s), v is the scan speed of the laser beam (mm/s), ρ_{powder} is the density of powder and t is the layer thickness. In the above relation, $2l - h$ is the width of the melt pool in the hatch direction, with h being the hatch spacing as is depicted in Figure 6.14.

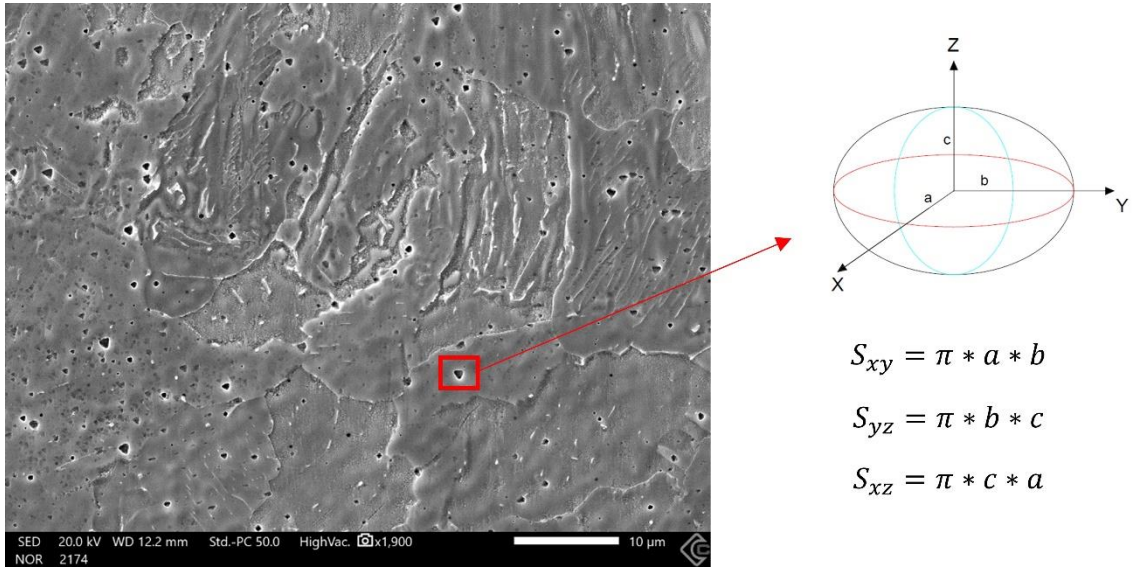


Figure 6.13 Ellipsoid pores with dimensions a, b and c in the fabricated component microstructure

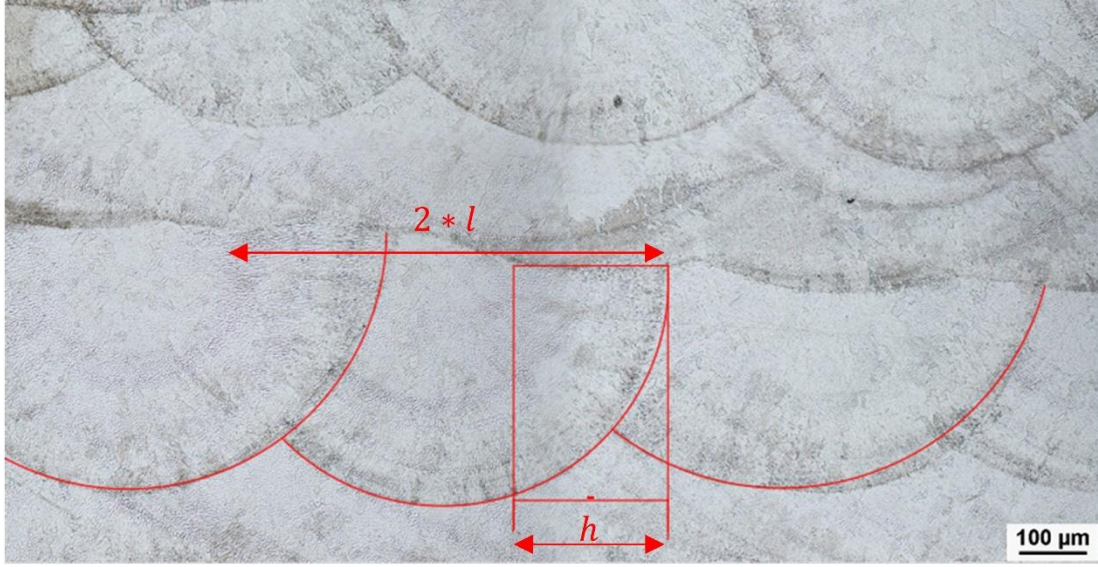


Figure 6.14 Melt pool dimensions in the fabricated component microstructure

Calculation of thermal strain parameter:

As previously discussed, lack of fusion during manufacturing process is known as a common cause for porosities in the as-fabricated components. This can be linked to the thermal distortions which could be characterised by a non-dimensional thermal strain parameter, ε^* , which can be calculated at each direction \vec{e}_i based on the Buckingham π theorem and using process parameters [101] as follows:

$$\varepsilon_{\vec{e}_i}^* = \frac{\chi \delta T \sqrt{\mathcal{V} t}}{\vartheta E I \sqrt{\rho_{\text{powder}}}} \hbar^{3/2} \quad (6.9)$$

where χ is the volumetric thermal expansion coefficient, δT is the temperature difference between the liquidus and solidus temperatures, \mathcal{V} is the volume of the melt pool, $\vartheta = \mathcal{K}/(\rho_{\text{powder}} c_p)$ is the thermal diffusivity with \mathcal{K} and c_p respectively as the thermal conductivity and specific heat of SS 316L. In the above definition, heat input parameter, \hbar , can be expressed by:

$$\hbar = \frac{\Upsilon P}{v} \quad (6.10)$$

where Υ is the absorption coefficient (to not be confused with the fracture coefficient in chapters 4 and 5) and P is the laser power (W). The variable I in Eq. (6.9) is the total moment of inertia of the porous media that is given by:

$$\begin{aligned}
[I_{total}] &= \begin{bmatrix} I_{xx} & I_{xy} & I_{xz} \\ I_{yx} & I_{yy} & I_{yz} \\ I_{zx} & I_{zy} & I_{zz} \end{bmatrix} \\
&= m \begin{bmatrix} \frac{9}{6} - \frac{N_1}{5}(b^2 + c^2) & -\frac{N_1}{5}(b^2 + c^2) & -\frac{N_1}{5}(b^2 + c^2) \\ -\frac{N_2}{5}(a^2 + c^2) & 9/6 - \frac{N_1}{5}(a^2 + c^2) & \frac{N_1}{5}(a^2 + c^2) \\ -\frac{N_3}{5}(b^2 + a^2) & -\frac{N_3}{5}(b^2 + a^2) & \frac{9}{6} - \frac{N_1}{5}(b^2 + a^2) \end{bmatrix} \quad (6.11)
\end{aligned}$$

where m is the mass of the nonporous material and N_1 , N_2 and N_3 are the number of pores, respectively in \vec{e}_x , \vec{e}_y and \vec{e}_z directions, which are derived by dividing the length, width and height of cube to the hatch space values in every directions.

Calculation of the J-factor parameter:

The mathematical relation between thermal strains and size of the pores in each direction can be obtained by curve fitting and written as:

$$C_1 \varepsilon_{\vec{e}_i}^{*2} + C_2 \varepsilon_{\vec{e}_i}^* + C_3 = (b^2 + c^2); (a^2 + c^2); (b^2 + a^2) \quad (6.12)$$

By using the following relation:

$$\vec{n} \cdot [I] \cdot \vec{e}_i = -\frac{N_3}{5}(b^2 + a^2); -\frac{N_1}{5}(b^2 + c^2); -\frac{N_2}{5}(a^2 + c^2) \quad (6.13)$$

the J -factor parameter can be associated with $\vec{n} \cdot [I] \cdot \vec{e}_i$ via curve fitting, yields the following expression:

$$J_{\vec{e}_i} = \exp(C_4 \vec{n} \cdot [I] \cdot \vec{e}_i) \quad (6.14)$$

In the scope of the present research, the value of C_4 is found to be the sum of C_i coefficients presented in Eq. (6.12). Taking the sample group $T3i$, at which based on the Figure 6.7 captures higher yield strength and moderately wider range of ductility compared to the other sample groups, the value of the J -factor can be associated to the material yield stress. The GMR relation expressed in Eq. (6.5) thus can be rewritten by using the initial porosity value instead of porosity and based on the values of yield stress as follows:

$$\frac{\sigma_y}{\sigma_{y1}} = \left(1 - \frac{1}{J_{\vec{e}_i}} f_0\right) \quad (6.15)$$

where σ_y and σ_{y1} are respectively the yield strength of each sample and a nominal strength value. In this regard, the values of the initial porosity are identified for each sample of group *T3i* using inverse finite element method based on the Rousselier damage model. Subsequent to the result of sample *T31* presented in Figure 6.12, the simulated curves of force-displacement for the remainder of samples of the group are graphed against the experimental curves and are illustrated in Figure 6.15, Figure 6.16, Figure 6.17 and Figure 6.18. Following the determination of the initial void volume fraction value based on these graphs, the identified values for all the sample are plotted against the yield stress of each sample from Table 6.5 as depicted through the scattered data in Figure 6.19 and the nominal stress value of $\sigma_{y1} = 524.5 \text{ MPa}$ is obtained using linear regression of this set of data for sample group *T3i*. The *J* factor parameter value is calculated using Eq. (6.14) as $J_3 = 0.00812$. By substituting this value in Eq. (6.15) and based on the yield stress of each sample, the values of initial void volume fraction are determined using GMR approach and given in Table 6.6. The estimated values are in a close agreement with the ones that were identified using the finite element simulations with the Rousselier damage criterion.

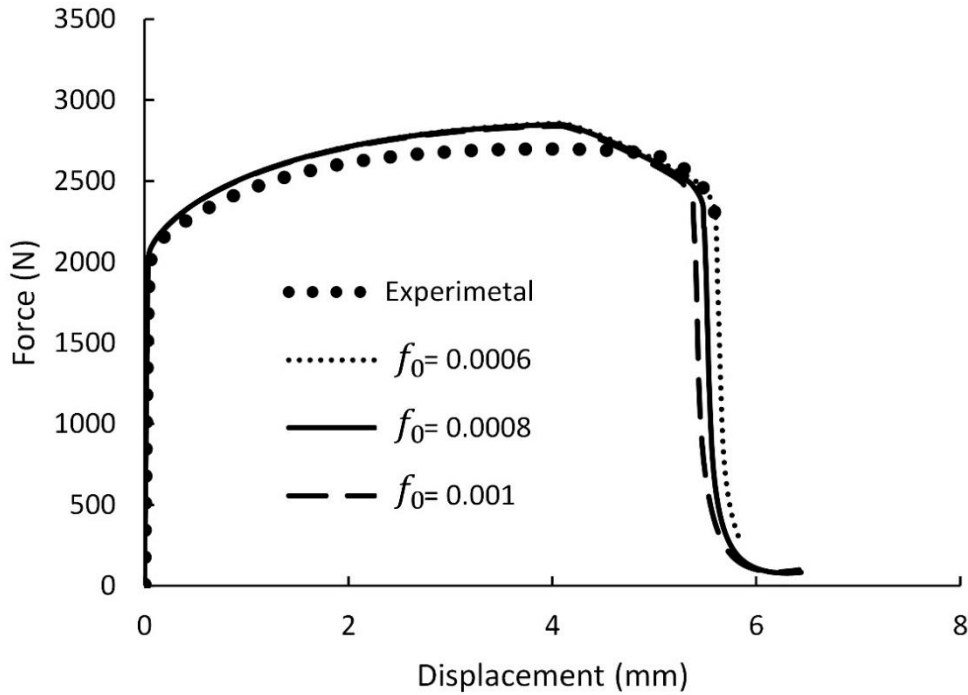


Figure 6.15 Force vs. displacement graph obtained from Rousselier damage model against experimental data for sample *T32*

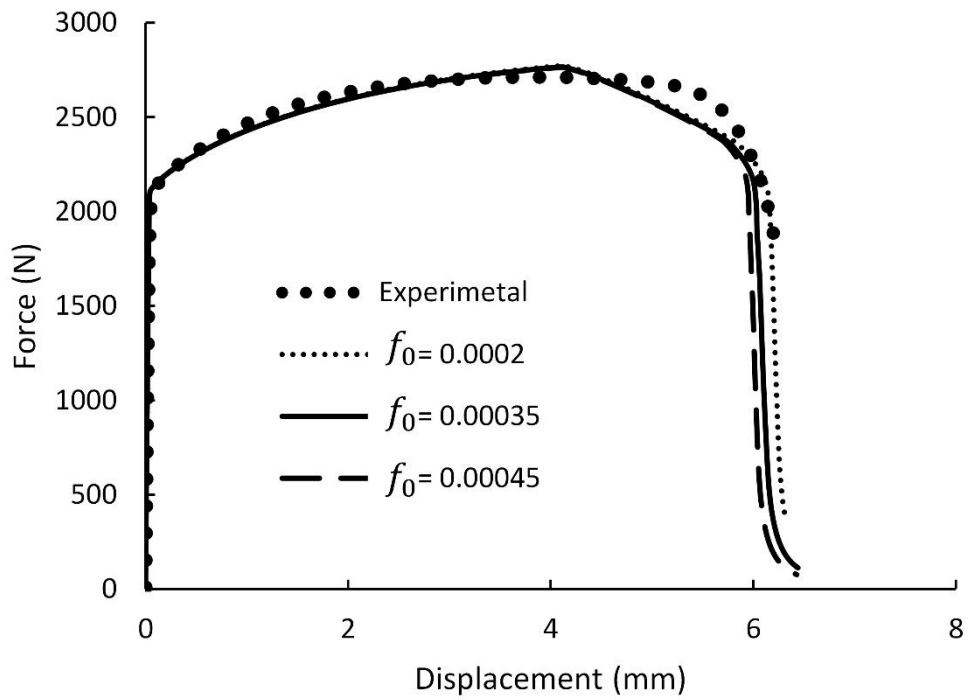


Figure 6.16 Force vs. displacement graph obtained from Rousselier damage model against experimental data for sample T33

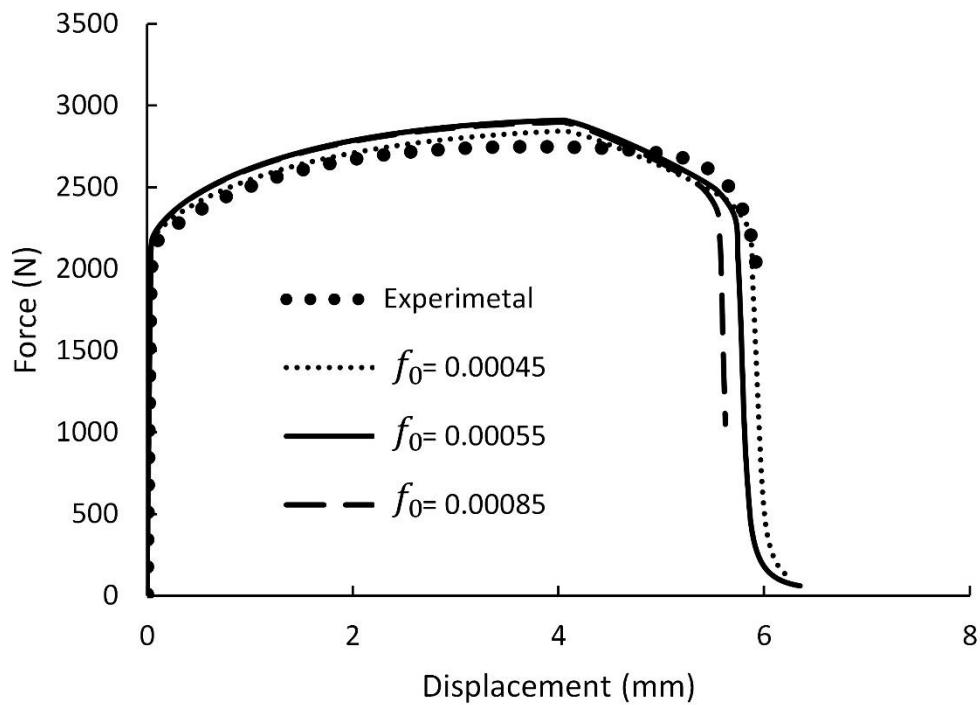


Figure 6.17 Force vs. displacement graph obtained from Rousselier damage model against experimental data for sample T34

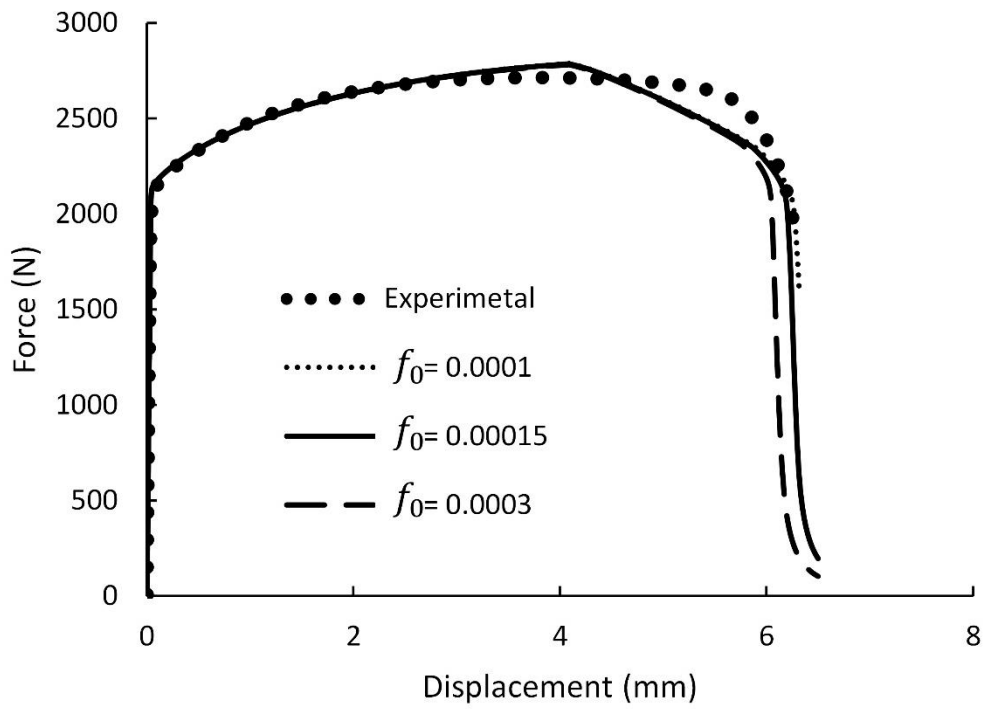


Figure 6.18 Force vs. displacement graph obtained from Rousselier damage model against experimental data for sample *T35*

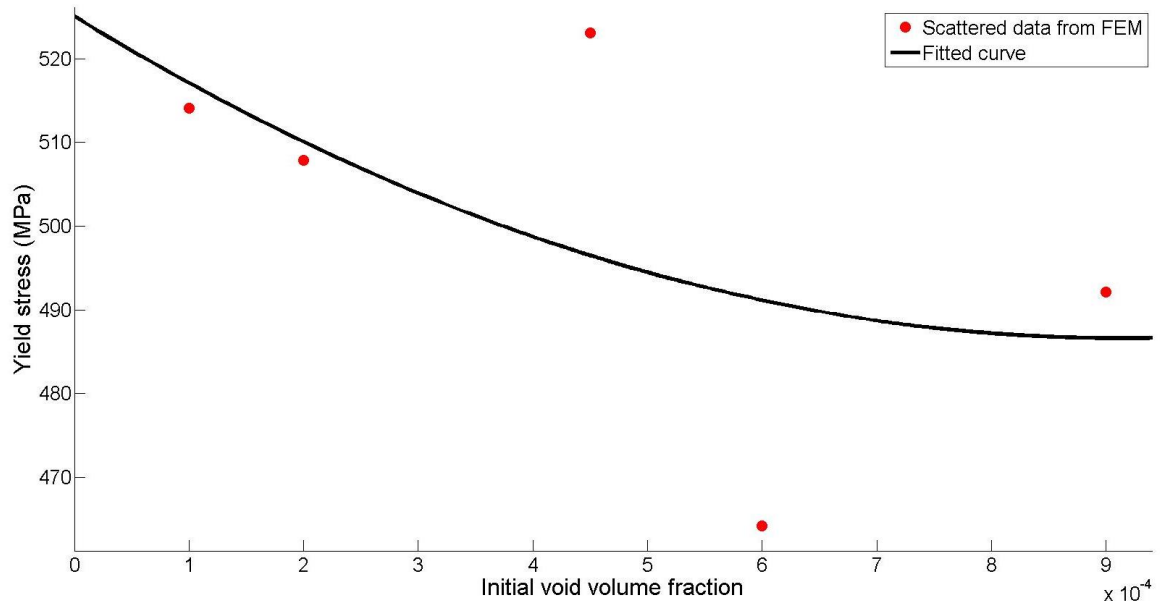


Figure 6.19 Linear regression of the scattered data of identified initial porosity values at yield strength of each sample of group *T3i*

Table 6.6 Comparison of identified values of initial porosity using FEM and GMR methods

Sample ID	Yield strength (<i>MPa</i>)	f_0 (FEM)	f_0 (GMR)
T31	464.2	9.0×10^{-4}	9.5×10^{-4}
T32	492.1	6.0×10^{-4}	5.2×10^{-4}
T33	507.9	2.0×10^{-4}	2.73×10^{-4}
T34	523.1	4.5×10^{-4}	3.58×10^{-4}
T35	514.1	1.0×10^{-4}	1.76×10^{-4}

6.2.3. Crack analysis using phase-field ductile fracture model

The performance of the numerical approach using the coupled phase-field ductile fracture model is investigated in this part of the work. Using the finite element mesh discretisation and the model parameters that are determined in the previous section, the simulations are performed for T11 and T31 samples. The following parameters corresponding to the phase-field model are adopted: phase-field length scale $l_d = 0.04 \text{ mm}$, critical energy release rate $\mathcal{G}_c = 12.0 \text{ N/mm}$ and $f_c = 0.03$. The fracture coefficient in the crack state function of Eq. (4.46) is set to $\eta = 1$ for all simulations. Regarding critical porosity parameter, this value was chosen rather empirically (some researchers proposed that this value should be at least one order of magnitude higher than the initial porosity) as its variation produced less discrepant force graphs in this particular example. Thus, apart from inverse FEM procedure that previously triggered for identification of the initial porosity, determination of this value needs more in-depth research which is out of the scope of this study.

The force -displacement graphs obtained from the phase-field ductile fracture model are plotted against experimental data in Figure 6.20 where a good agreement is achieved between the results. The contour plots of the state variables including the equivalent plastic strain and the phase-field are demonstrated for sample T11 in Figure 6.21. The phase-field crack is initiated when the axial strain reaches $\varepsilon_{22} = 0.63$, spotted at the upper half and roughly 2.62 mm away from the center of specimen. Then the crack grows directed outward to the side edges along the angle of about 80° with respect to the loading direction. This is in line with the fractography observation in Figure 6.10, where the crack initiated at the center of the upper half of the sample.

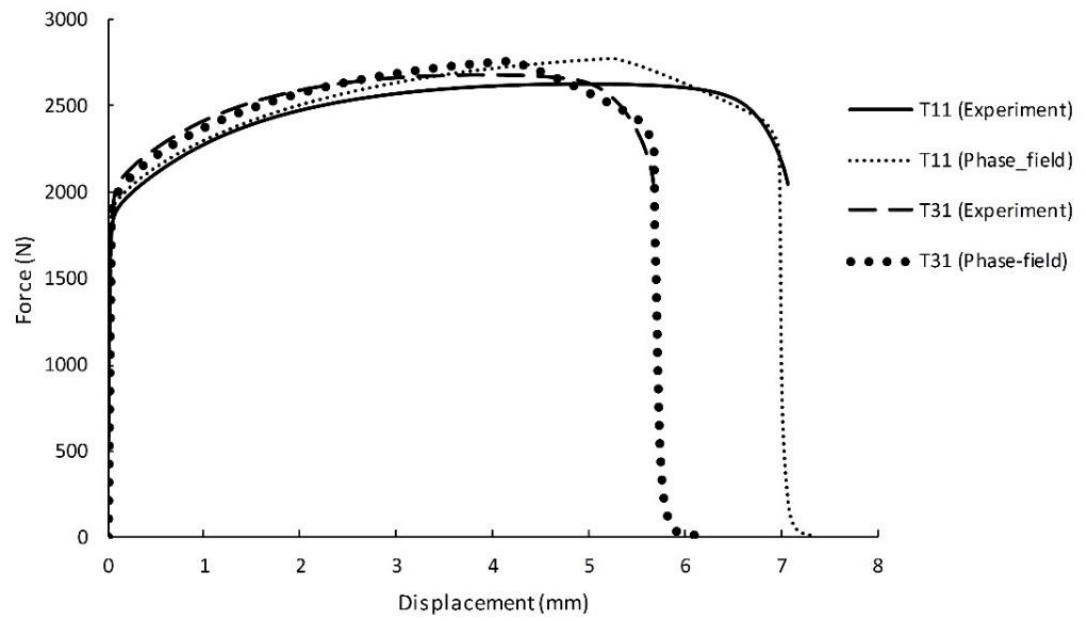


Figure 6.20 Force versus displacement for samples T11 and T31 using the phase-field ductile fracture model

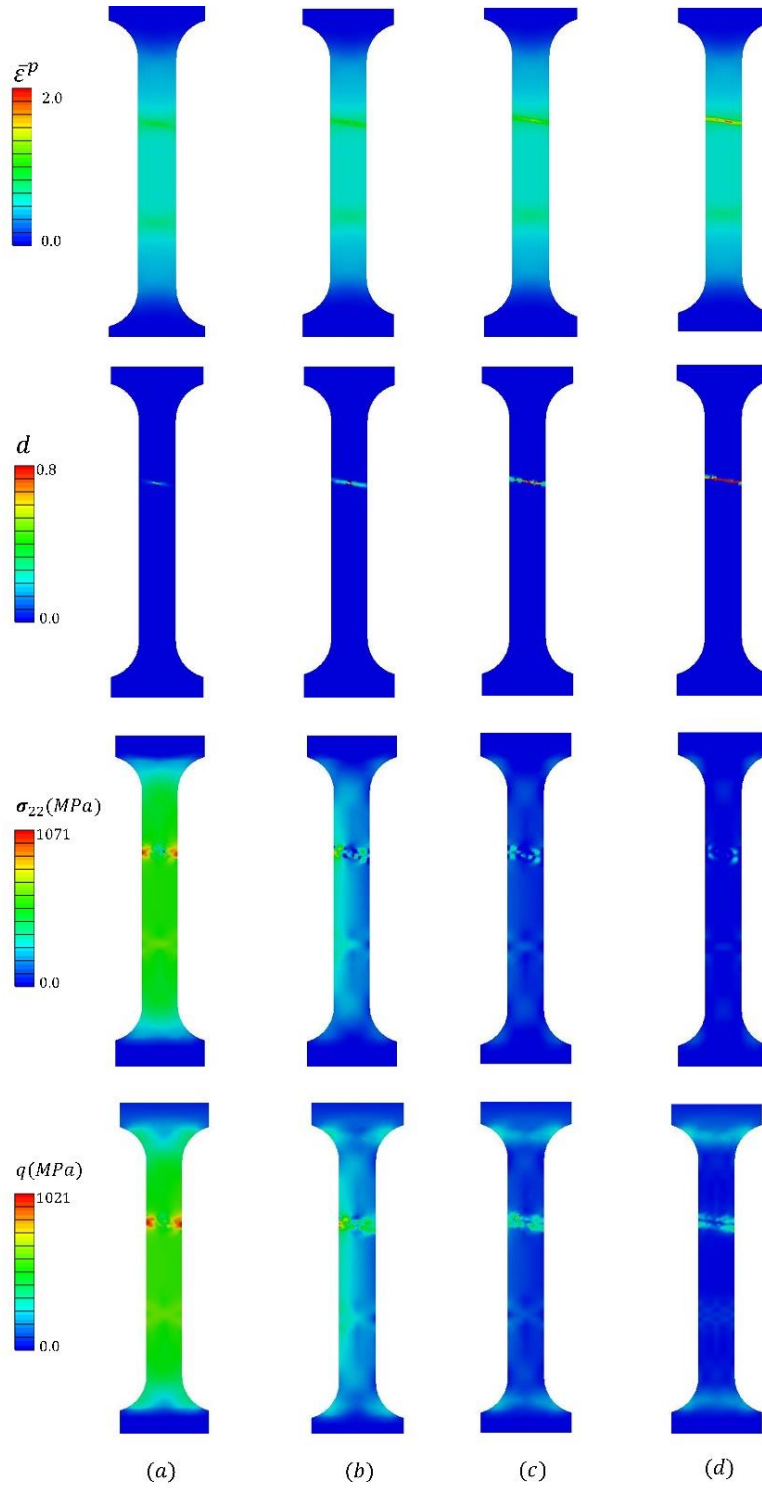


Figure 6.21 Distribution of equivalent plastic strain, phase-field crack, axial stress and von-Mises equivalent stress in the post-critical regime for sample T11 and at different deformation levels: a) $\varepsilon_{22} = 63\%$, b) $\varepsilon_{22} = 63.8\%$, c) $\varepsilon_{22} = 64.3\%$ and d) $\varepsilon_{22} = 66.8\%$

7 Summary and conclusions

The numerical modelling of ductile fracture through the analysis of damage accumulation that precedes initiation and propagation of cracks was studied. Gradient regularisation of the internal damage variable was addressed by utilising a diffusive gradient equation that has roots in continuous damage mechanics and fracture mechanics. In this regard, the major contribution of the present study was to blend the concept of phase-field diffusive approach in fracture with a micromechanically-motivated damage model, at which an alternative form of crack driving force was introduced based on the state variables that governs the material bulk softening response. This feature and the use crack initiation criterion based on a condition of a material parameter were addressed as key modifications to generalise the phase-field conventional concept to a stress-based criteria.

The pressure-dependent plasticity model based on the Rousselier criterion was employed as an underlying damage model and the main assumptions to perform the coupling between the damage in material bulk and the phase-field diffusion were presented, alongside with the finite element implementation and numerical integration of the multi-field problem. Apart from the importance of this treatment of fracture, in line with extending the conventional phase-field concept to the ductile fracture, this can be regarded, alternatively, as an generalisation of the micromechanical ductile damage framework to model the macro-crack propagation by accelerating the material softening in the post-critical regime. By the same token, this may viewed as the development of void coalescence criteria that are associated with the ductile damage modelling, as for instance in [34].

Following another path, the gradient nonlocal damage methodology was applied to a continuous damage model, in order to alleviate the mesh-dependent issues coming from the PDEs governing the mathematical model. A strategy, in the finite element framework, was utilised to simplify the numerical implementation of the coupled problem by taking advantage of the analogy between the gradient nonlocal equation with the heat conduction equation. Using this strategy, the heat conductivity takes the role of the length parameter in the structure of diffusion equation and the built-in thermo-mechanical coupled finite element procedure in Abaqus is responsible for solution of the diffusive equation for the nonlocal damage value.

7.1. Concluding remarks

The performance of the above material models was investigated through numerical analysis on several fracture benchmarks. The reliability of the phase-field ductile fracture model was further assessed via post-critical damage analysis on additively-manufactured steel components with the emphasis on porosity growth. The following conclusions can be drawn:

1. The problem of mesh dependency was analysed on a tensile plane strain specimen using the nonlocal gradient model based on the Lemaitre damage criterion. Less sensitivity of the nonlocal problem solution to the finite element discretisation using three different meshes was recognised through the graphs of force-displacement and damage evolution.
2. The phase-field ductile fracture model was analysed via simulations based on several fracture benchmarks that cover a wide range of triaxialities. Throughout the validation process, the role of the fracture coefficient that appears in the crack driving state function, the phase-field length scale parameter, the accumulation of damage and plastic deformations and the crack propagation patterns were addressed.
3. The material global response in notched round bars was found to be sensitive to the choice of the initial porosity value and the fracture coefficient, which controls the softening behaviour in the post critical material regime. In most numerical results, the critical porosity value had a minor influence in this material phase.
4. As for the numerical tests on the plates with notches, the predicted fracture pattern by the phase-field ductile fracture model in the asymmetrical notched plate was in high accordance with the experimental observations in [80]. Regarding the shear sample test, the crack propagation pattern was verified by comparing the shear band formation with the provided experimental observations in literature. The influences of the fracture coefficient and the phase-field length parameter were also investigated, showing how the increase in either of parameters directly induces more material softening in the post critical regime.
5. The simulation results of the additively-manufactured miniature-sized tensile samples were found to be in good agreement with the experimental observations.

The modelling of the global material response was approved by comparing experimental data for two of the samples that were excised from the component cube in different orientations. The qualitative performance of the model presented through comparisons of the FEM-based contour plots with the actual fracture location in one of the samples and the outcome was acceptable. However, it was observed some dependence of numerical fracture pattern on the choice of finite element mesh discretisation.

7.2. Future work

The overall objectives of the study including the acceptable numerical predictive ability to monitor initiation and propagation of cracks using the gradient approaches in ductile fracture modelling were achieved.

Nevertheless, the following recommendation in the scope of future model development could be taken into consideration:

1. Throughout the study, material models were established based on isotropy of damage and plasticity. However, the micromechanical damage material framework herein may be extended to include the anisotropy of plasticity and Lode angle effects within the constitutive material modelling, making it more appropriate to be utilised, for instance, in the context of sheet metal forming processes.
2. The computational performance of the phase-field ductile fracture model was verified in two-dimensional problems including plane and axis-symmetric settings. Some difficulties were felt during the simulation of three-dimensional structures related to poor convergence of the integration algorithm. This issue could be associated with the local Rousselier damage model integration and needs more investigation.
3. Modelling the Rousselier damage evolution in this study followed the original version of the model where solely the cavity growth drives the material degradation through damage softening. Despite the good predictive ability of the coupled model in the presented shear sample, this model can be extended by adding a shear term to the void growth rate and its possible improvement should be analysed with more sophisticated benchmarks. Utilisation of other damage

model frameworks such as Lemaitre or GTN models for coupling with the phase-field fracture problem could be another perspective to pursue in future studies.

4. As for the numerical study of fracture in additive manufacturing samples, further investigation is required regarding the void inclusion analysis and the influence of the electro-discharge machining orientation on the structural response.
5. Several mesh-biased issues were observed in the numerical simulations correspond to the phase-field ductile fracture model. This problem requires further investigation and possibly this could be alleviated by utilising alternative phase-field available formats, such as the one proposed in [102], at which it has an elastic domain unlike the phase-field model of Miehe et al. [6]. In [103], it is claimed that the former model is also moderately less mesh sensitive than the phase-field format used in this study. Nevertheless, it has been widely accepted that phase-field models are not mesh sensitive for sufficiently refined meshes, what comes at the cost of large computational efforts. Achieving a balance on this respect could be an issue of further research.

Appendix A

Coefficients in Eq. (4.51):

$$\begin{aligned}
J_{11} &= \frac{\partial k^2}{\partial H^2} \frac{\partial k^1}{\partial \Delta \epsilon_p} - \frac{\partial k^1}{\partial H^2} \frac{\partial k^2}{\partial \Delta \epsilon_p} , & J_{12} &= \frac{\partial k^2}{\partial H^2} \frac{\partial k^1}{\partial \Delta \epsilon_q} - \frac{\partial k^1}{\partial H^2} \frac{\partial k^2}{\partial \Delta \epsilon_q} \\
J_{21} &= \frac{\partial k^2}{\partial H^2} \frac{\partial k^1}{\partial p} - \frac{\partial k^1}{\partial H^2} \frac{\partial k^2}{\partial p} , & J_{22} &= -\frac{\partial k^2}{\partial H^2} \frac{\partial k^1}{\partial q} - \frac{\partial k^1}{\partial H^2} \frac{\partial k^2}{\partial q} \\
L_{11} &= -\frac{\partial k^2}{\partial H^1} \frac{\partial k^1}{\partial \Delta \epsilon_p} + \frac{\partial k^1}{\partial H^1} \frac{\partial k^2}{\partial \Delta \epsilon_p} , & L_{12} &= -\frac{\partial k^2}{\partial H^1} \frac{\partial k^1}{\partial \Delta \epsilon_q} + \frac{\partial k^1}{\partial H^1} \frac{\partial k^2}{\partial \Delta \epsilon_q} \\
L_{21} &= -\frac{\partial k^2}{\partial H^1} \frac{\partial k^1}{\partial p} + \frac{\partial k^1}{\partial H^1} \frac{\partial k^2}{\partial p} , & L_{22} &= -\frac{\partial k^2}{\partial H^1} \frac{\partial k^1}{\partial q} + \frac{\partial k^1}{\partial H^1} \frac{\partial k^2}{\partial q} \\
w &= \frac{\partial k^1}{\partial H^1} \frac{\partial k^2}{\partial H^2} - \frac{\partial k^2}{\partial H^1} \frac{\partial k^1}{\partial H^2}
\end{aligned} \tag{A.1}$$

Appendix B

Coefficients in Eqs. (4.76) and (4.77):

$$\begin{aligned}
 A_{11} = & \frac{\partial \Phi}{\partial q} + \Delta \epsilon_p \left(K \frac{\partial^2 \Phi}{\partial q \partial p} + \sum_{\gamma=1}^{n_H} \frac{\partial^2 \Phi}{\partial q \partial H^\gamma} \frac{\partial H^\gamma}{\partial \Delta \epsilon_p} \right) \\
 & + \Delta \epsilon_q \left(K \frac{\partial^2 \Phi}{\partial p^2} + \sum_{\gamma=1}^{n_H} \frac{\partial^2 \Phi}{\partial p \partial H^\gamma} \frac{\partial H^\gamma}{\partial \Delta \epsilon_p} \right)
 \end{aligned} \tag{B.1}$$

$$\begin{aligned}
 A_{12} = & \frac{\partial \Phi}{\partial p} + \Delta \epsilon_p \left(-3G \frac{\partial^2 \Phi}{\partial q^2} + \sum_{\gamma=1}^{n_H} \frac{\partial^2 \Phi}{\partial q \partial H^\gamma} \frac{\partial H^\gamma}{\partial \Delta \epsilon_q} \right) \\
 & + \Delta \epsilon_q \left(-3G \frac{\partial^2 \Phi}{\partial p \partial q} + \sum_{\gamma=1}^{n_H} \frac{\partial^2 \Phi}{\partial p \partial H^\gamma} \frac{\partial H^\gamma}{\partial \Delta \epsilon_q} \right)
 \end{aligned} \tag{B.2}$$

$$A_{21} = K \frac{\partial \Phi}{\partial p} + \sum_{\gamma=1}^{n_H} \frac{\partial \Phi}{\partial H^\gamma} \frac{\partial H^\gamma}{\partial \Delta \epsilon_p} \tag{B.3}$$

$$A_{22} = -3G \frac{\partial \Phi}{\partial q} + \sum_{\gamma=1}^{n_H} \frac{\partial \Phi}{\partial H^\gamma} \frac{\partial H^\gamma}{\partial \Delta \epsilon_q} \tag{B.4}$$

$$b_1 = -\Delta \epsilon_p \frac{\partial \Phi}{\partial q} - \Delta \epsilon_q \frac{\partial \Phi}{\partial p} \tag{B.5}$$

$$b_2 = -\Phi \tag{B.6}$$

Appendix C

Coefficients in Eqs. (4.96) and (4.97):

$$\bar{A}_{11} = \frac{\partial \Phi}{\partial q} + \Delta \epsilon_p \left(\sum_{\gamma=1}^{n_H} \frac{\partial^2 \Phi}{\partial q \partial H^\gamma} \frac{\partial H^\gamma}{\Delta \epsilon_p} \right) + \Delta \epsilon_q \left(\sum_{\gamma=1}^{n_H} \frac{\partial^2 \Phi}{\partial p \partial H^\gamma} \frac{\partial H^\gamma}{\Delta \epsilon_p} \right) \quad (\text{C.1})$$

$$\bar{A}_{12} = \frac{\partial \Phi}{\partial p} + \Delta \epsilon_p \left(\sum_{\gamma=1}^{n_H} \frac{\partial^2 \Phi}{\partial q \partial H^\gamma} \frac{\partial H^\gamma}{\Delta \epsilon_q} \right) + \Delta \epsilon_q \left(\sum_{\gamma=1}^{n_H} \frac{\partial^2 \Phi}{\partial p \partial H^\gamma} \frac{\partial H^\gamma}{\Delta \epsilon_q} \right) \quad (\text{C.2})$$

$$\bar{A}_{21} = \sum_{\gamma=1}^{n_H} \frac{\partial \Phi}{\partial H^\gamma} \frac{\partial H^\gamma}{\partial \Delta \epsilon_p} \quad (\text{C.3})$$

$$\bar{A}_{22} = \sum_{\gamma=1}^{n_H} \frac{\partial \Phi}{\partial H^\gamma} \frac{\partial H^\gamma}{\partial \Delta \epsilon_q} \quad (\text{C.4})$$

$$B_{11} = \frac{1}{3} \Delta \epsilon_p \left(\frac{\partial^2 \Phi}{\partial q \partial p} + \sum_{\gamma=1}^{n_H} \frac{\partial^2 \Phi}{\partial q \partial H^\gamma} \frac{\partial H^\gamma}{\partial p} \right) \frac{1}{3} \Delta \epsilon_q \left(\frac{\partial^2 \Phi}{\partial^2 p} + \sum_{\gamma=1}^{n_H} \frac{\partial^2 \Phi}{\partial p \partial H^\gamma} \frac{\partial H^\gamma}{\partial p} \right) \quad (\text{C.5})$$

$$B_{12} = -\Delta \epsilon_p \left(\frac{\partial^2 \Phi}{\partial^2 q} + \sum_{\gamma=1}^{n_H} \frac{\partial^2 \Phi}{\partial q \partial H^\gamma} \frac{\partial H^\gamma}{\partial q} \right) - \Delta \epsilon_q \left(\frac{\partial^2 \Phi}{\partial p \partial q} + \sum_{\gamma=1}^{n_H} \frac{\partial^2 \Phi}{\partial p \partial H^\gamma} \frac{\partial H^\gamma}{\partial q} \right) \quad (\text{C.6})$$

$$B_{21} = \frac{1}{3} \left(\frac{\partial \Phi}{\partial p} + \sum_{\gamma=1}^{n_H} \frac{\partial \Phi}{\partial H^\gamma} \frac{\partial H^\gamma}{\partial p} \right) \quad (\text{C.7})$$

$$B_{22} = - \left(\frac{\partial \Phi}{\partial q} + \sum_{\gamma=1}^{n_H} \frac{\partial \Phi}{\partial H^\gamma} \frac{\partial H^\gamma}{\partial q} \right) \quad (\text{C.8})$$

For $n_H = 2$, the derivatives of internal variables H^1 and H^2 are given by:

$$\frac{\partial H^1}{\partial \Delta \epsilon_p} = e_{11} \left(\frac{\partial h^1}{\partial \Delta \epsilon_p} \right) + e_{12} \left(\frac{\partial h^2}{\partial \Delta \epsilon_p} \right) \quad (\text{C.9a})$$

$$\frac{\partial H^1}{\partial \Delta \epsilon_q} = e_{11} \left(\frac{\partial h^1}{\partial \Delta \epsilon_q} \right) + e_{12} \left(\frac{\partial h^2}{\partial \Delta \epsilon_q} \right) \quad (\text{C.9b})$$

$$\frac{\partial H^2}{\partial \Delta \epsilon_p} = e_{21} \left(\frac{\partial h^1}{\partial \Delta \epsilon_p} \right) + e_{22} \left(\frac{\partial h^2}{\partial \Delta \epsilon_p} \right) \quad (\text{C.10a})$$

$$\frac{\partial H^2}{\partial \Delta \epsilon_q} = e_{21} \left(\frac{\partial h^1}{\partial \Delta \epsilon_q} \right) + e_{22} \left(\frac{\partial h^2}{\partial \Delta \epsilon_q} \right) \quad (\text{C.10b})$$

$$\frac{\partial H^1}{\partial p} = e_{11} \left(\frac{\partial h^1}{\partial p} \right) + e_{12} \left(\frac{\partial h^2}{\partial p} \right) \quad (\text{C.11a})$$

$$\frac{\partial H^1}{\partial q} = e_{11} \left(\frac{\partial h^1}{\partial q} \right) + e_{12} \left(\frac{\partial h^2}{\partial q} \right) \quad (\text{C.11b})$$

$$\frac{\partial H^2}{\partial p} = e_{21} \left(\frac{\partial h^1}{\partial p} \right) + e_{22} \left(\frac{\partial h^2}{\partial p} \right) \quad (\text{C.12a})$$

$$\frac{\partial H^2}{\partial q} = e_{21} \left(\frac{\partial h^1}{\partial q} \right) + e_{22} \left(\frac{\partial h^2}{\partial q} \right) \quad (\text{C.12b})$$

where

$$e_{11} = \frac{1}{\beta} \left(I_{22} - \frac{\partial h^2}{\partial H^2} \right) \quad (\text{C.13a})$$

$$e_{12} = \frac{1}{\beta} \left(\frac{\partial h^1}{\partial H^2} \right) \quad (\text{C.13b})$$

$$e_{21} = \frac{1}{\beta} \left(\frac{\partial h^2}{\partial H^1} \right) \quad (\text{C.14a})$$

$$e_{22} = \frac{1}{\beta} \left(I_{11} - \frac{\partial h^1}{\partial H^1} \right) \quad (\text{C.14b})$$

$$\beta = \left(I_{11} - \frac{\partial h^1}{\partial H^1} \right) \left(I_{22} - \frac{\partial h^2}{\partial H^2} \right) - \left(I_{21} - \frac{\partial h^2}{\partial H^1} \right) \left(I_{12} - \frac{\partial h^1}{\partial H^2} \right) \quad (\text{C.15})$$

being I_{ij} the components of the identity tensor \mathbf{I} .

Appendix D

Coefficients in Eqs. (4.98) and (4.99):

$$C_{11} = \frac{1}{\bar{\beta}} [(\bar{A}_{22} + 3GB_{22})B_{11} - (\bar{A}_{12} + 3GB_{12})B_{21}] \quad (\text{C.161})$$

$$C_{21} = \frac{1}{\bar{\beta}} [(\bar{A}_{11} + 3KB_{11})B_{21} - (\bar{A}_{21} + 3KB_{21})B_{11}] \quad (\text{C.17})$$

$$C_{12} = \frac{1}{\bar{\beta}} [(\bar{A}_{22} + 3GB_{22})B_{12} - (\bar{A}_{12} + 3GB_{12})B_{22}] \quad (\text{C.18})$$

$$C_{22} = \frac{1}{\bar{\beta}} [(\bar{A}_{11} + 3KB_{11})B_{22} - (\bar{A}_{21} + 3KB_{21})B_{12}] \quad (\text{C.19})$$

where

$$\bar{\beta} = (\bar{A}_{11} + 3KB_{11})(\bar{A}_{22} + 3GB_{22}) - (\bar{A}_{12} + 3GB_{11})(\bar{A}_{21} + 3KB_{21}) \quad (\text{C.20})$$

References

- [1] Moes N, Dolbow J, Belytschko T. A finite element method for crack growth without remeshing. *Int J Numer Methods Eng* 1999;**46**:131–150. [https://doi.org/10.1002/\(SICI\)1097-0207\(19990910\)46:1<131::AID-NME726>3.0.CO;2-J](https://doi.org/10.1002/(SICI)1097-0207(19990910)46:1<131::AID-NME726>3.0.CO;2-J).
- [2] Ingraffea AR, Saouma V. Numerical modeling of discrete crack propagation in reinforced and plain concrete. *Fract. Mech. Concr. Struct. Appl. Numer. Calc.*, Dordrecht: Springer Netherlands; 1985, p. 171–225. https://doi.org/10.1007/978-94-009-6152-4_4.
- [3] Belytschko T, Lu YY, Gu L. Element-free Galerkin methods. *Int J Numer Methods Eng* 1994;**37**:229–56. <https://doi.org/10.1002/nme.1620370205>.
- [4] Bourdin B, Francfort GA, Marigo J-J. Numerical experiments in revisited brittle fracture. *J Mech Phys Solids* 2000;**48**:797–826. [https://doi.org/10.1016/S0022-5096\(99\)00028-9](https://doi.org/10.1016/S0022-5096(99)00028-9).
- [5] Ambrosio L, Tortorelli VM. Approximation of functional depending on jumps by elliptic functional via t-convergence. *Commun Pure Appl Math* 1990;**43**:999–1036. <https://doi.org/10.1002/cpa.3160430805>.
- [6] Miehe C, Welschinger F, Hofacker M. Thermodynamically consistent phase-field models of fracture: Variational principles and multi-field FE implementations. *Int J Numer Methods Eng* 2010;**83**:1273–1311. <https://doi.org/10.1002/nme.2861>.
- [7] Miehe C, Hofacker M, Welschinger F. A phase field model for rate-independent crack propagation: Robust algorithmic implementation based on operator splits. *Comput Methods Appl Mech Eng* 2010;**199**:2765–2778. <https://doi.org/10.1016/j.cma.2010.04.011>.
- [8] Kuhn C, Müller R. A continuum phase field model for fracture. *Eng Fract Mech* 2010;**77**:3625–3634. <https://doi.org/10.1016/j.engfracmech.2010.08.009>.
- [9] Molnár G, Gravouil A. 2D and 3D Abaqus implementation of a robust staggered phase-field solution for modeling brittle fracture. *Finite Elem Anal Des* 2017;**130**:27–38. <https://doi.org/10.1016/j.finel.2017.03.002>.
- [10] Msekh MA, Sargado JM, Jamshidian M, Areias PM, Rabczuk T. Abaqus

- implementation of phase-field model for brittle fracture. *Comput Mater Sci* 2015;**96**:472–484. <https://doi.org/10.1016/j.commatsci.2014.05.071>.
- [11] Liu G, Li Q, Msekh MA, Zuo Z. Abaqus implementation of monolithic and staggered schemes for quasi-static and dynamic fracture phase-field model. *Comput Mater Sci* 2016;**121**:35–47. <https://doi.org/10.1016/j.commatsci.2016.04.009>.
- [12] Ambati M, Gerasimov T, De Lorenzis L. Phase-field modeling of ductile fracture. *Comput Mech* 2015;**55**:1017–1040. <https://doi.org/10.1007/s00466-015-1151-4>.
- [13] Miehe C, Hofacker M, Schaezel L-MM, Aldakheel F. Phase field modeling of fracture in multi-physics problems. Part II. Coupled brittle-to-ductile failure criteria and crack propagation in thermo-elastic–plastic solids. *Comput Methods Appl Mech Eng* 2015;**294**:1–37. <https://doi.org/10.1016/j.cma.2014.11.017>.
- [14] Borden MJ, Hughes TJR, Landis CM, Anvari A, Lee IJ. A phase-field formulation for fracture in ductile materials: Finite deformation balance law derivation, plastic degradation, and stress triaxiality effects. *Comput Methods Appl Mech Eng* 2016;**312**:130–166. <https://doi.org/10.1016/j.cma.2016.09.005>.
- [15] Aldakheel F, Wriggers P, Miehe C. A modified Gurson-type plasticity model at finite strains: formulation, numerical analysis and phase-field coupling. *Comput Mech* 2017;**62**:815–833. <https://doi.org/10.1007/s00466-017-1530-0>.
- [16] Alessi R, Vidoli S, De Lorenzis L. A phenomenological approach to fatigue with a variational phase-field model: The one-dimensional case. *Eng Fract Mech* 2018;**190**:53–73. <https://doi.org/10.1016/j.engfracmech.2017.11.036>.
- [17] Clemens V. Verhoosel,* and R de B, 1Department. A phase-field model for cohesive fracture. *Int J Numer Methods Eng* 2013;**96**:43–62. <https://doi.org/10.1002/nme.4553> A.
- [18] Vignollet J, May S, de Borst R, Verhoosel C V. Phase-field models for brittle and cohesive fracture. *Meccanica* 2014;**49**:2587–2601. <https://doi.org/10.1007/s11012-013-9862-0>.
- [19] Gurson AL. Continuum Theory of Ductile Rupture by Void Nucleation and Growth: Part I—Yield Criteria and Flow Rules for Porous Ductile Media. *J Eng*

- Mater Technol 1977;99:2. <https://doi.org/10.1115/1.3443401>.
- [20] Nahshon K, Hutchinson JW. Modification of the Gurson Model for shear failure. Eur J Mech A/Solids 2008;**27**:1–17. <https://doi.org/10.1016/j.euromechsol.2007.08.002>.
- [21] Xue L. Constitutive modeling of void shearing effect in ductile fracture of porous materials. Eng Fract Mech 2008;**75**:3343–3366. <https://doi.org/10.1016/j.engfracmech.2007.07.022>.
- [22] Tvergaard V, Needleman A. Analysis of the cup-cone fracture in a round tensile bar. Acta Metall 1984;**32**:157–69. [https://doi.org/10.1016/0001-6160\(84\)90213-X](https://doi.org/10.1016/0001-6160(84)90213-X).
- [23] Rousselier G. Ductile fracture models and their potential in local approach of fracture. Nucl Eng Des 1987;**105**:97–111. [https://doi.org/10.1016/0029-5493\(87\)90234-2](https://doi.org/10.1016/0029-5493(87)90234-2).
- [24] Rousselier G. Dissipation in porous metal plasticity and ductile fracture. J Mech Phys Solids 2001;**49**:1727–1746. [https://doi.org/10.1016/S0022-5096\(01\)00013-8](https://doi.org/10.1016/S0022-5096(01)00013-8).
- [25] Besson J, Steglich D, Brocks W. Modeling of plane strain ductile rupture. Int J Plast 2003;**19**:1517–1541. [https://doi.org/10.1016/S0749-6419\(02\)00022-0](https://doi.org/10.1016/S0749-6419(02)00022-0).
- [26] Lorentz E, Besson J, Cano V. Numerical simulation of ductile fracture with the Rousselier constitutive law. Comput Methods Appl Mech Eng 2008;**197**:1965–1982. <https://doi.org/10.1016/j.cma.2007.12.015>.
- [27] Guo J, Zhao S, Murakami RI, Zang S. Experimental and numerical investigation for ductile fracture of Al-alloy 5052 using modified Rousselier model. Comput Mater Sci 2013;**71**:115–123. <https://doi.org/10.1016/j.commatsci.2013.01.011>.
- [28] Zhao SD, Xu F, Guo JH, Han XL. Experimental and numerical research for the failure behavior of the clinched joint using modified Rousselier model. J Mater Process Technol 2014;**214**:2134–2145. <https://doi.org/10.1016/j.jmatprotec.2014.03.013>.
- [29] Samal MK, Seidenfuss M, Roos E. A new mesh-independent Rousselier's damage model: Finite element implementation and experimental verification. Int J Mech

- Sci 2009;**51**:619–630. <https://doi.org/10.1016/j.ijmecsci.2009.06.006>.
- [30] Samal MK, Seidenfuss M, Roos E. A comparative assessment of local and nonlocal damage models for prediction of fracture behavior during mixed-mode loading. *Procedia Eng* 2013;**55**:493–498. <https://doi.org/10.1016/j.proeng.2013.03.286>.
- [31] Xu Y, Poh LH. Localizing gradient-enhanced Rousselier model for ductile fracture. *Int J Numer Methods Eng* 2019;**119**:826–851. <https://doi.org/10.1002/nme.6074>.
- [32] Arun S. An enhanced void-crack-based Rousselier damage model for ductile fracture with the XFEM 2018;0:1–27. <https://doi.org/10.1177/1056789518802624>.
- [33] Areias P, Dias-Da-Costa D, Sargado JM, Rabczuk T. Element-wise algorithm for modeling ductile fracture with the Rousselier yield function. *Comput Mech* 2013;**52**:1429–1443. <https://doi.org/10.1007/s00466-013-0885-0>.
- [34] Zanganeh M, Pinna C, Yates JR. Void growth and coalescence modelling in AA2050 using the Rousselier model. *Int J Damage Mech* 2013;**22**:219–237. <https://doi.org/10.1177/1056789512441808>.
- [35] Thomason PF. A View on Ductile-Fracture Modelling, *Fatigue & Fracture of Engineering Materials & Structures*, 1998; **21**:1105–1122.
- [36] de Borst R, Verhoosel C V. Gradient damage vs phase-field approaches for fracture: Similarities and differences. *Comput Methods Appl Mech Eng* 2016;**312**:78–94. <https://doi.org/10.1016/j.cma.2016.05.015>.
- [37] Mandal TK, Phu V, Heidarpour A. Phase field and gradient enhanced damage models for quasi-brittle failure : a numerical comparative study. *Eng Fract Mech* 2019;**207**:48–67. <https://doi.org/10.1016/J.ENGFRACMECH.2018.12.013>.
- [38] Huang C, Gao X. Development of a phase field method for modeling brittle and ductile fracture. *Comput Mater Sci* 2019;**169**:109089. <https://doi.org/10.1016/j.commatsci.2019.109089>.
- [39] Seupel A, Hütter G, Kuna M. An efficient FE-implementation of implicit gradient-enhanced damage models to simulate ductile failure. *Eng Fract Mech*

- 2018;**199**:41–60. <https://doi.org/10.1016/j.engfracmech.2018.01.022>.
- [40] Mediavilla J, Peerlings RHJ, Geers MGD. Discrete crack modelling of ductile fracture driven by non-local softening plasticity. *Int J Numer Methods Eng* 2006;**66**:661–88. <https://doi.org/10.1002/nme.1572>.
 - [41] Hinton E (Ernest), Owen DRJ. *Finite element programming*. Academic Press; 1977.
 - [42] Belytschko T. The Finite Element Method: Linear Static and Dynamic Finite Element Analysis: Thomas J. R. Hughes. *Comput Civ Infrastruct Eng* 2008;**4**:245–246. <https://doi.org/10.1111/j.1467-8667.1989.tb00025.x>.
 - [43] Besson J. Continuum Models of Ductile Fracture: A Review. *Int J Damage Mech* 2010;**19**:3-52 <https://doi.org/10.1177/1056789509103482>.
 - [44] McClintock FA. A Criterion for Ductile Fracture by the Growth of Holes. *J Appl Mech* 1968;**35**(2):363-371. <https://doi.org/10.1115/1.3601204>.
 - [45] Rice JR, Tracey DM. On the ductile enlargement of voids in triaxial stress fields*. *J Mech Phys Solids* 1969;**17**:201–217. [https://doi.org/10.1016/0022-5096\(69\)90033-7](https://doi.org/10.1016/0022-5096(69)90033-7).
 - [46] Lemaitre J. A Continuous Damage Mechanics Model for Ductile Fracture. *J Eng Mater Technol* 1985;**107**(1):83-89. <https://doi.org/10.1115/1.3225775>.
 - [47] Chaboche JL. Continuum Damage Mechanics: Part 1—General Concepts. *J Appl Mech* 1988;**55**(1):59-64. <https://doi.org/10.1115/1.3173661>.
 - [48] Chaboche JL. Continuum Damage Mechanics: Part II -- Damage Growth, Crack Initiation, and Crack Growth. *J Mech* 1988;**55**(1):65-72. <https://doi.org/10.1115/1.3173662>.
 - [49] Tvergaard V, Needleman A. Analysis of the cup-cone fracture in a round tensile bar. *Acta Metall* 1984;**32**:157–169. [https://doi.org/10.1016/0001-6160\(84\)90213-X](https://doi.org/10.1016/0001-6160(84)90213-X).
 - [50] Kachanov L. Time of the Rupture Process under Creep Condition. *Izv Akad Nauk SSSR, Otd Tekhn Nauk* 1958;**8**:26–31.
 - [51] Souza Neto E de, Peric D, Owen DRJ. *Computational Methods for Plasticity*. John

- Wiley & Sons, vol. 55. 2008. <https://doi.org/10.1002/9780470694626>.
- [52] Bai Y, Wierzbicki T. A new model of metal plasticity and fracture with pressure and Lode dependence. *Int J Plast* 2008;**24**:1071–1096. <https://doi.org/10.1016/j.ijplas.2007.09.004>.
 - [53] Agarwal H, Gokhale AM, Graham S, Horstemeyer MF. Void growth in 6061-aluminum alloy under triaxial stress state. *Mater Sci Eng A* 2003;**341**:35–42. [https://doi.org/10.1016/S0921-5093\(02\)00073-4](https://doi.org/10.1016/S0921-5093(02)00073-4).
 - [54] Lemaitre J. A Continuous Damage Mechanics Model for Ductile Fracture. *J Eng Mater Technol* 1985; **107**(1):83-89. <https://doi.org/10.1115/1.3225775>.
 - [55] Benallal A, Billardon R, Doghri I, Mtkanique L De, Cachan ENS De, Paris L. an Integration Algorithm and the for Fully Coupled Elastoplastic and Damage. *Com Appl Num Meth* 1988;**4**:731–740.
 - [56] Koplik J, Needleman A. Void Growth and Coalescence in Porous. *Int J Solids Struct* 1988;**24**:835–853.
 - [57] Gurson AL. Continuum Theory of Ductile Rupture by Void Nucleation and Growth: Part I—Yield Criteria and Flow Rules for Porous Ductile Media. *J Eng Mater Technol* 1977;99:2. <https://doi.org/10.1115/1.3443401>.
 - [58] Mueller R, Maugin GA. On material forces and finite element discretizations. *Comput Mech* 2002;**29**:52–60. <https://doi.org/10.1007/s00466-002-0322-2>.
 - [59] Miehe C, Gürses E, Birkle M. A computational framework of configurational-force-driven brittle fracture based on incremental energy minimization. *Int J Fract* 2007;**145**:245–259. <https://doi.org/10.1007/s10704-007-9078-1>.
 - [60] Pijaudier-Cabot G, Bažant ZP. Nonlocal Damage Theory. [Http://DxDoiOrg/101061/\(ASCE\)0733-9399\(1987\)113:10\(1512\)](http://DxDoiOrg/101061/(ASCE)0733-9399(1987)113:10(1512)1987) 1987.
 - [61] Bažant ZP, Jirásek M. Nonlocal Integral Formulations of Plasticity and Damage: Survey of Progress. *J Eng Mech* 2002;**128**:1119–1149. [https://doi.org/10.1061/\(ASCE\)0733-9399\(2002\)128:11\(1119\)](https://doi.org/10.1061/(ASCE)0733-9399(2002)128:11(1119)).
 - [62] Peerlings RHJ, Borst R De, Brekelmans WAM, Vree JHP de. Gradient enhanced damage for quasi-brittle materials. *Int J Numer Methods Eng* 1996;**39**:3391–3403.

[https://doi.org/10.1002/\(SICI\)1097-0207\(19961015\)39:19<3391::AID-NME7>3.0.CO;2-D](https://doi.org/10.1002/(SICI)1097-0207(19961015)39:19<3391::AID-NME7>3.0.CO;2-D).

- [63] Andrade FXC, Andrade Pires FM, Cesar De Sa JMA. Consistent tangent operators for implicit non-local models of integral type. *Comput Struct* 2014;**141**:59–73. <https://doi.org/10.1016/j.compstruc.2014.05.007>.
- [64] Peerlings R, Geers M, de Borst R, Brekelmans W. A critical comparison of nonlocal and gradient enhanced softening continua. *Int J Solids Struct* 2001;**38**:7723–7746.
- [65] Areias PMA, César de Sá JMA, António CAC. A gradient model for finite strain elastoplasticity coupled with damage. *Finite Elem Anal Des* 2003;**39**:1191–1235. [https://doi.org/10.1016/S0168-874X\(02\)00164-6](https://doi.org/10.1016/S0168-874X(02)00164-6).
- [66] Seidenfuss M, Samal MK, Roos E. On critical assessment of the use of local and nonlocal damage models for prediction of ductile crack growth and crack path in various loading and boundary conditions. *Int J Solids Struct* 2011;**48**:3365–3381. <https://doi.org/10.1016/j.ijsolstr.2011.08.006>.
- [67] Francfort GA, Marigo J-J. Revisiting brittle fracture as an energy minimization problem. *J Mech Phys Solids* 1998;**46**:1319–1342. [https://doi.org/10.1016/S0022-5096\(98\)00034-9](https://doi.org/10.1016/S0022-5096(98)00034-9).
- [68] Miehe C, Welschinger F, Hofacker M. Thermodynamically consistent phase-field models of fracture: Variational principles and multi-field FE implementations. *Int J Numer Methods Eng* 2010;**83**:1273–1311. <https://doi.org/10.1002/nme.2861>.
- [69] Miehe C, Hofacker M, Welschinger F. A phase field model for rate-independent crack propagation: Robust algorithmic implementation based on operator splits. *Comput Methods Appl Mech Eng* 2010;**199**:2765–2778. <https://doi.org/10.1016/j.cma.2010.04.011>.
- [70] Fang J, Wu C, Rabczuk T, Wu C, Ma C, Sun G, et al. Phase field fracture in elastoplastic solids: Abaqus implementation and case studies. *Theor Appl Fract Mech* 2019;103. <https://doi.org/10.1016/j.tafmec.2019.102252>.
- [71] Alessi R, Marigo J-J, Maurini C, Vidoli S. Coupling damage and plasticity for a phase-field regularisation of brittle, cohesive and ductile fracture: one-

- dimensional examples. *Int J Mech Sci* 2017;Submitted:1–18.
<https://doi.org/10.1016/j.ijmecsci.2017.05.047>.
- [72] Borden MJ, Hughes TJR, Landis CM, Anvari A, Lee IJ. A phase-field formulation for fracture in ductile materials: Finite deformation balance law derivation, plastic degradation, and stress triaxiality effects. *Comput. Methods Appl. Mech. Engrg.* 2016;**312**:130–166. <https://doi.org/10.1016/j.cma.2017.06.023>.
 - [73] Ambati M, Gerasimov T, De Lorenzis L. Phase-field modeling of ductile fracture. *Comput Mech* 2015;**55**:1017–1040. <https://doi.org/10.1007/s00466-015-1151-4>.
 - [74] Aravas N. On the numerical integration of a class of pressure-dependent plasticity models. *Int J Numer Methods Eng* 1987;**24**:1395–1416. <https://doi.org/10.1002/nme.1620240713>.
 - [75] Zhang ZL. Explicit consistent tangent moduli with a return mapping algorithm for pressure-dependent elastoplasticity models. *Comput Methods Appl Mech Eng* 1995;**121**:29–44. [https://doi.org/10.1016/0045-7825\(94\)00707-T](https://doi.org/10.1016/0045-7825(94)00707-T).
 - [76] Sumi Y, Wang ZN. A finite-element simulation method for a system of growing cracks in a heterogeneous material. *Mech Mater* 1998;**28**:197–206. [https://doi.org/10.1016/S0167-6636\(97\)00048-3](https://doi.org/10.1016/S0167-6636(97)00048-3).
 - [77] Moës N, Stolz C, Bernard PE, Chevaugeon N. A level set based model for damage growth: The thick level set approach. *Int J Numer Methods Eng* 2011;**86**:358–380. <https://doi.org/10.1002/nme.3069>.
 - [78] Li H, Fu MW, Lu J, Yang H. Ductile fracture: Experiments and computations. *Int J Plast* 2011;**27**:147–180. <https://doi.org/10.1016/j.ijplas.2010.04.001>.
 - [79] Rousselier G, Quilici S. Combining porous plasticity with Coulomb and Portevin-Le Chatelier models for ductile fracture analyses. *Int J Plast* 2015;**69**:118–133. <https://doi.org/10.1016/j.ijplas.2015.02.008>.
 - [80] Ambati M, Kruse R, De Lorenzis L. A phase-field model for ductile fracture at finite strains and its experimental verification. *Comput Mech* 2016;**57**:149–167. <https://doi.org/10.1007/s00466-015-1225-3>.
 - [81] Guo J, Engineering E. An experimental and numerical investigation on damage evolution and ductile fracture mechanism of aluminum alloy 2016. PhD Thesis.

<https://doi.org/10.13140/RG.2.1.4544.7283>.

- [82] Andrade F, de Sá JC, Pires FA. Assessment and comparison of non-local integral models for ductile damage. *Int J Damage Mech* 2014;**23**:261–296. <https://doi.org/10.1177/1056789513493103>.
- [83] Malcher L, Andrade Pires FM, César De Sá JMA. An assessment of isotropic constitutive models for ductile fracture under high and low stress triaxiality. *Int J Plast* 2012;**30–31**:81–115.
- [84] Antony K, Arivazhagan N, Senthilkumaran K. Numerical and experimental investigations on laser melting of stainless steel 316L metal powders. *J Manuf Process* 2014;**16**:345–355. <https://doi.org/10.1016/j.jmapro.2014.04.001>.
- [85] Yasa E, Kruth JP. Microstructural investigation of selective laser melting 316L stainless steel parts exposed to laser re-melting. *Procedia Eng* 2011;**19**:389–395. <https://doi.org/10.1016/j.proeng.2011.11.130>.
- [86] Salman OO, Gammer C, Eckert J, Salih MZ, Abdulsalam EH, Prashanth KG, et al. Selective laser melting of 316L stainless steel: Influence of TiB₂ addition on microstructure and mechanical properties. *Mater Today Commun* 2019;**21**. <https://doi.org/10.1016/j.mtcomm.2019.100615>.
- [87] Andreatta F, Lanzutti A, Vaglio E, Totis G, Sortino M, Fedrizzi L. Corrosion behaviour of 316L stainless steel manufactured by selective laser melting. *Mater Corros* 2019;**70**:1633–1645. <https://doi.org/10.1002/maco.201910792>.
- [88] Wolff S, Lee T, Faierson E, Ehmann K, Cao J. Anisotropic properties of directed energy deposition (DED)-processed Ti–6Al–4V. *J Manuf Process* 2016;**24**:397–405. <https://doi.org/10.1016/j.jmapro.2016.06.020>.
- [89] Guo P, Zou B, Huang C, Gao H. *Journal of Materials Processing Technology* Study on microstructure , mechanical properties and machinability of efficiently additive manufactured AISI 316L stainless steel by high-power direct laser deposition. *J Mater Process Tech* 2017;**240**:12–22. <https://doi.org/10.1016/j.jmatprotec.2016.09.005>.
- [90] Gibson I, Rosen DW, Stucker B. *Additive Manufacturing Technologies*. Boston, MA: Springer US; 2010. <https://doi.org/10.1007/978-1-4419-1120-9>.

- [91] Muller P, Mognol P, Hascoet J. Journal of Materials Processing Technology Modeling and control of a direct laser powder deposition process for Functionally Graded Materials (FGM) parts manufacturing. J Mater Process Tech 2013;**213**:685–692. <https://doi.org/10.1016/j.jmatprotec.2012.11.020>.
- [92] Sames WJ, List FA, Pannala S, Dehoff RR, Babu SS, List FA, et al. The metallurgy and processing science of metal additive manufacturing The metallurgy and processing science of metal additive manufacturing 2016;6608. <https://doi.org/10.1080/09506608.2015.1116649>.
- [93] Susan DF, Puskar JD, Brooks JA, Robino C V. Quantitative characterization of porosity in stainless steel LENS powders and deposits. Mater Charact 2006;**57**:36–43. <https://doi.org/10.1016/j.matchar.2005.12.005>.
- [94] Wang L, Pratt P, Felicelli SD, El Kadiri H, Berry JT, Wang PT, et al. Pore formation in laser-assisted powder deposition process. J Manuf Sci Eng Trans ASME 2009;**131**:0510081–9. <https://doi.org/10.1115/1.3184087>.
- [95] Wolff SJ, Lin S, Faierson EJ, Liu WK, Wagner GJ, Cao J. A framework to link localized cooling and properties of directed energy deposition (DED)-processed Ti-6Al-4V. Acta Mater 2017;**132**:106–117. <https://doi.org/10.1016/j.actamat.2017.04.027>.
- [96] Dass A, Moridi A. State of the art in directed energy deposition: From additive manufacturing to materials design. Coatings 2019;**9**:1–26. <https://doi.org/10.3390/COATINGS9070418>.
- [97] Rousselier G, Quilici S. Combining porous plasticity with Coulomb and Portevin-Le Chatelier models for ductile fracture analyses. Int J Plast 2015;**69**:118–133. <https://doi.org/10.1016/j.ijplas.2015.02.008>.
- [98] Gao X, Wang T, Kim J. On ductile fracture initiation toughness: Effects of void volume fraction, void shape and void distribution. Int J Solids Struct 2005;**42**:5097–5117. <https://doi.org/10.1016/j.ijsolstr.2005.02.028>.
- [99] Ji S, Gu Q, Xia B. Porosity dependence of mechanical properties of solid materials. J Mater Sci 2006;**41**:1757–1768. <https://doi.org/10.1007/s10853-006-2871-9>.
- [100] Yu C, Ji S, Li Q. Effects of porosity on seismic velocities, elastic moduli and

- Poisson's ratios of solid materials and rocks. *J Rock Mech Geotech Eng* 2016;**8**:35–49. <https://doi.org/10.1016/j.jrmge.2015.07.004>.
- [101] Mukherjee T, Zuback JS, De A, DebRoy T. Printability of alloys for additive manufacturing. *Sci Rep* 2016;6. <https://doi.org/10.1038/srep19717>.
- [102] Pham K, Amor H, Marigo JJ, Maurini C. Gradient damage models and their use to approximate brittle fracture. *Int J Damage Mech* 2011;**20**:618–652. <https://doi.org/10.1177/1056789510386852>.
- [103] Mandal TK, Nguyen VP, Wu JY. Length scale and mesh bias sensitivity of phase-field models for brittle and cohesive fracture. *Eng Fract Mech* 2019;217:106532. <https://doi.org/10.1016/j.engfracmech.2019.106532>.

Related Publications

- E. Azinpour, J. P. S. Ferreira, M. P. L. Parente and J. Cesar de Sa, A simple and unified implementation of phase field and gradient damage models, Adv. Model. and Simul. In Eng. Sci.(2018)5:15, <https://doi.org/10.1186/s40323-018-0106-7>
- E. Azinpour, J. Cesar de Sa and A. Santos, Phase field approach for ductile failure using Rousselier model, Proceedings of NUMIFORM 2019: The 13th International Conference on Numerical Methods in Industrial Forming Processes
- E. Azinpour, J. Cesar de Sa and A. Santos, Micromechanically-motivated phase field approach to ductile fracture (under review)
- E. Azinpour, R. Darabi, J. Cesar de Sa, A. Santos, J. Hodek and J. Dzukan, Fracture analysis in directed energy deposition (DED) manufactured 316L stainless steel using a phase-field approach (Accepted for publication)
- E. Azinpour, J. M. A. César de Sá, A. Santos, A phase-field approach for ductile failure, MS1, ID142, The 12th international conference NUMIFORM 2016, Troyes, France, (<http://numiform2016.utt.fr/Papers/program.htm>)